TAILORING THE DEFECTS IN ZnO AND ZnO-GRAPHENE HYBRIDS FOR VISIBLE LIGHT PHOTOCONDUCTIVITY AND NONLINEAR ABSORPTION

A Thesis submitted

in partial fulfillment for the Degree of

Doctor of Philosophy

by

KAVITHA M. K.

Department of Chemistry

INDIAN INSTITUTE OF SPACE SCIENCE AND TECHNOLOGY

THIRUVANANTHAPURAM

NOVEMBER, 2014

CERTIFICATE

This is to certify that the thesis entitled **Tailoring the defects in ZnO and ZnO-graphene hybrids for visible light photoconductivity and nonlinear absorption** submitted by **Kavitha M. K.** to the Indian Institute of Space Science and Technology, Thiruvananthapuram, in partial fulfillment for the award of the degree of **Doctor of Philosophy** is a *bonafide* record of research work carried out by her under our supervision. The contents of this thesis, in full or in parts, have not been submitted to any other Institution or University for the award of any degree or diploma.

Dr. Honey John
Supervisor
Department of Chemistry

Dr. Pramod Gopinath
Co-supervisor
Department of Physics

Thiruvananthapuram
November, 2014

Counter signature of HOD with seal

DECLARATION

I declare that this thesis entitled **Tailoring the defects in ZnO and ZnO-graphene hybrids for visible light photoconductivity and nonlinear absorption** submitted in partial fulfillment of the degree of **Doctor of Philosophy** is a record of original work carried out by me under the supervision of Dr. Honey John and Dr. Pramod Gopinath, and has not formed the basis for the award of any other degree or diploma, in this or any other Institution or University. In keeping with the ethical practice in reporting scientific information, due acknowledgements have been made wherever the findings of others have been cited.

Kavitha M. K.
SC10D016

Thiruvananthapuram – 695547
27/11/2014

ACKNOWLEDGEMENTS

This thesis is the summary of the past four years of my life, which is a journey consisting of patience and joy, profound knowledge and exciting achievements. The good fortune of working in my field of interest, the deep-rooted passion I acquired throughout these years gives me sense of satisfaction and happiness, for which I am fully indebted to Dr. Honey John, my thesis supervisor, who inspires me in every way. Her scientific intuitions and firm belief in students influenced and helped me a lot to grow us an independent researcher at the end of this journey. She is always there when I need support in all matters relating to professional and personal life. I express my heartfelt gratitude for her guidance and encouragement, directed me to the successful completion of this thesis. I am grateful to Dr. Pramod Gopinath, my co-supervisor for his support and valuable advices to be a competent researcher. His immense patience in reviewing our papers and this thesis is appreciable.

I thank Dr. K.S. Dasgupta, Director IIST for providing me opportunity to work in the excellent ambience of IIST. My special thanks to Dr. Adimurthy, former Dean R & D, for his inspirational words when I first stepped to IIST as a student. I express my sincere gratitude to Prof. Kuruvilla Joseph, HOD, Chemistry for his readiness in finding solution for all our problems in the lab. I am very much indebted to my doctoral committee members for their valuable suggestions given to my work. I express my special thanks to Dr. K. N. Ninan for his critical evaluation of my research work in every doctoral committee meetings, which helped me to improve a lot. I render my thanks to faculty members of Department of Chemistry and my fellow research students for their support. I express my thanks to all staff members of Chemistry department, especially K. G. Dileepkumar for setting the lab.

I convey my special gratitude to Dr. K. B. Jinesh for the valuable and thoughtful discussions that given me courage to understand in depth of solid state

chemistry. I am thankful to Dr. Reji Philip, Raman Research Institute, Bangalore for providing the Z-scan facility. I remember with gratitude the warm hospitality rendered to me during my various visit to his lab. I am extremely thankful to SAIF, IIT Chennai for providing their facility for SEM analysis, Prof Vidyasagar, Department of Chemistry, IIT Chennai for XRD measurements, NIIST for TEM and AIMS for Raman and XPS measurements.

I remember with pleasure the time I spent with my fellow researchers Remyamol, Haripadmam, Jalaja, Sarah, Sarika, Dhanya, Raneesh, Bharath and Narasimman, they made my life at IIST pleasant and memorable. Special thanks to Remyamol and Haripadmam for the fruitful discussions, healthy arguments and for being my best batchmates. At this time, I remember all my teachers with gratitude, their blessings made me what I am. I thank all my friends who have been a part of my life. Special thanks to Unnikrishnan who has been a pillar of support in all my joys and hardships.

The happiest person in this world for all my achievements is my little sister Mahitha, thanks to her great companionship. In no words I can express my gratitude for the love and care of my parents. I wish to thank them for the loving and patient support for all the endeavours in my life. Without their prayers, this thesis would have never become a reality. Finally, I acknowledge the supreme power for all the blessings.

Kavitha M. K.

ABSTRACT

Nano ZnO is projected as future material for optoelectronic application. However, a deep understanding of surface defect is necessary to construct high performance devices. These defects are critical in controlling its optical and electrical properties. The combination of ZnO and graphene provides hybrid materials with excellent optoelectronic properties.

This thesis mainly focuses on the synthesis of ZnO nanocones and its hybrid with graphene, discusses the nature of defects in ZnO and correlates it with optoelectronic properties like visible photoconductivity and nonlinear absorption. Tailoring the morphology and crystal facets of ZnO nanocrystals will facilitate the modification of intrinsic defects, which in turn vary the optoelectronic properties of ZnO. ZnO nanocones are synthesized by solution precipitation and hydrothermal method using polyvinyl pyrrolidone as capping agent. In this method, polyvinyl pyrrolidone enhances the crystallisation of ZnO by its excellent adsorption ability. The growth of ZnO nanocones is mainly controlled by the concentration of hydroxyl ions in the reaction medium (This part of the work is published in Materials Research Bulletin 2014). The cone shaped morphology has polar oxygen terminated facets exposed, which can facilitate oxygen vacancy centres on the surface of ZnO.

The defects in ZnO can modify the optical and electrical properties of ZnO. The photoluminescence of ZnO nanocones and its calcined samples indicate that the as-grown samples have both oxygen and zinc vacancies. After calcination, oxygen vacancies vanish and zinc vacancies enhance. Photoconductivity of the samples reduces significantly upon calcination, due to the reduction in oxygen vacancies. However, the samples exhibit a significant enhancement in the *effective* two-photon absorption upon calcination, indicating that nonlinear optical absorption originates from zinc vacancies. (This part is published in Physical Chemistry Chemical Physics 2014).

Functionalisation of ZnO with graphene can alter the ZnO defect states, by its interfacial interaction. A solution method for the in-situ growth of ZnO on reduced graphene oxide is presented. During this growth, the oxygen vacancy states are healed out by the diffusion of oxygen from graphene oxide to ZnO and the zinc vacancies are retained. The visible photoconductivity of the hybrid is depleted, compared to pure ZnO. These ZnO decorated reduced graphene oxide sheets exhibit good optical limiting property than its individual counterparts, suggesting the Zn vacancy states assisted *effective* two-photon absorption with photoinduced electron transfer between ZnO and graphene sheets. These results suggest its scope as good optical limiting material. (Published in Journal of Materials Chemistry C 2013).

Finally a layer-by-layer self assembly method is proposed for the fabrication of multilayer films with ZnO nanocones and reduced graphene oxide. These films exhibit improved photoconductivity due to efficient charge transfer from ZnO and its shuttling through graphene. Its shows saturable absorption and optical limiting with respect to input intensity.

In conclusion, this thesis presents an understanding of the defects in ZnO nanocones and reduced graphene oxide/ZnO hybrids and its relationship with properties like photoconductivity and nonlinear absorption.

TABLE OF CONTENTS

LIST OF FIGURES

LIST OF TABLES

ABBREVIATIONS

^{o}C	Degree Celsius
µA	Microampere
µJ	Microjoule
µl	Microlitre
µm	Micrometre
2D	Two Dimensional
BE	Binding energy
cm	centimetre
CNTs	Carbon Nanotubes
CTAB	Cetyl trimethylammonium bromide
CVD	Chemical Vapour Deposition
DFT	Density Functional theory
DOS	Density of States
ESA	Excited state absorption
ESCA	Electron Spectroscopy for Chemical Analysis
eV	electron volt
FCA	Free Carrier Absorption
Fig.	Figure
FTIR	Fourier Transform Infrared
FTO	Fluorine doped Tin Oxide
g	gram
GO	Graphite Oxide
GW	giga watt
h	Hour
HRTEM	High Resolution Transmission Electron Microscope
Hz	hertz
I_D	Intensity of D band in Raman spectrum
I_{dark}	Dark current
I_G	Intensity of G band in Raman spectrum

I_{light}	Current generated after light illumination
I_{GE}	Intensity of green emission
I_{UV}	Intensity of UV emission
IR	Infrared
K	Kelvin
KE	Kinetic energy
kV	kilo volt
LBL	Layer-by-layer
M	Molar
m	metre
meV	millielectronvolt
mg	milligram
min	Minute
ml	millilitre
mm	millimetre
mW	milliwatt
Nd:YAG	Neodymium-doped Yitrium Aluminum Garnet
NIR	Near Infrared
NR	nonradiative
NLO	Nonlinear Optical
NLS	Nonlinear scattering
nm	Nanometre
ns	Nanosecond
pH	Potential of Hydrogen
PL	photoluminescence
PMT	Photomultiplier Tube
PAM	polyacrylamide
PSS	Poly (sodium 4-styrene sulfonate)
PVP	Poly vinyl pyrrolidone
rpm	Revolutions Per Minute
RSA	Reverse Saturable Absorption
s	second

SA	Saturable absorption
SAED	Selected Area Diffraction Pattern
SEM	Scanning Electron Microscopy
TCSPC	Time correlated single photon counting
TEM	Transmission Electron Microscope
TGA	Thermogravimetric Analysis
TPA	Two-photon absorption
UV	Ultraviolet
v/v	Volume/volume
vis	visible
W	watt
wt %	Weight percentage
XPS	X-ray Photoelectron Spectroscopy
XRD	X-ray Diffraction

NOTATIONS

$\overline{P}(r,t)$	Polarization
$\overline{E}(r,t)$	Electric field
$\chi_{ij}^{(1)}$	First order susceptibility
$\chi_{ijk}^{(2)}$	Second order susceptibility
$\chi_{ijkl}^{(3)}$	Third order susceptibility
λ	Wavelength
d	Crystal lattice spacing
θ	Angle of diffraction
D	Crystallite size
B	Diffraction peak broadening
c	Velocity of light
φ	XPS correction factor
α	Molar extinction coefficient
C	Fitting parameter in Tauc equation
h	Planck's constant
E_g	Bandgap
L	Thickness of the sample of Z scan experiment
ω_0	Beam waist
Z_0	Diffraction length of the focussed laser beam
I	Current
α	Linear absorption coefficient
β	Two photon absorption coefficient
z	Position
υ	Frequency
R	Fresnel reflection
I_0	Peak on-axis intensity
A_1	Pre-exponential factor
A_2	Pre-exponential factor

L	Length of the sample medium
T	Transmittance
V	Voltage
E(z)	Input fluence at each z position
β_{eff}	Effective nonlinear absorption coefficient
I_{sat}	Saturation intensity
ω(z)	Beam radius
τ	lifetime
V_{Zn}	Zinc vacancy
V_O	Oxygen vacancy
Zn_i	Zinc interstitial
O_i	Oxygen interstitial
$Zn_i^{\cdot\cdot}$	Doubly positive zinc interstitial
$Zn_i^{\cdot}$	Singly positive zinc interstitial
$V_O^{\cdot\cdot}$	Doubly positive oxygen vacancy
$V_O^{\cdot}$	Singly positive oxygen vacancy
$V_O^{\times}$	Neutral oxygen vacancy
V_{Zn}''	Doubly negative zinc vacancy
V_{Zn}'	Singly negative zinc vacancy

NOMENCLATURE

ZnO	Zinc oxide
$Zn(Ac)_2$. $2H_2O$	Zinc acetate dihydrate
GaAs	Gallium Arsenide
H_2SO_4	Sulfuric acid
HNO_3	Nitric acid
$KMnO_4$	Potassium permanganate
CH_3COOH	Acetic acid
HCl	Hydrochloric acid
H_2O_2	Hydrogen peroxide
NaOH	Sodium hydroxide
PbS	Lead sulphide
TiO_2	Titanium dioxide
AgCl	Silver chloride
Ag	Silver
Cu	Copper
Pt	Platinum
CdSe	Cadmium selenide
Na_2SO_4	Sodium sulphate
CO_2	Carbon dioxide
HCl	Hydrochloric acid
–COOH	Carboxylic acid group
KBr	Potassium bromide
OH^-	Hydroxyl group

CHAPTER 1
INTRODUCTION

This chapter presents an overview about zinc oxide and its hybrids with graphene. The nature of defects in ZnO plays a critical role in modifying its absorption, photoluminescence and conductivity. The section of ZnO describes on crystal structure, various methods for the synthesis of ZnO nanostructure, and mechanism of photoconductivity and nonlinear absorption. The general features of graphene and the significance of ZnO/graphene hybrids are also discussed along with scope and objectives of the thesis.

1.1. Background

ZnO research has long history, but by last decade, it recovered its recognition as a versatile material for optoelectronic applications. This is because of the progress in the development of crystalline ZnO with unique optical and electrical properties. Controlling the conductivity is an important challenge in ZnO research, because a small variation in the concentration and type of native defects can significantly affect the electrical and optical properties (Look, et al., 1999a; Schmidt-Mende and MacManus-Driscoll, 2007; Xu, et al., 2013). Therefore, deep understanding of intrinsic point defects and addition of impurities are the key factors to control the conductivity. By modifying the synthesis conditions and post-growth treatments like calcination and hydrothermal treatment, researchers are trying to control the defect states and associated charge carriers (Akhavan, et al., 2009; Georgekutty, et al., 2008)

Combining ZnO with other functional materials like carbon nanotubes, graphene, noble metal nanoparticles, semiconductor quantum dots, etc., are the recent approach to improve the optical and electrical performance of ZnO (Gu, et al., 2013; Lee, et al., 2009; Nguyen, et al., 2014; Son, et al., 2012; Tak, et al., 2009; Tian, et al., 2012; Wang, C. Y. and Adhikari, 2011; Williams and Kamat, 2009; Zhu, et al., 2006). These hybrid materials offer improved performance than

individual components due to the synergetic effect caused by their interfacial interaction. Taking into account photo-induced charge separation ability of ZnO and excellent conductivity of graphene, ZnO/graphene hybrids are one of the remarkable candidates for optoelectronic applications.

1.2. Zinc oxide

ZnO is considered as an alternative for GaAs in optoelectronic devices, due to its wide direct bandgap (3.37 eV at 300 K) comparable to GaAs, large exciton binding energy (60 meV) at room temperature, excellent electron mobility (Li, F. M., et al., 2008) and good thermal conductivity (Özgür, et al., 2006). It has many superior properties over GaAs like greater resistance to high energy radiation (Look, et al., 1999b), higher quantum efficiency (van Dijken, et al., 2001), etc. The most significant benefit is the low cost and ease of preparation with good crystal quality.

ZnO belongs to the group of II-IV compound semiconductors, crystallized in cubic zinc blende, cubic rocksalt or hexagonal wurtzite structure, where each Zn^{2+} ions are tetrahedrally surrounded by four O^{2-} ions, and vice versa. The tetrahedral coordination means sp^3 hybridised covalent bonding, but these material have partial ionic character due to the polarity difference. Under ambient conditions, the thermodynamically stable phase is that of wurtzite symmetry. The wurtzite structure of ZnO can be described as number of alternating planes composed of tetrahedrally coordinated Zn^{2+} and O^{2-} ions stacked alternately along the c-axis as shown in Fig 1.1 a. This tetrahedral coordination results in the lack of inversion symmetry perpendicular to c-axis. The wurtzite crystal surface could take specific configuration depending on the distribution of cations and anions and some important crystal facets are given in Fig 1.1 b. Some surfaces can be terminated entirely by cations or anions, resulting in charged surface called polar surfaces. Some other surfaces have equal distribution of cations and anions resulting in nonplanar surfaces. Zn^{2+} ions produce positively charged surface designated as (0001) plane and O^{2-} ions produce negatively charged surface designated as $(000\bar{1})$ plane (Wang, 2009). Because of the superior stability of

these two polar surface, ± (0001) are the most commonly used surface and direction for growth. Another polar surface is $(10\bar{1}1)$, which are not common in ZnO, but they are observed in nanohelical (Yang, et al., 2004) and nanocone (Chang, et al., 2013) structures. The polar surfaces are highly reactive owing to its high surface energy. The other commonly observed surfaces of ZnO are $(2\bar{1}\bar{1}0)$, $(10\bar{1}0)$, which are non-polar and have lower energy than polar facets. It is commonly observed in one-dimensional nanostructures like rods, wires, etc. (Lv, et al., 2011; Song, et al., 2008). By tuning the growth rate along different crystallographic directions, it is possible to obtain a wide range of ZnO nanostructures.

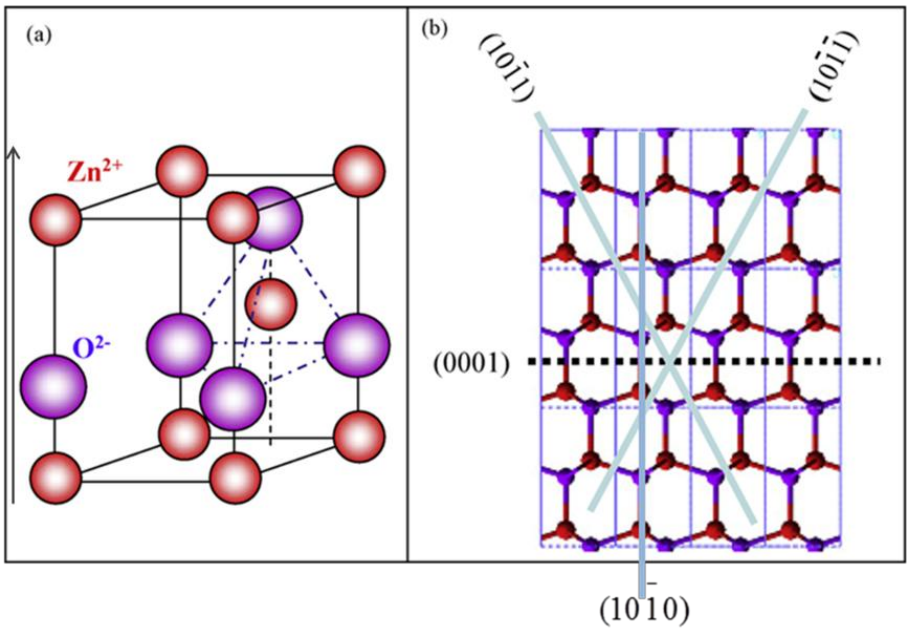

Figure 1.1. (a) The wurtzite structure of ZnO and the representation of tetrahedral cordination (b) Three types of crystal facets of ZnO nanostructures (Wang, Z. L., 2009)

1.2.1. Synthesis of ZnO nanostructures

Synthesis methods can be broadly classified in to solution phase synthesis and gas phase synthesis. In solution phase synthesis, ZnO is grown in liquid phase. Some of the solution phase synthesis involves sol-gel method, controlled precipitation, solvothermal or hydrothermal method, etc. (Kuo, et al.,

2012; Li, et al., 2005; Rai, et al., 2013; Rodríguez-Paéz, et al., 2001; Xu, et al., 2013). Gas phase synthesis involves the growth from a gaseous environment in closed chambers. Some common gas phase methods are physical vapor deposition, chemical vapor deposition, and microwave thermal decomposition (Bilecka, et al., 2009; Cheng, et al., 2008; García-Gutiérrez, et al., 2012; Jimenez-Cadena, et al., 2010; Phan, et al., 2010). Solution phase methods are getting much attention owing to its simplicity, low cost, reliability, repeatability and relatively mild synthesis conditions.

Among the solution methods, sol-gel method has gained popularity as it offers control over the size and shape of nanostructures. In sol-gel method, concentrated alcoholic solution of zinc salt is refluxed to form a transparent sol. ZnO is grown from this sol by either condensation or by the addition of hydroxides (Li, et al., 2005). Controlled precipitation is also widely accepted since it is possible to obtain products with repeatable properties. Controlled precipitation involves the fast and spontaneous growth of ZnO from a zinc salt by the addition of base in aqueous phase (Rodríguez-Paéz, et al., 2001). The process of precipitation is controlled by reaction conditions such as pH, temperature and precipitation time. In this method, capping agents have critical role in controlling the particle size and agglomeration. The capping agents also fasten the crystallization of ZnO from zinc hydroxide by dissolution-reprecipitation and dehydration. Many surfactants like sodium dodecyl sulphate, cetyl trimethylammonium bromide (CTAB), hexamethylene diamine and polymers like polyvinyl alcohol, polyethylene glycol, polyvinyl pyrrolidone, etc. are used as capping agents for the crystallization of ZnO from solution (Ashfold, et al., 2007; Feng, et al., 2010; Jia, et al., 2013; Shao, et al., 2012; Sun, et al., 2003; Zhang, J., et al., 2007; Zhang, L. Z. and Xiang, 2011).

Hydrothermal method involves the crystallization of ZnO from aqueous medium by heating in an autoclave. Among the solution methods, hydrothermal method is attractive for the high degree of crystallinity of the product and environmental friendly conditions (Sunandan, et al., 2009). In this method,

particle size and morphology can be controlled by varying the conditions like temperature, pressure and pH of the solution. Polsongkram et al. (2008) demonstrated the relationship between the reaction temperature and aspect ratio of ZnO nanorods preapared by hydrothermal method. Zhang, Z. and Mu. (2007) synthesized nanobundles of ZnO with pyramid like and hexagonal prism shapes using polyethers in hydrothermal condition. The growth of prism and pyramid like ZnO nanocrystals are attributed to the different growth rate of various crystal facets. In hydrothermal condition the growth rate of different planes are (0001) > $(10\bar{1}1)$ > $(10\bar{1}0)$ (Laudise, et al., 1960). The more rapid the growth rate, the quicker the disappearance of the plane. The (0001) plane disappears quickly due to the fast growth rate, resulting in tip shape at the end of the c-axis. If the growth rate of $(10\bar{1}0)$ is slow, they form hexagonal prisms while slow growth of $(10\bar{1}1)$ plane result in pyramid like pointed structures (Wang and Song, 2005).

1.2.2. Native point defects and optical properties

In ZnO, depending on the growth rate of different crystal planes, nanostructures with variety of morphologies can be prepared. In these different morphologies, nature of exposed crystal facets (either polar or nonpolar) will be different. The surface related intrinsic or native defects will change with respect to different morphologies. The intrinsic defects in ZnO include vacancies (oxygen or zinc vacancies), interstitials (oxygen or zinc interstitials) and antisites (Zn atom occupying in O atom lattice site or vice versa) (Janotti and van de Walle 2007). These imperfections will create donor or acceptor levels within the band structure and it can strongly influence the electrical and optical properties of ZnO (Erhart, et al., 2006). Oxygen vacancies and zinc interstitials have most often mentioned as the sources of n-type conductivity (Ellmer, et al., 2007; Look, et al., 1999a). However, oxygen vacancies are considered as potential source for the compensation of p-type conductivity (Henini, 2012). The intrinsic carriers can vary the minority carrier lifetime and luminescence efficiency, which in turn modifies the optical properties. Understanding the behavior of intrinsic defects in ZnO is therefore essential to its successful application in semiconductor devices. The formation of defects depends on growth and post-growth treatment conditions

(van de Walle and Neugebauer, 2004). For example, the formation of oxygen vacancy is determined by the relative abundance of Zn and O atoms in the environment. The defects introduce transition levels within the bandgap of the semiconductor (Schmidt-Mende and Macmanus-Driscoll, 2007). Fig 1.2 shows the energy level of native defects in ZnO. There are a number of defects within the bandgap of ZnO. The donor defects are $Zn_i^{\cdot\cdot}$, $Zn_i^{\cdot}$, $Zn_i^{\times}$, $V_O^{\cdot\cdot}$, $V_O^{\cdot}$, $V_O^{\times}$ and the acceptor defects are V_{Zn}'', V_{Zn}'. The Kroger Vink notation used here represents i = interstitial site, Zn = zinc, O = oxygen and V = vacancy. The superscripted terms indicate charges, where a dot indicates positive charge, a prime indicates negative charge, and a cross indicates zero charge, with charges in proportion to the number of symbols.

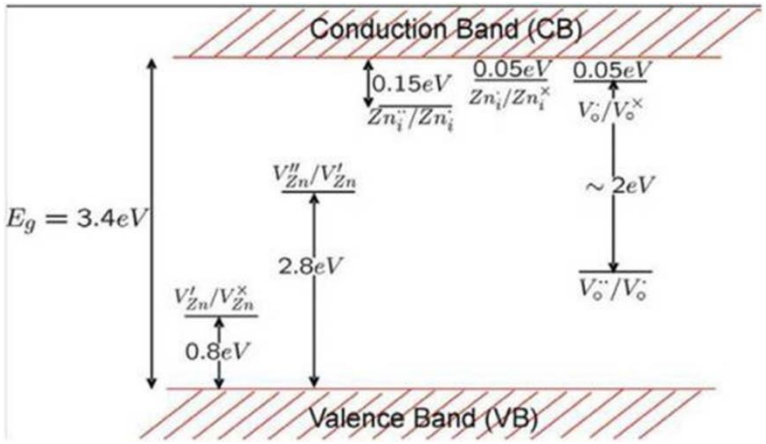

Figure 1.2. Energy levels of native defects in ZnO (Schmidt-Mende and MacManus-Driscoll, 2007)

The defect states can modify the emission of ZnO. When ZnO is excited with photons of energy higher than bandgap leads to band to band excitation and formation of excitons. Excited free carriers are then trapped by V_{Zn} and V_O, occupying in the deep energy levels in the bandgap. De-excitation and radiative recombination provide band edge emission as well as defect related visible emissions. The nature of intrinsic defects contributing visible emission is still a matter of controversy. Several groups have suggested that oxygen vacancies are

responsible for green emission in ZnO (Gong, et al., 2007; Leiter, et al., 2001) and Zn vacancies can cause blue emission (Shim, et al., 2012; Willander, et al., 2010). Leung et al. (2013) showed that Zn vacancies also contribute to green emission. Many researchers are trying to find out the defect states related to visible emission and its relationship with size and shape of ZnO nanostructures. Zhang, X. et al. (2014) synthesized ZnO nanorods with different aspect ratio. The high aspect ratio nanorods exhibit high level of surface oxygen vacancies causing green and yellow emission. Bitenc et al. (2009) proposed a hypothesis that radiative contribution of defects increase with the decrease of nanocrystal size. Kurbanov et al. (2009) demonstrated that violet emission in ZnO nanocrystals is related to zinc vacancy states.

The structural disorders in ZnO can be identified from the characteristic photoluminescence spectra. The optical properties and transport of charge carriers are strongly influenced by these structural defects. Therefore, understanding of the nature of defects which alter the optical and electrical properties is essential for the fabrication of devices.

1.2.3. Photoconductivity

Photoconductivity is defined as electrical conductivity resulting from photo-induced electron excitation. Photoconductivity of the material depends on carrier concentration, carrier life time and carrier dynamics. Upon illumination with photon energy larger than the bandgap, electron-hole pairs are generated and holes are readily trapped at the surface, leaving behind the unpaired electrons, which increases the conductivity under the applied electric field. In ZnO, the photoconduction mechanism is primarily governed by adsorption and desorption of oxygen (Carrey, et al., 2008; Kind, et al., 2002; Soci, et al., 2007). In the dark, oxygen molecules which are adsorbed on ZnO, capture the free electrons present in the n-type semiconductor, and get converted to negatively charged oxygen ions. Under illumination electron-hole pairs are generated; holes migrate to the surface and discharge the oxygen ions. Oxygen will photo-desorb from the surface and the unpaired electrons will enhance the conductivity. Soci et al. (2007)

demonstrated this photoconduction mechanism in a nanowire detector as shown in Fig 1.3.

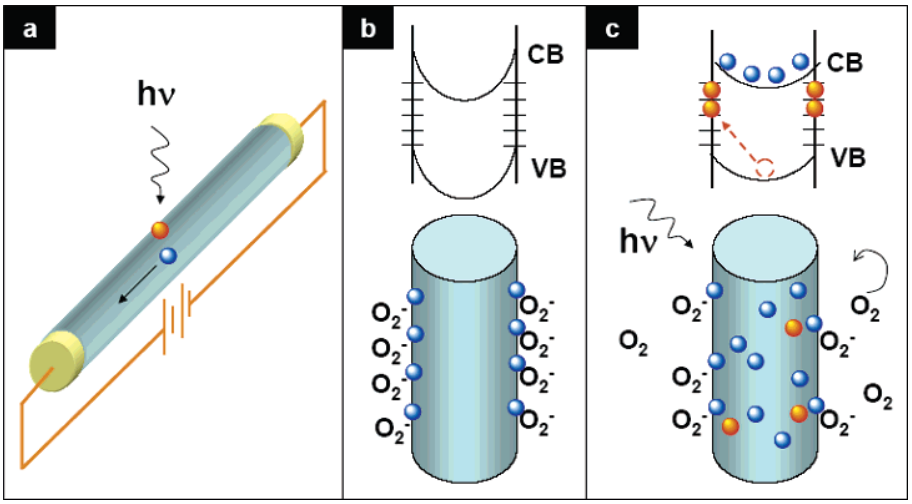

Figure 1.3. (a) Representation of a nanowire photodetector (b) Energy band diagram of the nanowire in dark and oxygen molecules adsorbed at the nanowire surface that capture the free electron present in the n-type semiconductor (c) Under UV illumination, photogenerated holes migrate to the surface and are trapped, leaving behind unpaired electrons that contribute to the photocurrent (Soci, et al., 2007).

ZnO is a well studied UV photoconductor (Chen, et al., 2010; Gimenez, et al., 2010; Kushwaha and Aslam, 2012; Qin, et al., 2011). Sheetz et al. (2009) theoretically demonstrated that the presence of oxygen vacancies in ZnO contribute strongly to optical absorption in visible spectra regime. Using first principle density functional theory (DFT) calculations, they derived the electronic band structure, density of states (DOS) and optical properties of ZnO. In case of O and Zn vacancy, analysis of DOS shows that valence states near the Fermi level is mainly contributed by O 2p states while Zn 3d state contribution is deep down in the valence band. These energy levels deep in the bandgap, created by oxygen and zinc vacancies, allow electronic transitions in the visible region. The simulated optical absorption shows that oxygen vacancies contribute significantly for visible light absorption. These findings open the scope of designing ZnO with improved solar energy absorption by creating oxygen vacancies. There are a few experimental observations regarding the below bandgap photoresponse in ZnO (Liu, Y. et al, 2009; Moazzami, et al., 2006).

1.2.4. Nonlinear optical properties

Under ordinary light, the optical properties of a material are unchanged with respect to the intensity of light falling on it. Nonlinear optics deals with modification of the optical properties in presence of light. Under high intensities, the response of the material depends in a nonlinear manner on the strength of the applied optical field. Light-matter interaction creates electric dipoles leading to macroscopic polarization of the medium. In case of linear optics, the dipole moment per unit volume or polarization $\overline{P}(r,t)$ depends linearly on the strength of the electric field $E(r,t)$ of an applied optical field (Sutherland 2003).

$$\overline{P}(r,t) = \varepsilon_0 \sum_j \chi_{ij}^{(1)} E_j(r,t) \tag{1.1}$$

In nonlinear optics, the optical response can be described by generalizing equation 1.1. by expressing $\overline{P}(r,t)$ as a power series in the field strength $\overline{E}(r,t)$ (Sutherland, 2003).

$$\overline{P}(r,t) = \varepsilon_0 (\sum_j \chi_{ij}^{(1)} E_j(r,t) + \sum_{jk} \chi_{ijk}^{(2)} E_j(r,t) E_k(r,t) + \sum_{jkl} \chi_{ijkl}^{(3)} E_j(r,t) E_k(r,t) E_l(r,t) + ...) \tag{1.2}$$

$\chi_{ij}^{(1)}$, $\chi_{ijk}^{(2)}$ and $\chi_{ijkl}^{(3)}$ are first, second and third order nonlinear susceptibilities, respectively. Only laser radiation is sufficiently intense to modify the optical properties of a material. This is because the nonlinear susceptibilities are by far smaller than the linear susceptibilities. The second order susceptibility is responsible for second order nonlinear optical effects like second harmonic generation, sum and difference frequency generation and optical parametric amplification. Third order nonlinear optical phenomena include two-photon absorption, third harmonic generation, optical Kerr effect, etc.

Nanostructures are of particular interest in nonlinear optics due to the applications arising out of their enhanced response to the applied electromagnetic

field. Depending on the response of the medium to the incident electromagnetic radiation, transmission of light can change by the absorption, scattering and refraction. For example, if the intensity of the input light is such that the corresponding electric field can induce dipole oscillation, it affects the light transmission. The change in transmittance of a medium as a function of input light intensity or fluence is referred as nonlinear transmission or nonlinear absorption. A few major mechanisms that control nonlinear absorption are two/three photon absorption, reverse saturable absorption (RSA), excited state absorption (ESA), saturable absorption (SA) and nonlinear scattering (NLS). By two/three-photon absorption, RSA, ESA and NLS, the nonlinear absorption of the material increases with increase in input fluence. Such materials are called optical limiters. Saturable absorption results in decrease in the absorption of light with input intensity.

In ZnO, nonlinear absorption is the result of different processes like two/three photon absorption, RSA and ESA, therefore ZnO is considered as good optical limiter. Vivas et al. (2010) demonstrated broadband nonlinear absorption in ZnO. RSA is observed in the spectral range of 460-500 nm due to the on photon excitation of deep defect levels in ZnO. The defect levels in ZnO can trap the charge carriers, which change the carrier dynamics, which in turn influence the nonlinear absorption (Anand, et al., 2014; Stehr, et al., 2014). In nanocrystals, size variation changes the energy level spacing and variation in shape, changes the symmetry of wave functions, polarization and localization of the electronic states (Feng and Ji, 2009). These variations in shape (Kavitha, et al., 2013a) and size (Soon Ki Min, 2009) of nanostructures can change nonlinear optical properties. Therefore tailoring the morphology and defects in ZnO is an important strategy to modify its nonlinear optical properties.

Functionalization of ZnO with other active materials like metal nanoparticles (Georgekutty, et al., 2008), CNTs (Park, et al., 2013), graphene, etc. can alter defect states in ZnO by its interfacial interaction and electron transfer mechanism. Among these hybrid materials, ZnO/graphene systems are getting

great attention for optoelectronic devices due to excellent photoresponse of ZnO and near ballistic conductivity of graphene.

1.3. Graphene

Graphene is a monolayer of sp^2 carbon atoms tightly packed into a honeycomb two dimensional crystal lattice (Fig. 1.4). The richness of optical and electrical properties of graphene attracts physicists and chemists. Graphene exhibits extraordinary physiochemical properties like high carrier mobility at room temperature (Morozov, et al., 2008), good optical transparency (Nair, et al., 2008), excellent thermal conductivity (Balandin, et al., 2008) and unusual quantum hall effect (Zhang, et al., 2005). The near ballistic transport phenomena of charge carriers make graphene a potential material for nanoelectronics (Yazyev and Louie, 2010). Graphene shows remarkable optical properties. Its absorption spectra covers the entire ultraviolet to near infrared range (Pirruccio, et al., 2013) and the optical absorption of a single layer graphene is about 2.3 % of the incident light (Nair, et al., 2008). Graphene exhibit saturable absorption as a consequence of Pauli blocking (Bao, et al., 2009) and reverse saturable absorption due to nonlinear scattering (Wang, et al., 2011).

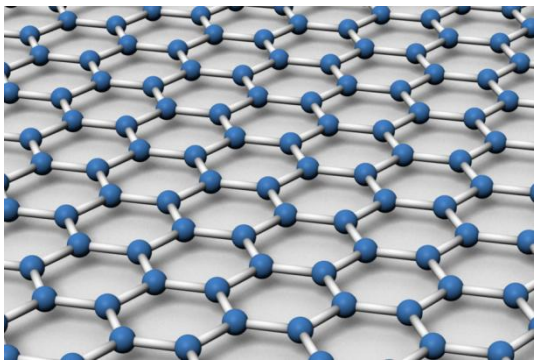

Figure 1.4. Schematic representation of graphene

Graphene can be synthesized by various methods including micromechanical cleavage of graphite, CVD, epitaxial method and chemical synthesis from graphite (Bae, et al., 2010; Novoselov, et al., 2004; Yang, W. et

al., 2013). Chemical preparation of graphene using graphite as the starting material is considered as one of the cost-effective method for the synthesis of graphene without compromising its electronic properties, transparency and sheet resistance. Brodie (1859) was the first to produce exfoliated graphite through oxidation. Hummers and Offeman (1958) presented a method for the oxidation graphite to graphitic oxide. Nowadays this oxidized graphite is extensively used for the preparation of high quality graphene. Graphene can be derived from the oxidized graphite by several routes such as thermal exfoliation, solar exfoliation, chemical and thermal reduction, hydrothermal treatment etc. (Acik, et al., 2011; Eswaraiah, et al., 2011; Zhou, et al., 2009; Zhu, et al., 2010) and the derived graphene found to retain certain oxygen impurities, is termed as reduced graphene oxide (rGO).

When rGO is suspended in a solvent, it has a strong tendency to irreversibly aggregate and restack due to strong π-π stacking and van der Waals interaction between the planar basal planes of graphene sheets. Inserting functional materials between the graphene layers prevent aggregation and facilitate tailored properties (Chen, L., et al., 2012; Nethravathi, et al., 2008b). Intercalating materials include conducting polymers, metal nanoparticles, semiconductor nanoparticles, etc. (Bai, et al., 2013; Murphy, et al., 2013; Parand, et al., 2014; Pham, et al., 2012; Remyamol, et al., 2013; Zhang, H., et al., 2009). The interaction between graphene sheets and these functional materials may be by electrostatic interaction, covalent bonding via chemical grafting, van der Waals attraction, hydrogen bonding or electron transfer (Compton, et al., 2011; Pham, et al., 2012; Remyamol, et al., 2014b; Zan, et al., 2014). The combinations of graphene with functional materials have broadened the scope of fundamental studies and applications.

Tremendous interest is devoted to fabricate graphene-semiconductor hybrid materials for light harvesting applications (Pan, et al., 2014; Peining, et al., 2012; Shao, et al., 2013). Strong and tunable light absorption by semiconductor nanoparticles create charge carriers. These charge carriers are readily accepted

and shuttled through the 2D graphene sheet, due to its high charge mobility (Lightcap, et al., 2010). These electron accepting and shuttling mechanism is demonstrated in several graphene hybrids like TiO_2, ZnO, CdSe and PdS (Jiang, et al., 2011; Krishnamurthy, et al., 2014; Williams and Kamat, 2009). Graphene-semiconductor hybrid systems find application in photovoltaics, photocatalysis, photodetectors and saturable absorption with superior performance to what have been achieved previously with individual technologies.

1.4. Graphene-ZnO hybrids

Willaims and Kamat (2009) demonstrated systematically the excited state interaction between ZnO and graphene oxide. The excited electrons in the conduction band of ZnO will migrate to rGO. This electron transfer mechanism will suppress the recombination of photo-induced electron-hole pairs and improve the conductivity (Lee, et al., 2009). ZnO is a visible-blind material, combining with graphene will modify its absorption spectral regime to visible region. This efficient charge separation, mobility and broadband absorption of ZnO/graphene hybrids point out the possibility of using this hybrid materials for various applications like photodetectors (Zhan, et al., 2012), light emitting diodes (Son, et al., 2012), photocatalysis (Li, et al., 2011), sensors (Singh, G., et al., 2012), etc.

ZnO/graphene hybrids can be synthesized in two ways. In the first approach, ZnO with desired shape and size synthesized in advance. It can bind to the surface of graphene by non-covalent interaction (Zhang, C., et al., 2014). In this method, either ZnO or graphene require modification with functional groups. The loading of nanoparticles depends on the type of functionalization and strength of interaction. Sometimes this method has the disadvantage of non-uniform wrapping of nanoparticles on graphene. By this approach, hybrids with desired properties can be prepared by controlling functionalization and loading of nanoparticles. In second method, ZnO is directly grown on the surface of graphene sheets. This *in-situ* growth method is widely used for the synthesis of ZnO/graphene hybrids.Graphene oxide (GO) is used as the precursor for

graphene, which is dispersed in a zinc source. During the nucleation of ZnO, simultaneous reduction of GO occurs (Lee, et al., 2009; Li and Cao, 2011; Singh, G., et al., 2012; Son, et al., 2012). This provides direct interaction with ZnO and can prevent the restacking and agglomeration of reduced graphene oxide sheets. Chemical techniques like solution precipitation, hydrothermal method, microwave-assisted method, etc. are used for this in-situ growth method (Liu, et al., 2013; Liu, et al., 2011; Zhou, et al., 2012).

By the fabrication of ZnO/graphene hybrid systems, we can control the morphology, surface defect states and the photoresponse of ZnO nanocrystals. For ZnO, the fastest growth direction is along the c-axis. During the growth of ZnO in presence of GO, the interaction of Zn^{2+} ions with oxygen functional groups of GO, can suppress the growth velocity of ZnO nanoparticles along c-axis (Kavitha, et al., 2013b; Pan, et al., 2014). Pan et al. (2014) observed that the variation of the concentration of GO can transform the morphology of ZnO from one-dimensional prismatic rod with pointed tip to a hexagonal tube with flattened tip while GO is effectively converted to rGO. In addition to the tuning of morphology, the addition of GO can modify the oxygen vacancies in ZnO. They observed the creation of oxygen vacancies on ZnO during the synthesis of rGO/ZnO. But Yoo et al. (2014) observed the filling of oxygen vacancies in ZnO. The alteration in morphology and defect engineering can vary the optical properties and conductivity of rGO/ZnO hybrids.

Visible light photoresponse is found in rGO/ZnO hybrids. This is either due to the narrowing of bandgap or the broad visible absorption in presence of carbon (Li, et al., 2012). One reason for bandgap reduction and resultant visible light absorption is carbon doping effect (Zhan, et al., 2012). The photoluminescence spectra of ZnO consist of excitonic UV emission and visible emission related to defects. In rGO/ZnO, it is observed that excitonic emission will quench significantly, indicating the charge transfer from the conduction band of ZnO to graphene layers. Son et al. (2012) revealed that the wavelength of excitonic emission can be modulated by conjugation of graphene with ZnO in the

form of a consolidated core shell structure. The visible emission in the hybrids depends on the nature of defects present in it (Yoo, et al., 2014). The deep understanding of the tailoring of optical properties will facilitate researchers for the fabrication of high performance optical devices.

Although graphene has many fascinating optical and electrical properties, its relative low light absorption coefficient and too fast recombination rate have limited graphene from practical optoelectronic applications. It is found that combining graphene with semiconductor nanoparticles like ZnO will improve the performance by photo-induced charge transfer of ZnO and electronic transport property of ZnO (Hayashi, et al., 2011; Song, W., et al., 2014). ZnO is a well known UV photoconductor while photoconductors based on ZnO/graphene heterostructures can be used in UV as well as visible spectral regime (Li, et al., 2012; Liu, et al., 2014). Visible light photocurrent generation and photodetection is important in various applications including biological and environmental research, sensing, etc. The photocurrent generation and detection in graphene based devices depend on the photoresponse of Schottky junctions at the contact interfacial area (Ghosh, et al., 2010). Pristine graphene based devices have reduced performance due to poor interfacial contact. Graphene-semiconductor hybrid devices will help to overcome this drawback, and assist in utilization of the fascinating properties of graphene. The visible light photoreponse in ZnO depends on many factors like defect concentration, processing conditions, grain boundaries, etc. Upon illumination, electron-hole pairs are generated in ZnO. The rapid photoresponse of ZnO/graphene hybrids is enabled by the efficient charge separation and transport facilitated by the graphene sheets in contact with the photoexcited ZnO.

Graphene shows strong and broadband optical nonlinearity, because of its unique band structure and possible optical transitions in all wavelength. Pristine graphite shows saturable absorption because of Pauli blocking (Bao, et al., 2009). If the Fermi level is tuned away from the Dirac point, by more than half of the photon energy, the optical transitions get Pauli blocked, reduces the

absorption of graphene (Gan, et al., 2013). Graphene based saturable absorbers are used in fiber laser mode locking. However, graphene dispersions exhibit broadband optical limiting response in graphene dispersions (Wang, J.,et al., 2009). Here the nonlinearity originated from nonlinear scattering of thermally induced bubbles and microplasmas (Wang, J., et al., 2011). Recently large number of graphene hybrids is prepared and they exhibit reverse saturable absorption, nonlinear scattering and two-photon absorption. The enhanced nonlinear optical properties of these hybrids are a combination of nonlinear optical (NLO) mechanisms from graphene and the other NLO material. The possibility of photoinduced electron or energy transfer in the hybrid materials, which provides a good approach to obtain materials with high value NLO properties.

Covalent or noncovalent combinations of NLO materials are a good approach to improve the NLO properties of the hybrid materials. Porphyrin and fullerene are covalently functionalised with graphene sheets (Liu, Z. B., et al., 2009) and it is found that nanohybrids offer limiting performance superior to that of the individual moieties. Even though porphyrin and phthalocyanine have excellent nonlinear optical response, lack of proper stability against thermal (Guermeur, et al., 1997) and optical bleaching (Bonnett and Martinez, 2000) limit their potential applications. The fabrication of graphene-based materials with Zinc oxide nanoparticles may expect to overcome this disadvantage, because ZnO nanoparticles have good stability under prolonged laser irradiation. These ZnO decorated graphene sheets exhibit good nonlinear absorption than its individual counterparts, which may be due to the two-photon absorption with reverse saturable absorption and photo-induced charge transfer between ZnO and graphene sheets.

Taking into account the excellent properties of ZnO and graphene, their hybrid can enable versatile properties with competence far beyond those of the individual members. The use of such hybrids to fabricate optoelectronic devices may offer advantages like lightweight, good stability and optical transparency. The aim of this thesis is to explore the interfacial interaction between intrinsic

defects in ZnO nanostructures and graphene and demonstrate how the charge transfer pathways modify its visible photoconductivity and nonlinear optical properties

1.5. Scope and objectives of the thesis

ZnO possess tunable optoelectronic properties like photoluminescence, carrier mobility, photoconducting behaviour and nonlinear absorption. Tailoring the morphology and crystal facets of ZnO nanocrystals will facilitate the modification of intrinsic defects, which in turn vary the optoelectronic properties of ZnO. Inspired by the reactivity and charge carrier separation of polar facets of ZnO, we have focused on the synthesis of cone shaped nanostructures, as it possesses more exposed oxygen terminated facets. This high energy polar surface also has a good affinity towards graphene sheets during the preparation of graphene-ZnO hybrid material. Recent literature shows that considerable effort has been made to attach ZnO nanostructures on graphene sheets for optoelectronic applications. The nature of defects and carrier dynamics play an important role in altering the interfacial interaction and charge transfer mechanism in ZnO/graphene systems. A systematic understanding on tailoring of defects in ZnO and ZnO/graphene hybrids will be beneficial for the fabrication of high performance devices.

Based on this outlook, the main objectives of the present work are

1. Synthesis and characterization of ZnO nanocones by solution precipitation and hydrothermal methods, influence of capping agents, pH of the precipitating medium and calcination temperature on the morphology of ZnO nanostructures and the prediction of its formation mechanism.

2. Analysis of the nature of surface defects by photoluminescence and lifetime measurements and measurement of visible light photocurrent and nonlinear absorption of the nanostructures

3. Synthesis of ZnO/graphene hybrids by solution precipitation and hydrothermal methods, its characterization and study the correlation of visible light photoconductivity and nonlinear absorption with surface defect states.

4. Fabrication of ZnO/graphene hybrid films by layer-by-layer self assembly technique using polycationic and polyanionic polymer matrices, study its photocurrent and nonlinear optical properties.

1.6. Organization of the thesis

Chapter 1 gives an overview about ZnO and its hybrid with graphene. The nature of the defect states in ZnO, and its effect in below bandgap absorption is discussed. The mechanism of photoconductivity and nonlinear absorption is described. The general features of graphene and the importance of ZnO/graphene hybrids is also discussed.

Experimental procedures for the synthesis of ZnO and reduced graphene oxide/ZnO hybrids and its film fabrication method are described in chapter 2. The various characterization techniques like scanning electron microscopy, transmission electron microscopy, X-ray diffraction, X-ray photoelectron spectra, IR spectra, UV-vis absorption spectra and photoluminescence are detailed. The experimental set up for the measurement of nonlinear absorption and photocurrent generation is also demonstrated.

Chapter 3 put forward the facile solution method for the synthesis of ZnO nanocones. The influence of reaction conditions like pH, effect of capping agent, and calcination temperature are discussed. Based on the observation of

morphology and crystallization conditions, a growth mechanism for the formation of nanocones is proposed.

The tailoring of surface defects in ZnO nanocones is discussed in chapter 4. With the help of photoluminescence and lifetime measurements, the nature of defects in ZnO is identified and it is correlated with the photoconductivity and nonlinear absorption.

Chapter 5 describes the synthesis of rGO/ZnO by solution method. The extent of deoxygenation of graphene oxide is identified by structural characterization. Photoluminescence demonstrates how the defects in ZnO are modified in presence of reduced graphene oxide and explained how this modification varies its photoconductivity and optical limiting properties.

Layer-by-layer self assembly method to fabricate rGO/ZnO films is proposed in chapter 6. Combining the advantages of ZnO with visible light absorption and graphene with extremely high carrier mobility, these reduced graphene oxide/ZnO films are used for photocurrent generation and nonlinear absorption.

The major results and outcome of this research work are summarised in Chapter 7. Finally, the future possible applications are suggested.

CHAPTER 2
EXPERIMENTAL

This chapter describes the experimental procedure for the synthesis of ZnO and reduced graphene oxide/ZnO hybrids and their film fabrication methods. Various characterization techniques, open aperture Z-scan technique for the measurement of nonlinear absorption and electrochemical experiments for photoconductivity studies are also discussed.

2.1. Synthesis

2.1.1. Materials

Zinc acetate dihydrate ($Zn(Ac)_2$. $2H_2O$), 98 % acetic acid (CH_3COOH), sodium hydroxide (NaOH), 35 % hydrochloric acid (HCl), 98 % sulfuric acid (H_2SO_4), potassium permanganate ($KMnO_4$), 30 % hydrogen peroxide (H_2O_2), acetone and 2-propanol are purchased from Merck India and used as-received. Graphite powder (particle size < 20 μm), polyvinyl pyrrolidone (PVP, average mol. wt. 40,000), poly(sodium 4-styrene sulfonate) (PSS, average mol. wt. 70,000), polyacrylamide (PAM mol. wt. 5,000,000 – 6,000,000) and fluorine doped tin oxide (FTO) coated glasses (surface resistivity ≈ 8 Ω/sq) are received from Sigma Aldrich.

2.1.2. Synthesis of ZnO nanocones

2.1.2.1. Solution precipitation method

1 mmol of zinc acetate dehydrate (0.219 g) is stirred with 0.05 % PVP solution (in 1 % acetic acid) for 24 h to form zinc acetate-PVP complex. ZnO is precipitated from this complex using NaOH solution. The molar ratio of zinc acetate and NaOH solution is 1:6. The stirring is continued for 12 h to complete the precipitation. The precipitate is filtered and dried at 100 ^oC in air and a part of the dried sample is heated at 550 ^oC in air.

2.1.2.2. Hydrothermal method

1 mmol of zinc acetate dehydrate (0.219 g) is stirred with 0.05 % PVP solution (in 1 % acetic acid, 30 ml) for 24 h. For the precipitation of ZnO, 6 mmol of NaOH solution is added. The colloid formed is stirred for 30 min, after that it is transferred to a 50 ml Teflon-lined stainless steel autoclave and heated in an oven for 7 h at 100 ^{o}C. After cooling to room temperature, the product is collected by filtration, washed with distilled water and dried. A portion of as-prepared ZnO is heated at 550 ^{o}C in air.

2.1.3. Synthesis of graphene oxide (GO)

GO is synthesized by a novel strategy adopted by simplifying Hummers method (Hummers and Offeman, 1958). GO is prepared by chemical oxidation of graphite powder at low temperature. Graphite powder is stirred with 98 % sulphuric acid for 12 h at room temperature. This mixture is cooled below 10 ℃ and potassium permanganate is gradually added. The reaction mixture is stirred for 2.5 h while keeping the temperature below 10 ℃. Then 50 ml distilled water is added and stirred at room temperature for 30 min. The reaction is terminated by addition of water and 30 % H_2O_2. The dispersion is washed by centrifugation and decantation. The final product is dried at 60 ^{o}C under vacuum for 12 h.

2.1.4. Synthesis of reduced graphene oxide/ZnO (rGO/ZnO)

2.1.4.1. Solution precipitation method

1 mmol of zinc acetate dehydrate (0.219 g) is stirred with 0.05 % PVP solution (in 1 % acetic acid) for 30 min to form zinc acetate-PVP complex. GO is added to the above mixture and sonicated to get a uniform dispersion, followed by stirring for 24 h. Three different masses of GO namely 10 mg, 20 mg and 30 mg are added to the zinc acetate-PVP solution. For precipitation of ZnO, 6 mmol of NaOH solution is added, the colloid formed is again stirred for 12 h at room temperature. The precipitate is filtered and dried at 100 ^{o}C. The samples are designated as SG10, SG20 and SG30 for 10 mg, 20 mg and 30 mg of GO, respectively.

2.1.4.2. Hydrothermal method

1 mmol of zinc acetate dehydrate (0.219 g) is stirred with 0.05 % PVP solution (in 1 % acetic acid, 30 ml) for 30 min to form zinc acetate-PVP complex. GO is mixed to the above mixture by sonication and this solution is stirred for 24 h to get a uniform dispersion. After that, ZnO is precipitated by the addition of NaOH. The colloid formed is stirred for 30 min, and it is transferred to a 50 ml teflon-lined stainless steel autoclave, heated in an oven at 100 ^{o}C for 7 h. After cooling to room temperature, the product is collected by centrifugation, washed with distilled water, and dried at 100 ^{o}C. The samples are designated as HG10, HG20 and HG30 for 10 mg, 20 mg and 30 mg of GO, respectively.

2.1.5. Synthesis of poly (sodium 4-styrene sulfonate) coated reduced graphene oxide (PSS-rGO)

Stable aqueous dispersion of polymer coated graphitic nanoplatelets can be prepared by exfoliation and *in-situ* reduction of graphene oxide in presence of PSS (Stankovich, et al., 2006). 1 mg/ml of aqueous solution of GO is prepared by ultrasonication to form a colloidal suspension. 4 g of PSS is dissolved in 100 ml of the colloidal solution of GO followed by the addition of 100 μL hydrazine hydrate and it is refluxed at 70 ^{o}C for 4 h. A stable suspension of PSS coated reduced graphene oxide (PSS-rGO) is obtained and it is repeatedly washed with distilled water until the pH of the colloid become neutral. This aqueous dispersion is stable for several months.

2.2. Film Fabrication

2.2.1. Fabrication of reduced graphene oxide/ZnO (rGO/ZnO) films by electrostatic layer-by-layer self assembly technique

Electrostatic layer-by-layer self assembly technique is a versatile and economic method to fabricate multilayer films with controllable surface

morphology and properties. By means of this technique rGO/ZnO multilayer films are fabricated. The multilayer films are deposited on quartz and FTO coated glass substrates. Quartz slides are cleaned by immersing in freshly prepared piranha solution (98 % H_2SO_4 to 30 % H_2O_2 by 7:3 v/v), followed by rinsing with distilled water and dried by purging N_2. FTO coated glass slides are cleaned by sonicating in soap solution, 2-propanol and acetone. The multilayer films are fabricated by alternate spin coating of positively charged 4 % polyacrylamide solution (pH = 4) containing 0.5 mg/ml of ZnO and negatively charged solution of PSS-rGO (0.5 mg/ml, pH = 9). These two solutions are spin coated at 500 rpm for 120 s and followed by 3000 rpm for 30 s. After coating each layer, the substrate is rinsed with distilled water at 3000 rpm for 30 s, to remove the weakly adsorbed materials. This sequence is repeated to get desired number of layers, designated as $(PAM\text{-}ZnO/PSS\text{-}rGO)_n$, where n is the number of bilayers. After spin coating the films are dried at room temperature. The multilayer films coated on quartz substrate is used for recording the UV-vis absorption spectra. The films on FTO substrate is used for the measurement of nonlinear absorption and as working electrode for the photocurrent measurement.

2.2.2. Fabrication of films of ZnO, rGO/ZnO and PSS-rGO for photocurrent measurement

Thin films of the samples are fabricated on clean FTO glass slides. 0.5 mg/ml of ZnO or rGO/ZnO is dispersed in 4 % aqueous solution of PAM by sonication. This uniform dispersion is spin coated on FTO by a two step process at 500 rpm for 120 s and 3000 rpm for 30 s and the coated films are dried at room temperature. PSS-rGO films are spin coated using the suspension of as-prepared PSS-rGO, adjusted its concentration as 0.5 mg/ml by adding water. For the photocurrent measurement, all the films are coated nine times continuously.

2.3. Characterization Techniques

A combination of spectroscopic, thermal and microscopic techniques are

employed to analyze the materials synthesized for this research work. Fourier transform infrared spectroscopy (FTIR) is used to understand the structural features of the samples. Raman spectroscopy is used to analyze the percentage defects in samples containing graphene. Crystallinity of the samples is analyzed using X-ray diffraction studies (XRD). X-ray photoelectron spectroscopy (XPS) is used to analyze the elemental composition of the samples and extent of reduction in graphene containing samples. Thermal decomposition pattern of the samples is studied using thermogravimetric analysis (TGA). Characteristic absorption and emission of the samples are studied using UV-vis absorption spectroscopy and fluorescence spectroscopy respectively. Time correlated single photon counting (TCSPC) technique is used to measure the decay transient and emission life time of ZnO samples. Size, morphology and surface features of the samples are studied by various microscopic techniques like scanning electron microscopy (SEM) and transmission electron microscopy (TEM).

2.3.1. Spectroscopic techniques

2.3.1.1. Fourier transform infrared spectroscopy

Infrared spectroscopy is the most popular chemical characterization technique for structural analysis. An infrared spectrum gives characteristic absorption peaks corresponding to the vibrational frequency of bonds between the atoms in the material. In an infrared spectrometer, infrared radiation of successively increasing wavelength is passed through the sample and the percentage of absorbance is measured. During exposure to the radiation, some of the incident frequencies will be in resonance with the molecular vibrations. This resonance allows the exchange of energy between the incident electromagnetic wave and the molecular vibrations and the absorbed frequencies are recorded as a spectrum. The Fourier transform spectrometer contains an interferometer that produces a Fourier spectrum which gives the distinct frequencies absorbed from the IR spectrum. By utilizing the FTIR spectroscopy a significant improvement in the quality of the infrared spectra and acquisition time is achieved.

The instrument used for the present study is Perkin Elmer 100 FTIR spectrometer with diffuse reflectance accessory. Spectral range and optical resolution of the instrument is 4500-400 cm^{-1} and 0.5 cm^{-1} respectively. The samples are diluted with KBr before the measurement and each sample is scanned 32 times.

2.3.1.2. Raman spectroscopy

Raman spectroscopy is a light scattering technique, an exceedingly useful tool to study fundamental excitations in solids and molecules, because light can be scattered inelastically so that the incident and scattered light have different frequencies and this frequency difference is related to the properties of each material. The inelastic scattering of light is called Raman Effect. Raman spectroscopy is identified as powerful tool to analyse graphitic materials (Ferrari, 2007). Two prominent features of Raman spectra of graphene are the G band and the 2D band (also called G''), which is the characteristic of graphene without defects. The D and D' bands are two additional peaks arising from defects. The E_{2g} point symmetry gives rise to the G band and it is due to the in plane stretching of sp^2 carbon. The D band is attributed to the breathing mode of κ-point phonons in A_1' symmetry and its intensity is dependent on the amount of lattice defects. The ratio of the intensities of D band to G band (I_D/I_G) is the measure of disorder or imperfections in the sp^2 carbon lattice.

The Raman spectrum of the powder samples under study is recorded in WiTech alpha 300 Raman system excited with 488 nm.

2.3.1.3. X-ray diffraction studies

XRD is a very useful tool to identify crystalline phases and orientation and it can also provide information on unit cell dimensions. Since the wavelength of X-rays matches with inter atomic bond length, X-rays can produce diffraction pattern when pass through a crystal. These diffraction patterns reveal information about the internal structure of the crystal. The dominant effect that occurs when an

incident beam of X-rays interacts with a solid material is the scattering of the X-rays from atomic lattices within that material. In crystalline materials, the scattered X-rays undergo constructive and destructive interference and it is described by Bragg's Law (Equation 2.1).

$$n\lambda = 2d\sin\theta \tag{2.1}$$

The directions of possible diffractions depend on the size and shape of the unit cell of the material. The intensities of the diffracted waves depend on the kind and arrangement of atoms in the crystal structure. When a powder with randomly oriented crystallites are placed in an X-ray beam, the beam will see all possible inter atomic planes. If the scanning angle of the detector is systematically changed, all possible diffraction peaks from the powder will be detected. Calculation of d-spacing from diffraction peaks allows the identification of the material, because each material has a set of unique d-spacing. X-ray diffraction pattern also allows estimating crystal size by Scherrer equation as given in equation 2.2. This equation gives the relationship between diffraction peak broadening (B) and crystallite size (D).

$$D = \frac{0.9\lambda}{B\cos\theta} \tag{2.2}$$

Bruker AXS D8 advance X-ray diffractometer with Cu Kα (λ=1.54 Å) radiation is used for XRD studies of the synthesized powder samples. XRD pattern is recorded in the range $2\theta = 5^{o}$ to $2\theta = 80^{o}$.

2.3.1.4. X-ray photoelectron spectroscopy

XPS is an analysis technique that uses X-ray in ultra high vacuum environment to investigate chemical composition and chemical states of compounds on a surface. XPS is based on the interaction between X-rays and electrons. The incident X-rays collide with core electrons and get ejected from the electronic shell. The ejected electrons will possess certain kinetic energy that can be related to the binding energy of electron to the atom. The ejected inner electrons will create holes in the electronic shell. Since it is an unstable state

electrons from the valence shell fills this hole, causing an auger electron to be emitted from the valence shell. We can calculate the binding energy (BE) of the electron using the equation 2.3, where λ is wavelength of incident X-ray, KE is its kinetic energy and φ is a correction factor depending on the instrument.

$$BE = \frac{hc}{\lambda} - KE - \varphi \tag{2.3}$$

Since the binding energy is unique for each element, we can identify the elements. The spectrum is recorded by measuring the kinetic energy and number of electrons ejecting from the material by irradiating with a beam of soft X-rays (with a photon energy of 200-2000 eV). In an XPS spectrum binding energy of a particular peak not only depends on the element but also the chemical environment and energy states of the atom. Any change of the chemical environment and state which perturb the energy level of the atom, will cause change in the XPS spectrum. Moreover, the intensity of the peaks is related to the concentration of the element. Thus, the technique provides a quantitative analysis of the surface composition.

In our studies, Kratos Axis ultra photoelectron spectrometer with a monochromatic Al Kα X-ray source (1486.6 eV) is used to study the elemental composition of the sample. The samples under study are in the powder form

.

2.3.1.5. Ultraviolet-visible absorption spectroscopy

When a molecule is irradiated with UV or visible light, it will undergo electronic excitation by the absorption of light. The principal characteristics of absorption band are the position and intensity. The position of absorption band corresponds to the wavelength of radiation whose energy is equal to that required for the electronic transition from ground state to the excited state. The intensity of absorption can be derived from Beer Lamberts law: $A = \epsilon cl$, where A is the measured absorbance, ϵ is the absorptivity and c is the concentration of the solution. UV-vis absorption spectrum is a powerful technique for the characterisation of semiconductor nanomaterials. Here the optical absorption is

based on the excitation of electrons from the valence band to the conduction band, creating an electron-hole pair. Further, the optical bandgap of these nanoparticles can be calculated using the equation 2.4 (Tauc, 1966).

$$\alpha h\nu = C(h\nu - E_g)^n \tag{2.4}$$

where C is a constant, α is the molar extinction coefficient, $h\nu$ is the incident photon energy, E_g is the optical bandgap and n is a factor that determines the electronic transition, $n = 1/2$ for materials with direct bandgap and $n = 1$ for indirect bandgap materials.

The light source commonly used is deuterium discharge lamp for UV measurements and a tungsten-halogen lamp for visible and NIR measurements. A combination of photomulplier tube and a Peltier-cooled PbS IR detector is used in UV-visible-NIR spectrometers.

Optical absorption measurements of the powder samples are recorded by dispersing in water using Cary 100 Bio UV-visible spectrophotometer.

2.3.1.6. Steady state photoluminescence and time correlated decay measurements

Photoluminescence (PL) is the spontaneous emission of light upon optical excitation. The emission takes place from the lowest vibrational state of the excited state to the ground state. The photoluminescence spectrum shifts to higher wavelength compared to its absorption spectrum which can be illustrated by the Jablonski diagram as shown in Fig 2.1. When continuous wave excitation is used in a PL experiment, the system quickly converges to a steady state, since the rate of excitation equals the rate of recombination. The PL spectrum provides the transition energies, which can be used to determine electronic energy levels. The PL intensity gives a measure of the relative rates of radiative and nonradiative recombination. PL usually originates from the surface of the material, so it is an important tool to measure the surface characteristics.

Lifetime is defined as the time taken by an ensemble of excited molecules decay to 1/e of their initial excited state population. The fluorescence lifetime thus refers to the average time that a molecule stays in its excited state before emitting a photon. When the surface states act as trap states, it can alter the time correlated PL radiative transitions. When a material is excited by a series of short laser pulses, the concentration of carriers depends strongly on time. Because the laser pulse can be much shorter than the average recombination time, a specific carrier density can be generated almost instantaneously. The photoexcited carriers then recombine at a rate that is characteristic of the recombination path they follow.TCSPC measurements can be used to determine carrier lifetimes, and to identify and characterize various recombination mechanisms in the material.

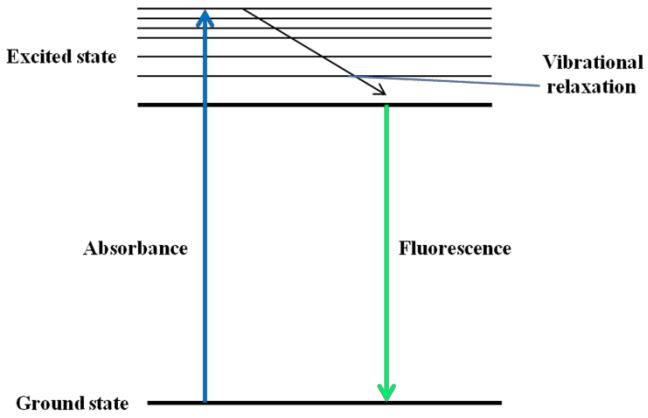

Figure 2.1 Scheme of absorption and emission

A steady state fluorescence spectrometer (spectrofluorometer) contains a sample holder, a xenon lamp, monochromators, focussing optics and a detector. The detector is commonly kept at 90 degrees to the light source. Jobin Yvon Flurolog 3-11 spectrofluorometer is used for the measurements of the samples under study. The samples are dispersed in water (1 mg in 10 ml). The time correlated decay transients are measured using TCSPC technique. The samples are excited using 340 nm laser source (pulse duration <1 ns) and the emission life times were measured using the Horiba Jobin Yvon single photon counting system.

2.3.2. Thermogravimetric analysis

TGA records weight change in a material subjected to temperature variation in a controlled atmosphere. TGA provides information about physical as well as chemical properties of materials (Bottom, 2008). A thermogravimetric analyzer consists of a sample pan with a precision balance. The pan is heated or cooled in a furnace during the experiment. Usually a null type balance with a sensing element is used to detect change in mass. The sample environment is controlled by a purge gas, which may be inert or reactive. The heating can be programmed in a controlled rate. Usual sample size is between 1 mg to 10 mg.

Thermal studies of the samples are done using thermogravimetric analyzer (TGA Q50, TA instruments) at a heating rate of 10 ^{o}C/min under nitrogen atmosphere from room temperature to 800 ^{o}C.

2.3.3. Microscopic Techniques

2.3.3.1. Scanning electron microscopy

SEM enables the investigation of specimens with resolution down to the nanometer scale. It uses focused beam of high energy of electrons to generate variety of signals at the surface of the specimen. The signals which are generated when incident electrons are decelerated on the sample surface are secondary electrons, back scattered electrons and X-rays. Secondary electrons and backscattered electrons are commonly used for imaging samples: secondary electrons are most valuable for showing morphology and topography on samples and backscattered electrons are most valuable for illustrating contrasts in composition of multiphase samples. X-rays are generated by inelastic collisions of the incident electrons with electrons in discrete orbital of atoms in the sample. As the excited electrons return to lower energy states, they yield X-rays which is the characteristic of the elements in the sample (Goldstein, et al., 2003).

For SEM imaging, the specimen must be electrically conductive at least at the surface to prevent the accumulation of electrostatic charge on the surface. When scanned by the electron beam, nonconducting specimens tend to charge and these causes scanning faults. So the specimens are usually coated with conducting materials like gold.

The morphology of the samples are analyzed using FEI Quanta FEG 200 high resolution scanning electron microscope.

2.3.3.2. Transmission electron microscopy

TEM uses beam of electrons accelerated with high voltage (up to 300 kV). When this electron beam transmits through an ultra thin specimen (nearly 200 nm), it gets scattered. The scattering of the electrons during the transmission determines the kind of information about the sample. Through elastic scattering, diffraction patterns can be observed. The diffraction mode displays accurate information about the local crystal structure. The inelastic interaction between the primary electrons and the electrons from the sample at the heterogeneities of the nanostructures causes a complex absorption and scattering effects. This will produce spatial variations in the intensity of the transmitted electrons, which can be distinguished by the detector during image formation. This imaging mode provides a highly magnified view of the micro- and nanostructures and ultimately, in the high resolution imaging mode a direct map of atomic arrangements can be obtained (high resolution TEM).

For imaging using TEM, samples dispersed in 2-propanol is placed on the inner meshed area of TEM grid made up of Cu. It has a diameter of 3 mm with a thickness and mesh size ranging from few to 100 μm. The sample is dried under vacuum before imaging. TEM imaging is done using FEI Tecnai G230 high resolution transmission electron microscope.

2.4. Nonlinear absorption measurement

The change in transmittance of a medium as a function of input light intensity or fluence is referred to as nonlinear absorption or nonlinear transmittance. Open aperture Z-scan technique is quite popular to measure nonlinear absorption, due to its simplicity in determining and interpreting nonlinear changes in absorption (Sheik-Bahae, et al., 1990). In the open aperture Z-scan experiment, a laser beam is first split by a beam splitter. The reflected light was recorded by detector 1, as a reference. The transmitted light is focused using a lens. The direction of beam propagation is taken as the z-axis, and the focal point is considered as z = 0. The z value increases towards either side of the focal point, but the sign will be negative on one side and positive on the other. The sample is now placed in the beam at a position (z) between the lens and the focal point, and the transmitted laser energy is measured. Then the sample is moved in small steps towards the focus and beyond, and the transmission is measured at each step. At each of these positions the sample will experience different laser intensity, and the intensity will be maximum at the focus. The transmittance is measured continuously while the sample is slowly translated from a position before the focus to a position after the focus by the detector 2. A schematic of the open aperture Z-scan setup can be seen in Fig 2.2.

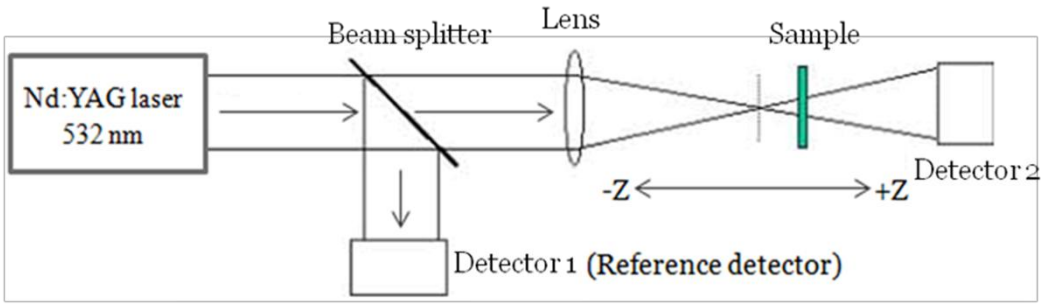

Figure 2.2. Open aperture Z-scan experiment set-up for measuring the nonlinear absorption properties of the materials (Sheik-Bahae, et al., 1990)

In open aperture Z-scan technique, the entire energy transmitted through the sample is collected. So the reduction in transmittance measured is independent of the nonlinear refraction and thus can be used to determine the nonlinear absorption coefficient. The nonlinear absorption coefficient can be extracted by fitting the experimental data with the Z-scan theory.

A Q-switched Nd:YAG laser (Minilite continuum) with pulse width of 5 ns at the excitation wavelength of 532 nm operating at single shot mode is used for exciting the samples. The spatially Gaussian laser beam is focused by a converging lens of 10 cm focal length and the sample is moved along the beam axis in small steps such that it passes through the focal point. The light intensity is maximum at the focal point and it reduces symmetrically to either side on the beam axis. The far-field sample transmittance is measured as a function of sample position (z).as a source and a lens is used to focus the laser. While moving the sample through the focus along the laser direction, the input energy as well as the transmitted energy are measured by two similiar pyroelectric energy probes (RjP 735, Laser Probe Corp.), which are connected to an energy meter (RJ7600, Laser Probe Corp.). In the Z-scan experiment, the thickness of the sample L should be smaller than the Rayleigh length of the focused beam ($L < Z_0 = \pi\omega_0^2 / \lambda$, ω_0 is the beam waist). In this case, the sample length is small enough that changes in the beam diameter within the sample due to either diffraction or nonlinear refraction can be neglected.

For the measurements, ZnO and ZnO/graphene powder are dispersed in water (1 mg/ml) is taken in a 1 mm thick quartz cuvette and is placed at the focus of the lens and scanned on either side of it.

For the nonlinear absorption, material satisfies the attenuation equation,

$$\frac{dI}{dz'} = -(\alpha + \beta I) I \qquad (2.5)$$

where α, β are the linear absorption and two photon absorption coefficients, respectively.

For a pulsed laser beam that is temporally and spatially gaussian, the transmittance in presence of two-photon absorption process is expressed as

$$T(z) = \frac{(1-R)^2 e^{-\alpha L}}{q_0 \sqrt{\pi}} \int_{-\infty}^{+\infty} \ln\left[1 + q_0 \exp(-x^2)\right] dx \tag{2.6}$$

where R is the Fresnel reflection at the interface of the material with air, L is the length of the medium and q_o is given by

$$q_o = \beta I_0 L_{eff} \tag{2.7}$$

where I_0 is the peak on-axis intensity incident on the material and L_{eff} is effective length of the medium given by

$$L_{eff} = (1 - e^{-\alpha L}) / \alpha \tag{2.8}$$

2.5. Photocurrent generation and electrochemical impedance measurement

Photocurrent generation and electrochemical impedance experiments are conducted using Autolab electrochemical work station (AUT83909 potentiostat/ galvanostat). in a conventional three electrode electrochemical cell comprising of the thin film sample as the working electrode, platinum wire as counter electrode and Ag/AgCl as a reference electrode. 0.2 M Na_2SO_4 taken in a quartz beaker is used as the electrolyte solution. The active area of the working electrode is 0.25 cm^2. The potential of the working electrode is set at –0.5 V against the Ag/AgCl reference electrode. An incandescent lamp operating at 300 W is used as the illumination source. The photointensity is measured using digital solar meter

(Daystar) which uses polycrystalline silicon photovoltaic cell as the sensor. The light intensity chosen for the measurement is 80 mW/cm^2. The photoresponse property of the samples under white light illumination is studied by measuring the photocurrent growth and decay of the samples by repetitive switching of the illumination (on/off) at an interval of 60 s using a stop watch. The photocurrent is calculated by taking difference between the observed current after the illumination of the sample and the dark current. Schematic representation of the experimental set up is given as Fig. 2.3.

$$\text{Photocurrent} = I_{light} - I_{dark} \qquad (2.9)$$

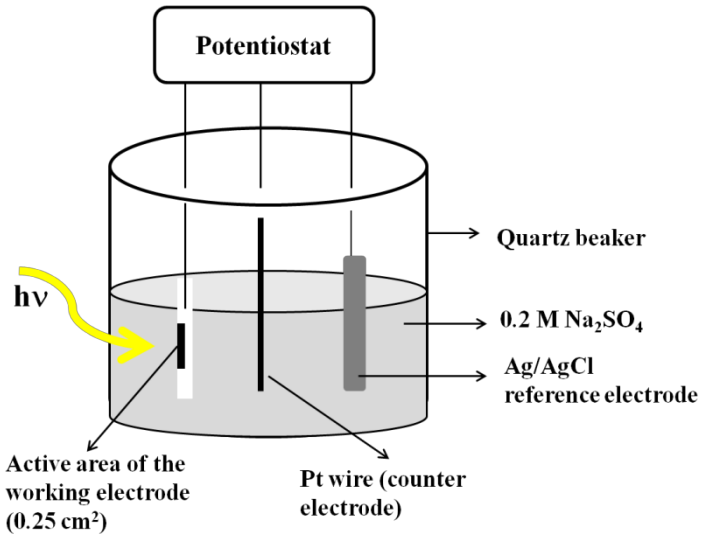

Figure 2.3. Experimental set-up for measuring the photocurrent generation

For all the samples, electrochemical impedance spectra (EIS) are recorded in the frequency range 0.01 Hz to 100 KHz by applying a small AC signal with amplitude 10 mV with a static potential of –0.5 V.

CHAPTER 3
SYNTHESIS AND CHARACTERIZATION OF ZnO NANOCONES

In this chapter, facile solution methods (solution precipitation and hydrothermal method) for the synthesis of ZnO nanocones using polyvinyl pyrrolidone are discussed. Here polyvinyl pyrrolidone has pivotal role in the crystallization of ZnO by its excellent adsorption ability. Based on the observation of morphology and crystallization conditions, growth mechanism for the formation of nanocones is also proposed.

3.1. Introduction

ZnO, owing to its low cost, ease of preparation, abundance, nontoxicity and good carrier mobility, is considered to be an important semiconductor in light-induced applications. Recently numerous researchers have been focusing on new synthetic methods to control shape, size and crystallinity of ZnO nanomaterials, which are important in tailoring their physical and chemical properties. ZnO is an n-type semiconductor material with a wide and direct band gap of 3.37 eV and a large exciton binding energy of 60 meV at room temperature. It is an intrinsic semiconductor because of the presence of oxygen/zinc vacancies or interstitials. These native point defects are the cause of conductivity and controlling these native defects is very crucial for using ZnO for various applications. ZnO has been identified as a good optoelectronic material used in optical limiting devices (Min, et al., 2009), photodetectors (Reyes, et al., 2012), solar cells (Zhang,Q. et al., 2009), light emitting diodes (Kim, et al., 2009), photocatalyst (Jiang and Gao, 2005), etc., due to its tunable optoelectronic functions like absorption (Zhan, et al., 2014), photoluminescence (Joshi, et al., 2014), bandgap (Singh, J. et al., 2012), carrier mobility and photoconducting behaviour (Bang, et al., 2012).

The tremendous interest in ZnO is provoked by its multifunctional characters, which can be varied by controlling the morphology and crystallinity. ZnO is a polar crystal with hexagonal wurtzite structure, consisting of positive (0001) plane rich in Zn^{2+} ions, negative $(000\bar{1})$ plane rich in O^{2-} ions, polar $(10\bar{1}1)$ O^{2-} terminated plane (Zuniga Perez, et al., 2005) and nonpolar $(10\bar{1}0)$ plane with alternate Zn^{2+} and O^{2-} ions. The growth velocities of different crystal planes in solution, follows the order $(0001) > (10\bar{1}1) > (10\bar{1}0) > (000\bar{1})$ (Li, et al., 1999). Therefore one dimensional nanostructure with elongation along (0001) plane is the most common morphology in ZnO (Ahn, et al., 2008; Singh, J. et al., 2012; Xu, et al., 2005). Recent advances in chemical synthesis and deep understanding of crystal structure have enabled the achievement of ZnO nanostructures with an increased degree of structural complexity and shape. By adjusting the growth velocity of different crystal planes and passivating high energy polar surfaces, different morphologies like sheets (Chang and Waclawick, 2012), cubes (Feng, et al., 2009), cones (Chang, et al., 2013) spheres (Zhang, G. et al., 2011), etc. can be prepared.

Tailoring the morphology and crystal facets of ZnO nanocrystals will facilitate the modification of intrinsic defects which in turn vary the optoelectronic properties. For example, Alenezi et al. (2013) synthesized ZnO nanowires, nanodiscs and nanostars with different ratio of exposed polar to nonpolar facets. Nanodiscs exhibit high intensity visible photoluminescence due to more surface defects caused by the exposed polar facets. Kuo et al. (2014) demonstrated that the influence of length and orientation of ZnO nanowires on dye absorption and carrier transport in dye sensitised solar cells. Chang et al. (2013) compared the power conversion efficiency of ZnO nanocones and nanorods. The nanocones show higher photoconversion taking the advantage of reactive oxygen terminated $(10\bar{1}1)$ facet to control the dye aggregation on this surface. Recent literatures also revealed that polar surface of ZnO nanocrystals leads to higher photocatalytic activity (Boppella, et al., 2013; Zeng, et al., 2009). The polar surfaces are important in ZnO heterostructures due to the favourable

photogenerated carrier separation and effective transfer of photoexcited holes and electrons (Wang, X. et al., 2011).

ZnO nanostructures with control over the exposed facets can be synthesized by chemical vapour deposition (Hani, et al., 2009) and thermal evaporation (Khanderi, et al., 2009). However, complex process control and sophisticated equipment are needed for the vapour phase methods. Solution method is simple and effective way to prepare highly crystalline ZnO nanostructures. By solution method different nanostructures can be synthesized without using any metal catalyst or template comparatively at low growth temperature with good crystal quality. But understanding of the relevant parameters on the kinetics and growth of the nanoparticles in the reaction medium is crucial in the design of nanocrystals with desired morphology and dimension. Solution precipitation and hydrothermal method are the two common liquid phase synthesis methods. In solution synthesis, capping agents play a vital role in the nucleation and in promoting the crystallization of nanoparticles at low temperature.

In this chapter we propose a simple wet chemical approach for the synthesis of ZnO nanostructures at comparatively low temperature. Inspired by the reactivity and charge carrier separation of polar facets in ZnO, cone shaped nanostructures are synthesized by solution precipitation and hydrothermal method. The effect of synthesis conditions on the growth of ZnO nanocones is discussed in detail. The capping agent PVP has a essential role in the crystallization of ZnO by its excellent adsorption ability.

3.2. Experimental

3.2.1. Synthesis of ZnO by solution precipitation

ZnO is synthesized by simple wet chemical approach using PVP as the capping agent. Zinc acetate dihydrate is stirred with 0.05 % PVP solution (in 1% acetic acid) for 24 h to form Zinc acetate-PVP complex. The pH of this solution is

found to be 4 and ZnO is precipitated from this complex using NaOH solution. The molar ratio of zinc acetate and NaOH solution is 1:6. When NaOH solution is added in dropwise, pH of the solution slowly increases and turbidity starts to appear at a pH value of 6.4. The addition of NaOH is continued till the pH of the final solution is raised to 11. The reaction mixture is stirred for 12 h at 30-35 ^{o}C. The precipitate is filtered and dried at 100 ^{o}C and the as-obtained powder is designated as s-ZnO.

3.2.2. Effect of synthesis conditions on the growth of s-ZnO

The influence of reaction conditions on the growth of ZnO are studied in detail. The capping agent, PVP has a critical role in the nucleation of ZnO at room temperature and it is confirmed by the control experiment without capping agent. To study the effect of pH and concentration of OH^- ions on the growth of ZnO at low temperature, the synthesis is repeated by varying the pH of the precipitating solution. The s-ZnO nanopowder is calcined at 550 ^{o}C and 900 ^{o}C, for studying the effect of calcination temperature on the morphology.

3.2.3. Synthesis of ZnO by hydrothermal method

For the hydrothermal method, ZnO is precipitated using NaOH from zinc acetate-PVP complex. The colloid formed is stirred for 30 min and it is transferred to a 50 ml Teflon-lined stainless steel autoclave. It is then heated in an oven for 7 h at 100 ^{o}C. After cooling to room temperature, the product is collected by centrifugation, washed with distilled water, and dried at 100 ^{o}C. The as-obtained powder is designated as h-ZnO.

3.3. Results and Discussions

3.3.1. Room temperature solution precipitation of s-ZnO

The transmission electron micrograph of s-ZnO shown in Fig. 3.1a is dominated by cone shaped nanostructure having rough surface with an average

size of 90 nm (base) x 170 nm (height). Fig. 3.1 b shows the high resolution transmission electron microscope image of as-formed ZnO. The fringe spacing of 0.28 nm agrees well with the spacing of (100) lattice planes of ZnO. The XRD pattern (Fig. 3.2) confirms the formation of ZnO. The peaks at $2\theta = 31.7^{o}$, 34.4^{o}, 36.2^{o}, 47.5^{o}, 56.5^{o}, 62.8^{o}, 66.3^{o}, 68.0^{o} and 69.1^{o}, corresponds to the hexagonal wurtzite phase of ZnO. The nanocrystallites are oriented along (101) plane unlike along the commonly dominant (002) plane with lowest surface energy. The sharp peaks indicate that the product formed is well crystallized and oriented, further confirming the room temperature crystallization of ZnO by this method. The crystallite size evaluated by Scherer formula is found to be 24 nm. This reveals that cone shaped nanostructures are polycrystalline.

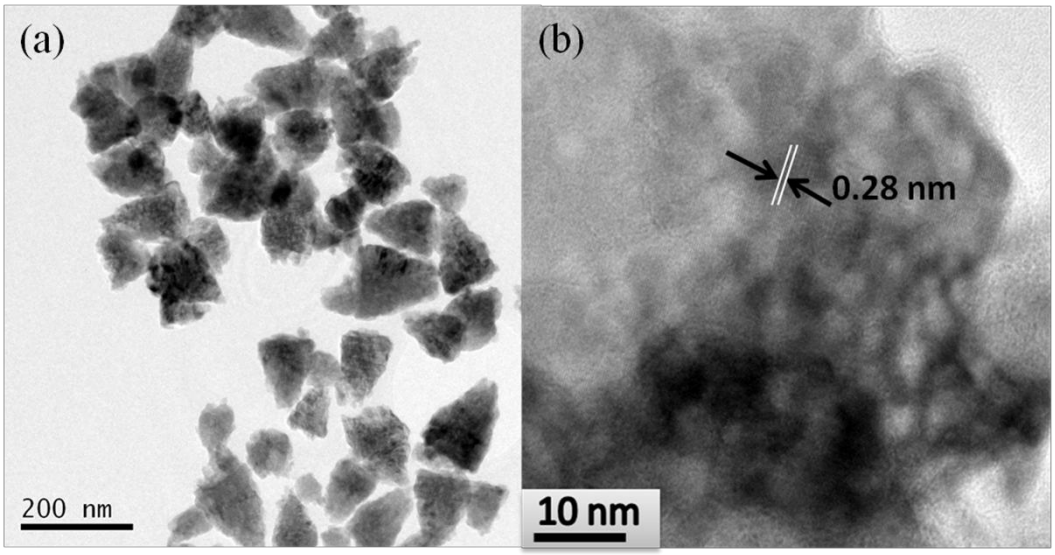

Figure 3.1. (a) TEM micrograph and (b) HRTEM micrograph of s-ZnO

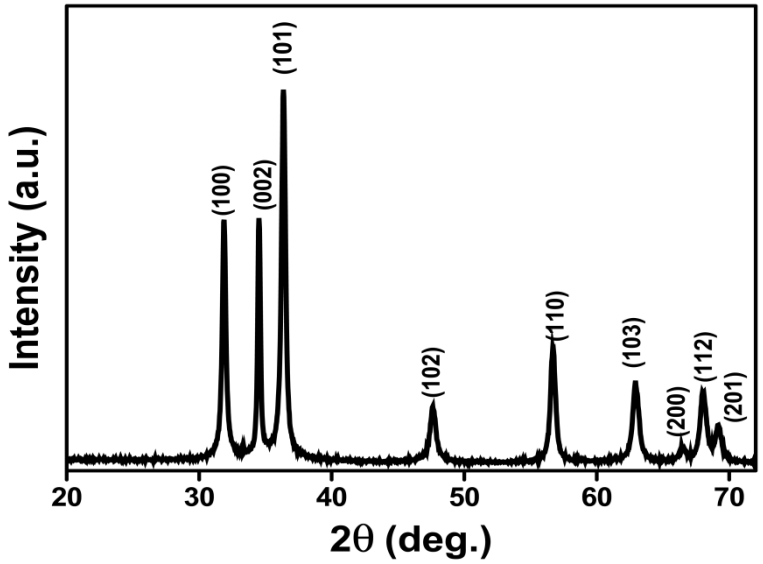

Figure 3.2. XRD pattern of s-ZnO

3.3.2. Effect of synthesis conditions on the growth of s-ZnO

To evaluate growth mechanism of ZnO nanocones, the various parameters involved in its crystallization in solution are evaluated systematically. During the solution growth of ZnO by precipitation using NaOH, zinc cations readily react with hydroxide anions to form a stable tetrahedral $[Zn(OH)_4]^{2-}$ complex, which act as the growth units of ZnO structures. The key parameters involved in the transformation of zinc hydroxide tetrahedral complex to ZnO nanocrystals are listed below.

3.3.2.1. Role of capping agent

To identify the role of capping agent in the crystallization of ZnO in solution, the precipitation reaction is repeated without using PVP, while keeping all other reaction conditions same as s-ZnO. The XRD pattern of as-synthesized ZnO is shown in Fig. 3.3 and the product contains both ZnO phase and zinc hydroxide phase. The marked peaks correspond to ZnO and all other peaks correspond to Zinc hydroxide. This confirms that in the absence of PVP all hydroxide phase cannot transform to ZnO. Zhang, J. et al. (2007, 2008) studied the effect of PVP on the nucleation of ZnO. According to their studies, PVP can

influence the ZnO growth in two ways. Firstly, it may accelerate the dehydration reaction of zinc hydroxide by consuming the resultant water via binding water due to the excellent adsorption ability of PVP. Thus it promotes the ZnO nucleation even at low temperature. Secondly the possible coordination between PVP and Zn^{2+} ions may initiate the ZnO growth. This coordination of as-formed ZnO with PVP may suppress the further aggregation of nanostructures.

TGA curve of s-ZnO with and without PVP is shown in Fig. 3.4. For s-ZnO with PVP, a weight loss of about 2.5 % is observed in the temperature range 130 ^{o}C to 540 ^{o}C, which is due to the decomposition of chemisorbed PVP on the surface of ZnO. No further weight loss and no thermal effect is observed after 540 ^{o}C, indicating the presence of pure ZnO phase. But in the TGA curve of s-ZnO without PVP, there is small weight loss of about 1.8 % due to desorption of physisorbed water molecules from 110 ^{o}C to 130 ^{o}C. After that a significant weight loss of about 13% is observed in the temperature range 130 ^{o}C to 300 ^{o}C, due to the condensation dehydration of surface hydroxyl groups (Morishige, et al., 1980). Thus TGA confirms the role of PVP in the transformation of zinc hydroxide phase to zinc oxide.

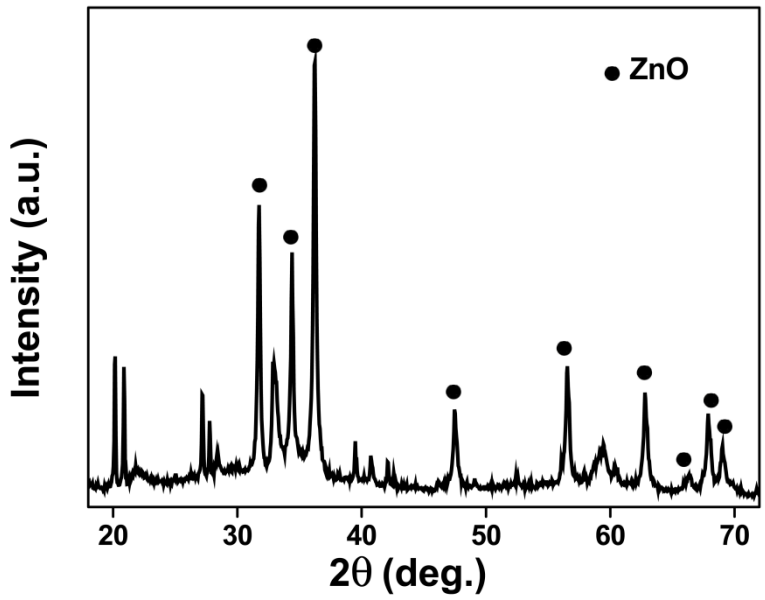

Figure 3.3. XRD pattern of s-ZnO synthesized without using PVP

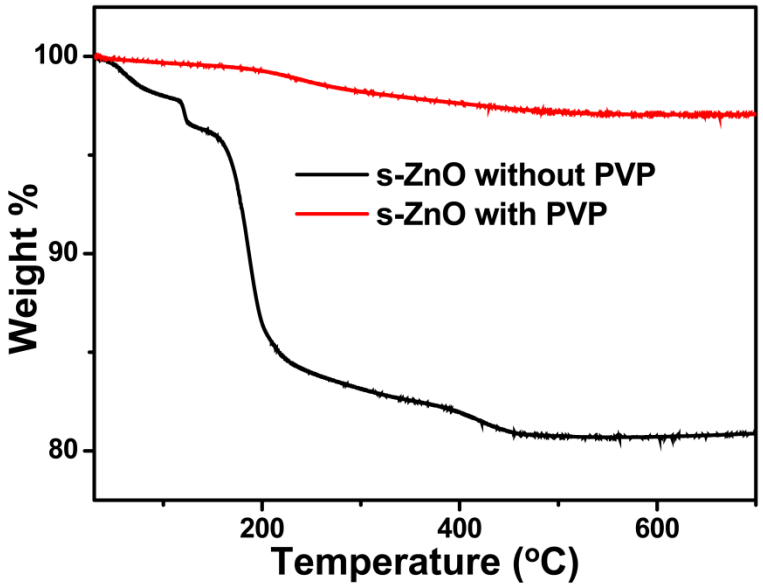

Figure 3.4. TGA curve of s-ZnO synthesized with and without PVP

3.3.2.2. Effect of pH of the reaction medium

In order to study the effect of pH of the reaction medium on the growth of ZnO, the reaction for s-ZnO is repeated and extracted the product at different pH. The XRD pattern of s-ZnO at different pH is shown in Fig. 3.5 and the marked peaks correspond to zinc hydroxide phase. The XRD analysis shows that in all the samples below pH 11, zinc hyroxide phase is present. This shows that at lower pH, complete conversion of zinc hydroxide to ZnO does not occur, because at lower pH, concentration of OH^- is not sufficient for the formation of $[Zn(OH)_4]^{2-}$, which is the nucleation center for the formation of ZnO. Fig. 3.6 a and b shows the TEM image of s-ZnO synthesized at pH 9, which shows the presence of needle shaped ZnO structures, along with small spherical paricles and hexagonal plates. During the addition of NaOH to Zn^{2+}/acetic acid solution, the turbidity appears at pH 6.4. This turbid solution contains spherical molecules of zinc hydroxide ($Zn(OH)_2$) and $[Zn(OH)_4]^{2-}$ units. At lower pH, ZnO may be formed as distorted hexagonal plates (inset of Fig. 3.6 b), because in acidic medium the H^+ ions will react with OH^- ions on the surface of this plates and inhibits the growth along c-axis. The increase of pH causes a favorable

condition for the stacking of this hexagonal plates, resulting in desired morphology, by elongation along the c-axis. At pH 9, needle shaped structures (elongated cones, Fig. 3.6 a) are present. In order to get shorter nanocones (length to width ratio decreases), the pH of the solution has to be adjusted to 11 and allowed the ZnO to grow slowly by stirring.

When higher concentration of NaOH is used, ZnO nuclei formed will undergo rapid growth and agglomeration by the absorption of excess hydroxyl ions on the polar surface may occur. Fig. 3.7 shows the TEM image of s-ZnO synthesized in highly alkaline solution. The morphology is modified to quasi-spherical nanostructures because at higher OH^- concentration, uncontrolled hydrolysis and condensation occurs with no preferential growth along the c-axis. Wang et al. (1997) have also demonstrated a similar observation such that at weak alkaline conditions elongated cones will predominate, while increasing the basicity, the cones get shortened and finally at higher alkaline condition transform into spherical shape.

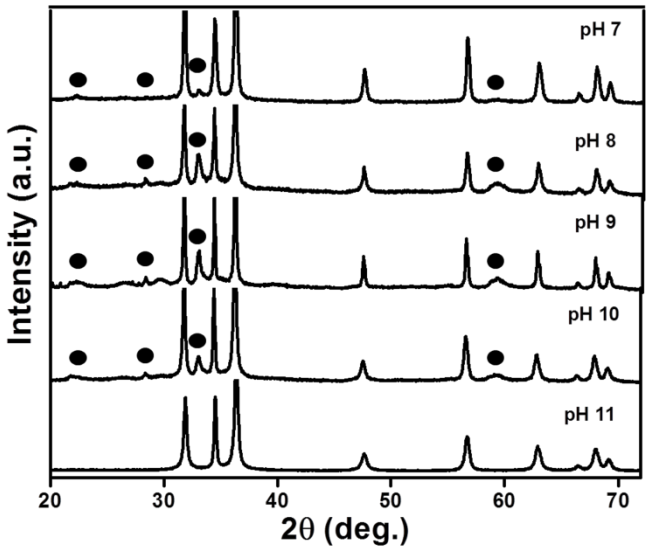

Figure 3.5. XRD pattern of s-ZnO synthesized at different pH

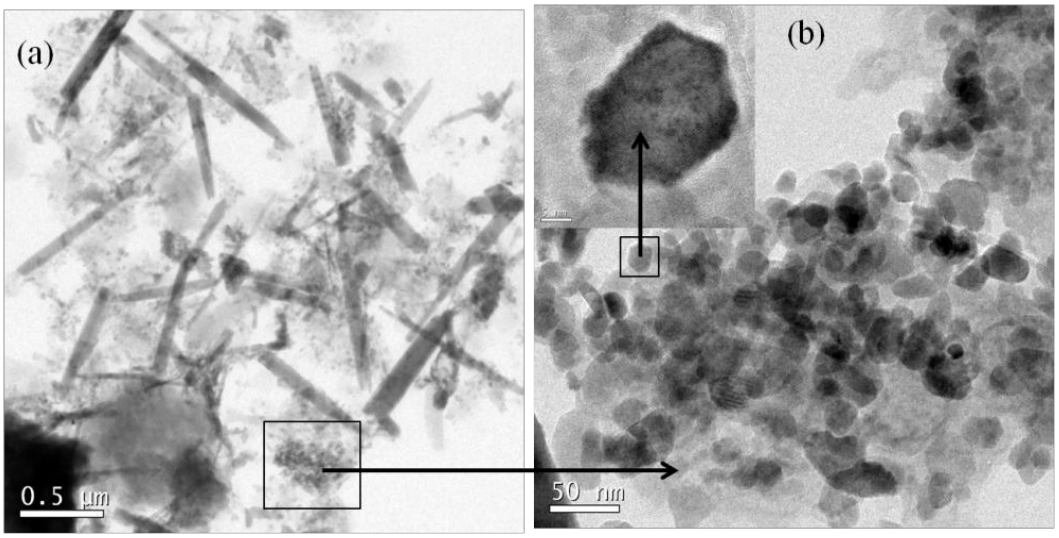

Figure 3.6. (a) TEM image of s-ZnO synthesized at pH 9 (b) Enlarged area containing spherical and hexagonal particles (inset shows the hexagonal plate)

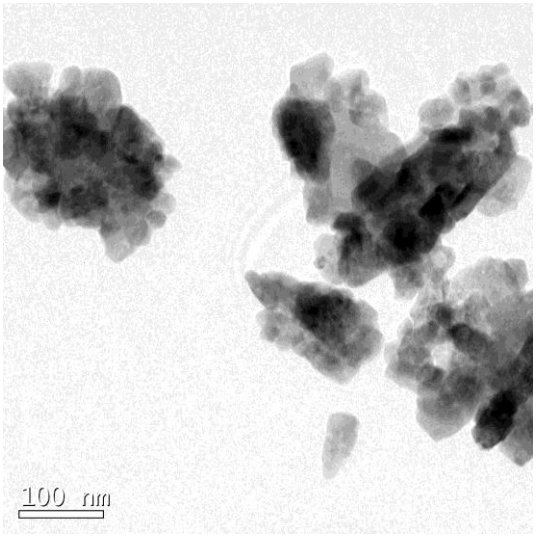

Figure 3.7. TEM image of s-ZnO synthesized at highly alkaline condition

3.3.2.3. Effect of calcination temperature

For ZnO nanocones, the high energy $(10\bar{1}1)$ facets are exposed instead of more stable $(10\bar{1}0)$ plane. Since the surface energy of $(10\bar{1}1)$ facet is higher and if it is more exposed, the crystal termination on that facet is favoured by the absorption of capping agent (Chang and Waclawik, 2012). Due to these chemisorption of PVP, surface of cone shaped s-ZnO become rough. The sample s-ZnO is calcined at 550 ^{o}C and 900 ^{o}C and their XRD pattern is shown in Fig 3.8.

When s-ZnO is calcined at 550^{o}C, smooth nanocones are formed as shown in Fig. 3.9a. It may be due to the complete decomposition of chemisorbed PVP. These cone shaped nanostructures have no crystallographically defined side planes, due to the creation of step edge on the $(000\bar{1})$ surface at high temperature. Joo et al. (2005) reported that, by the formation of step edges, the surface energy of the hexagonal cones can be lowered by reducing the number of dangling bonds on the side surface of the cone. The crystallite size is calculated from XRD pattern and it shows that there is no significant variation in crystallite size (24 nm), when it is calcined at 550 ^{o}C. When s-ZnO is calcined at 900 ^{o}C, large clusters of nanocones are formed (Fig. 3.9b). Due to high surface energy of the crystal planes in nanocones, they will aggregate rapidly to form clusters and the crystallite size is increased to 42 nm as compared to s-ZnO.

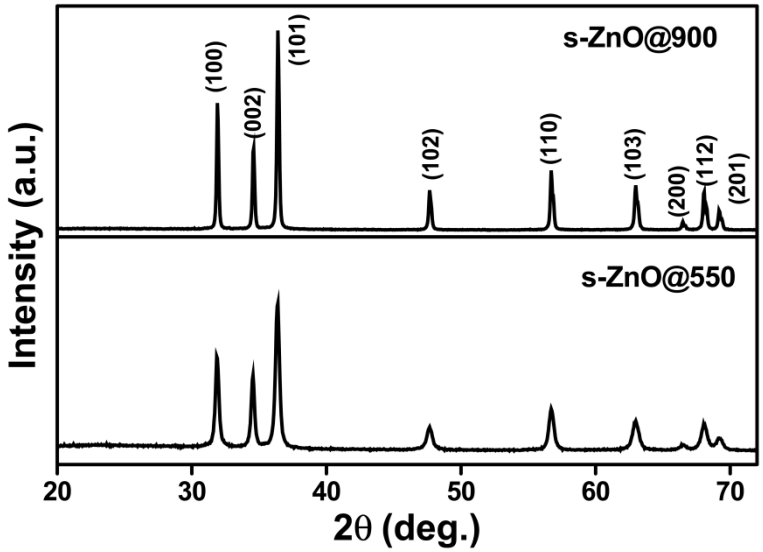

Figure 3.8. XRD pattern of s-ZnO calcined at (a) 550 ^{o}C (b) 900 ^{o}C

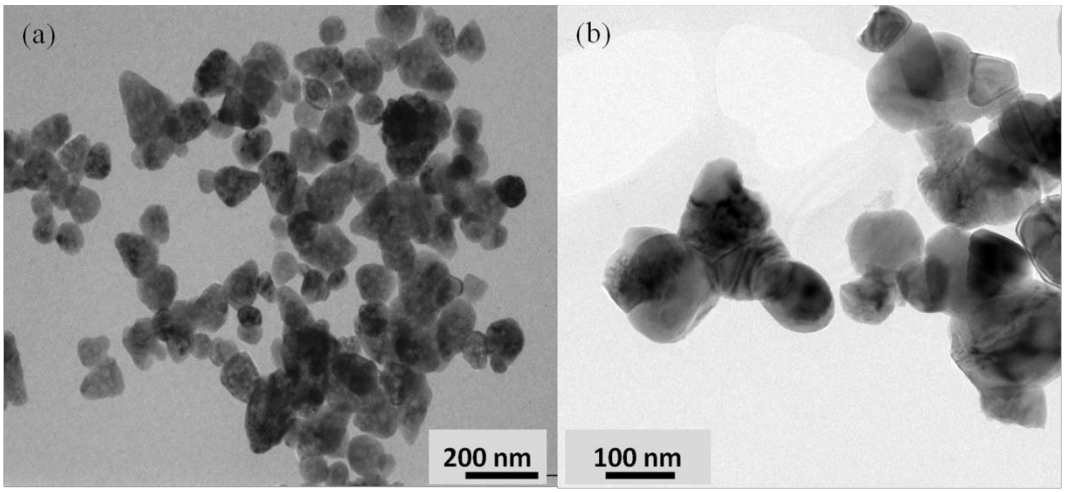

Figure 3.9. TEM micrograph of s-ZnO calcined at (a) 550 ^{o}C (b) 900 ^{o}C

3.3.3. Growth mechanism of ZnO nanocones

In this study PVP is dissolved in 1 % acetic acid solution and in this polar medium PVP is partially polarised. Since the oxygen atom is more electronegative than nitrogen, the partial negative charge resides on oxygen atom and partial positive charge on nitrogen atom. The nitrogen atom is located inside the PVP molecule and has a saturated covalent bond, while the oxygen atom is located outside the molecule, hence PVP shows more anionic properties. When the zinc salt is mixed with PVP, the Zn^{2+} cation can directly attach to the negatively charged end of PVP to form Zn^{2+}/PVP complex. On this coordinated complex, the first layer of crystal growth will be initiated (Gu, et al., 2012). When NaOH is added, OH^{-} will react with the coordination complex to form $[Zn(OH)_4]^{2-}$. Since the growth and the conversion of ZnO is reversible, with the increase in OH^{-} concentration, the equilibrium tends to proceed towards right as given in Fig 3.10.

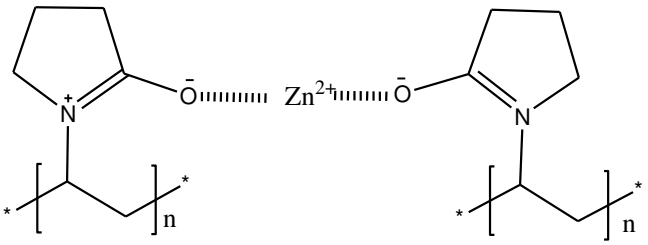

$$Zn^{2+} + 4OH^- \rightleftharpoons [Zn(OH)_4]^{2-} \rightleftharpoons ZnO + H_2O + 2OH$$

Figure 3.10. Representation of the coordination of Zn^{2+} with PVP and possible reaction to form ZnO

In a typical ZnO wurtzite structure, number of alternating planes composed of tetrahedrally coordinated O^{2-} and Zn^{2+} are stacked along the c-axis. Such a crystal structure is composed of basal polar oxygen plane $(000\bar{1})$, a top tetrahedral corner with exposed polar zinc plane (0001), and low index facets consisting of nonpolar $(10\bar{1}0)$ planes parallel to c-axis (Xu, et al., 2005). The nonpolar $(10\bar{1}0)$ facets are more stable than polar (0001) and $(000\bar{1})$ facets because of their relatively lower surface energies. But for ZnO nanocones the high energy $(10\bar{1}1)$ facets are exposed instead of more stable $(10\bar{1}0)$. The formation of hexagonal cone shape of ZnO can be attributed to the different growth rate of the various growth facets in the order (0001) > $(10\bar{1}1)$ >$(10\bar{1}0)$. It is well studied that faster the growth rate, quicker will be the disappearance of that plane (Li, et al., 1999). Therefore, the (0001) plane tends to disappear in the growth process and result in tip shaped nanostructures (Gu, et al., 2012).

Figure 3.11 presents the morphology of ZnO nanostructures at different pH. By the analysis of ZnO nanostructures at different pH, the driving force behind the growth of nanocones is described (Kavitha et al., 2014b). When Zn^{2+} and OH^- is mixed in acetic acid solution, intially zinc hydroxide will form and get dissolved. When the pH of the solution is slowly increased, the turbidity apppears due to the formation of spherical aggregates of $[Zn(OH)_4]^{2-}$ units. When the pH raised to 6.4, ZnO will precipitate as hexagonal plates and its growth along c-axis is restricted by H^+ ions adsorbed on its surface. When the pH of the solution is further increased, growth become favourable between the plates by its stacking in

both polar diections, elongated cones. When the concentration of OH^- is further increased around 11, large quantity of OH^- is adsorberd on polar (0001) facet, restricting the growth along c- axis, resulting in shortened nanocones. Finally when the concentration of OH^- is very high (pH > 11), it gets adsorbed in all the polar surface, no preferential growth along the c-axis and hense quasi spherical particles are formed. Thus in shortened nanocones, the exposed planes are polar and oxygen terminated namely base plane $(000\bar{1})$ and six side planes $(10\bar{1}1)$ (Dakhlaoui, et al., 2009). Since the surface energy of $(10\bar{1}1)$ facet is higher and it is more exposed, the crystal termination on that facet may also be favoured by the adsorption of capping agent (Chang and Waclawik, 2012). Due to these chemisorptions of PVP, surface of conical structures become rough.

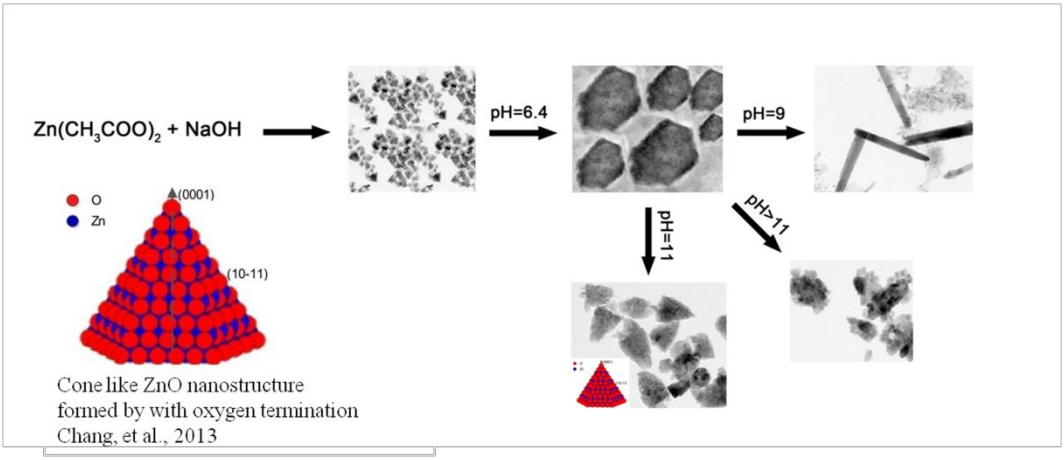

Figure 3.11. Schematic representation of the morphology of ZnO nanostructures at different pH

In ZnO nanocones, since the exposed planes are oxygen terminated, the prominent defects during the growth process is predicted to be that of oxygen vacancies. These defect states play an important role in the below bandgap photoresponse of ZnO, and it can be utilised for tailoring the optoelectronic and photonic properties of ZnO. When ZnO is calcined at 550 ^oC, the surface becomes smoothened due to the removal of capping agent and a drastic surface reconstruction occurs to form spherical crystallites, by curving of side planes to minimize the surface energy (Fig. 3.9 a). These cone-shaped nanostructures do not have crystallographically well-defined side planes, due to the creation of step edge on the $(000\bar{1})$ surface at high temperature.

3.3.4. Hydrothermal synthesis of ZnO (h-ZnO)

Using the optimized reaction conditions for s-ZnO, ZnO colloid is prepared and heated hydrothermally at different temperatures namely 60 ^{o}C, 80 ^{o}C, 100 ^{o}C and 150 ^{o}C and its TGA is shown in Fig. 3.12. ZnO prepared at 60 ^{o}C, shows a weight loss of around 8 % in the temperature range of 130 ^{o}C to 400 ^{o}C, due to the dehydration of surface hydroxyl groups. All other samples shows a weight loss below 2 % in this temperature range due to the decomposition of PVP alone. Therefore, it is clear that at 80 ^{o}C and above, pure ZnO is formed. Hydrothermal method has the advantage over solution precipitation due to its better control over the particle size and the temperature assisted fast conversion of zinc hydroxide to ZnO. Fig. 3.13 shows the XRD and TEM image of h-ZnO at 100 ^{o}C. The crystallite size is about 23 nm, same as that of s-ZnO. h-ZnO is also cone shaped structure but with low length to width ratio (100 nm × 50 nm), compared to s-ZnO. Since the aspect ratio is reduced, the oxygen terminated polar facets ($10\bar{1}1$) become more exposed in h-ZnO, which may favour the creation of more centers of oxygen vacancies.

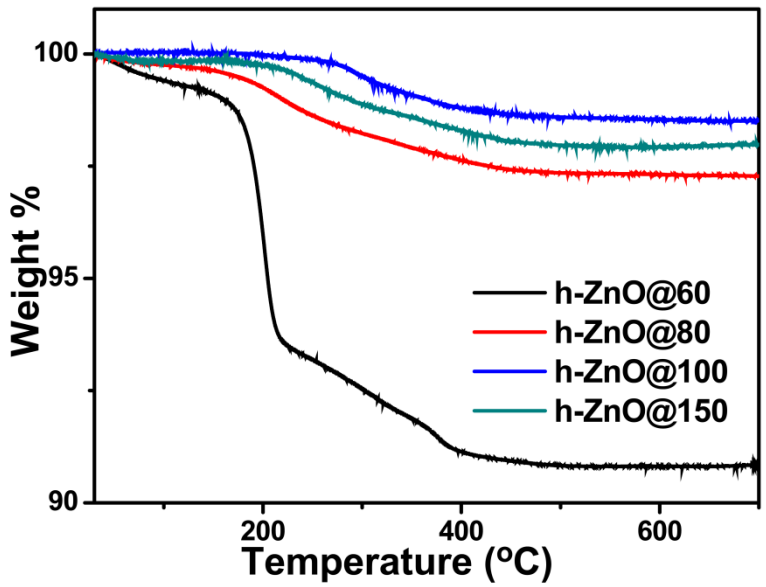

Figure 3.12. Thermogram of h-ZnO synthesized at different temperature

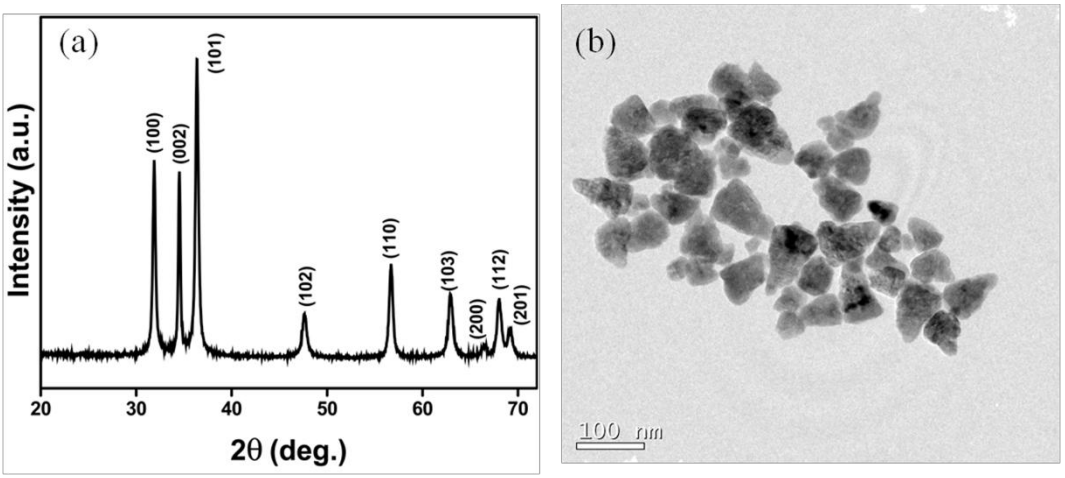

Figure 3.13. (a) XRD pattern and (b) TEM image of h-ZnO at 100^{o}C

The defect states in ZnO will affect its optical properties and it is discussed in chapter 4 in detail.

3.4. Conclusions

ZnO nanocones are synthesized by simple solution precipitation and hydrothermal method using PVP as the capping agent. In this method PVP has a significant role in nucleation and growth of ZnO at comparatively low growth temperature. The growth mechanism is proposed on the basis of ZnO growth habit with respect to the concentration of OH^- ions in the solution. At lower pH elongated cones are formed by the fast growth rate along the c-axis. When the concentration of OH^- is further increased, length to width ratio of the nanocones is reduced due to the impeded growth along c-axis by the adsorption of OH^- ions on the polar (0001) facets. When the ZnO is synthesized under hydrothermal condition, the cones again get shortened. The cone shaped morphology has polar oxygen terminated facets exposed; which can facilitate oxygen vacancy centres in the surface. These defect states can modify the optical properties of ZnO.

CHAPTER 4
ROLE OF DEFECTS IN ZnO NANOCONES FOR VISIBLE LIGHT PHOTOCONDUCTIVITY AND NONLINEAR ABSORPTION

Photoluminescence spectra of ZnO nanocones demonstrate that the as-grown samples have both oxygen and zinc vacancies, and after calcination oxygen vacancies vanish, but zinc vacancies enhance. Photoconductivity of the samples reduces significantly upon calcination, due to the reduction in oxygen vacancies. However, the samples exhibit a significant enhancement in the effective two-photon absorption upon calcination, indicating that nonlinear optical absorption originates from zinc vacancies.

4.1. Introduction

ZnO is a promising optoelectronic material owing to its wide direct bandgap and large exciton binding energy at room temperature. ZnO defects chemistry has been studied for the past few decades to employ this material for various optical and electronic applications (Ischenko, et al., 2005; van Dijken, et al., 2000a; Zeng, et al., 2010). For instance, the response of ZnO can be tuned within the visible spectral region by controlling the intrinsic defect levels, which makes it an excellent photodetector in the visible spectral regime. These intrinsic defect levels create localized states within the bandgap, which influences the optical absorption and the carrier dynamics (Sheetz, et al., 2009). However, the nature and origin of the defects prevalent in native undoped ZnO is still a matter of controversy. Density functional theory (DFT) calculations show that the band structure of ZnO is determined by O 2p and Zn 3d orbitals, and the upper levels of the valence band are constituted by O 2p levels (Lv, et al., 2013; Sheetz, et al., 2009). The defect levels in ZnO are usually categorized into four types, namely, oxygen vacancies (V_O) and zinc vacancies (V_{Zn}) which are generally surface defects, interstitials (Zn and O) and antisites which exist in the bulk of the

material (Schmidt-Mende and MacManus-Driscoll, 2007). Majority of the defect levels belong to oxygen and zinc vacancies. The nature of defects in ZnO depends on factors like exposed facets in different morphology, doping, etc. ZnO normally crystallizes in the wurtzite structure, but the exposed facets are different with different morphologies. For example, the nonpolar facets $(10\bar{1}0)$ are more exposed in ZnO nanorods, while the polar oxygen terminated $(10\bar{1}1)$ facets are dominant in nanocones (Chang, et al., 2013).

In this chapter, the optical properties of as-prepared ZnO nanocones is analysed and compared them with ZnO calcined at 550 ^{o}C, in order to understand the nature of defect levels present. The effect of defects on the visible light photocurrent generation and nonlinear optical properties are also explored. ZnO samples for these studies are prepared by the procedure as described in chapter 3, Section 3.2. The samples synthesized by hydrothermal and solution processes are designated as h-ZnO and s-ZnO, and their calcined samples as h-ZnO@550 and s-ZnO@550, respectively.

4.2. Experimental

4.2.1. Measurement of optical properties of ZnO

The UV-vis absorption spectra of ZnO are recorded on a Varian Cary Bio 100 UV Spectrophotometer at room temperature in the wavelength ranging from 210 nm to 600 nm. The room temperature photoluminescence spectra are recorded using Horiba Jobin Yvon spectrofluorometer at an excitation wavelength of 340 nm. The decay transient is measured using the time correlated single photon counting (TCSPC) technique. The samples are excited using 340 nm laser source (pulse duration < 1 ns) and the emission lifetime is measured using the Horiba Jobin Yvon single photon counting system. For all the measurements, the concentration of ZnO samples is taken as 1 mg in 10 ml in water.

4.2.2. Fabrication of ZnO films for photocurrent measurements

Films of ZnO for photocurrent measurement are fabricated on clean FTO glasses. The FTO glasses are cleaned by ultrasonication in distilled water, isopropyl alcohol and acetone. The ZnO (5 mg) dispersion is made in aqueous solution of 4 % polyacrylamide (PAM). Nine layers are coated on FTO substrate (2 cm^2) by successive spin coating of 300 µl of the dispersion. For each layer the dispersion is spun at 500 rpm for 120 s followed by 3000 rpm for 30 s. After spin coating, the films are dried under vacuum for 12 h.

4.3. Results and Discussions

4.3.1. UV-vis absorption and photoluminescence spectra of ZnO

The UV-vis absorption spectrum of the as-prepared and calcined ZnO samples is shown in Fig. 4.1. A clear blue-shift in the excitonic absorption edge is observed in the spectra of all ZnO samples, compared to the bulk ZnO. h-ZnO and s-ZnO shows more blue shift in the absorption edge (362 nm) compared to the corresponding calcined samples (372 nm). The shift in the absorption edge to higher wavelength after calcination indicates a smaller bandgap for calcined ZnO. This red shift in the band edge absorption wavelength of ZnO nanopowders calcined at high temperature is due to the formation of shallow levels inside the bandgap as a result of the impurity atoms in the lattice or strong disturbances of local symmetry in the ZnO lattice (Pradhan, et al., 2011).

The inset of Fig. 4.1 shows the estimation of its optical bandgap using the Tauc equation (Tauc, 1966). The bandgap calculated for as-synthesized samples is 3.27 eV (h-ZnO) and 3.23 eV (s-ZnO), which is slightly lower than the bandgap of bulk ZnO (3.37 eV), which may be due to the existence of valence band-donor level overlap due to the surface states (Srikant and Clarke, 1998). The bandgap of calcined samples is found to be reduced further to 3.16 eV. This reduction may be due to the introduction of defect levels within the bandgap

(Pradhan, et al., 2011) and the nature of these defect levels can be identified from photoluminescence spectra.

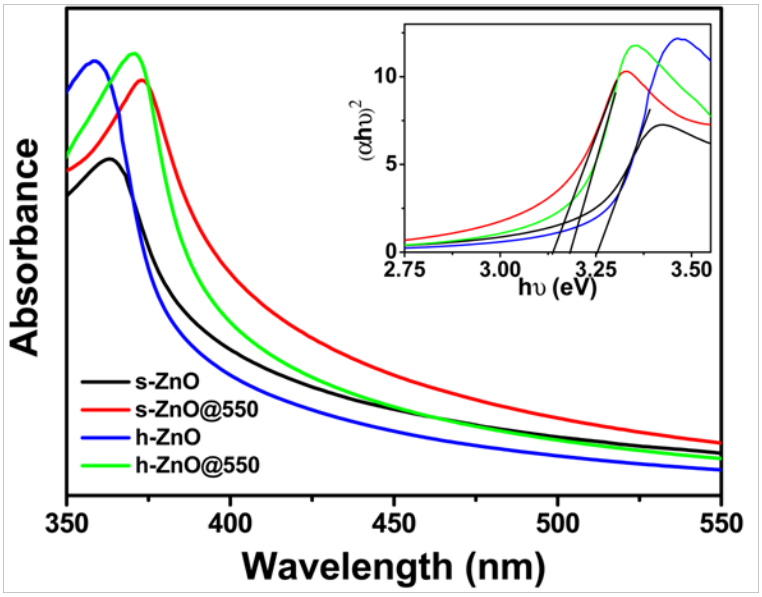

Figure 4.1. UV-vis absorption spectra of the ZnO samples. Inset shows the Tauc plots for bandgap calculation

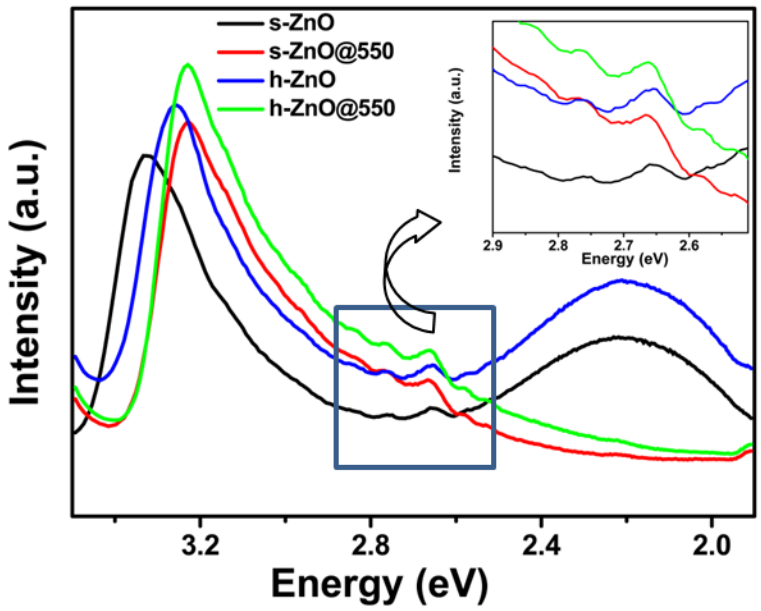

Figure 4.2. Photoluminescence spectra of h-ZnO, s-ZnO and the samples calcined at 550 °C. Inset highlights the emission at 2.69 eV by the zinc vacancies. The excitation wavelength is 340 nm.

Fig. 4.2 shows the room temperature photoluminescence spectra of h-ZnO, s-ZnO, h-ZnO@550 and s-ZnO@550. In all the samples there is a sharp emission in the ultraviolet region due to the band-to-band radiative recombination of excitons, and a broad green emission centred at 2.25 eV, together with a minor blue emission peak at 2.69 eV. The green emission at 2.25 eV can be linked to the native point defects in the ZnO lattice (Appavoo, et al., 2014). When the samples are calcined at 550 ^{o}C, the green emission around 2.25 eV is substantially quenched while the blue emission around 2.69 eV is improved.

The defects responsible for visible emission in undoped ZnO are proposed to be the native defects such as the oxygen vacancy (van Dijken, et al., 2000b) (V_O), zinc vacancy (Li, et al., 2013) (V_{Zn}), Zn interstitial (Zn_i) (Knutsen, et al., 2012), and oxygen intersitial (O_i). Theoretical calculations predict that these defects will create deep energy levels in the bandgap; V_O and Zn_i generate mainly donor levels (Erhart, et al., 2006), whereas V_{Zn} produces acceptor levels. Defect levels related to oxygen interstitials (O_i) occur both near the valence band maximum and the conduction band minimum. Among the donor type defects V_O has the least formation energy, but in the case of acceptor type defects, V_{Zn} has the lowest formation energy (Janotti and van de Walle, 2007). In zinc rich conditions oxygen vacancies are more favourable to form, and therefore, during the precipitation of ZnO in solution, oxygen vacancies are more probable to form in the crystal lattice. Fig. 4.2 indicates that for both s-ZnO and h-ZnO, there is a prominent green emission around 550 nm (2.25 eV), and it is suppressed upon calcination in air. The origin of green emission is highly debated, since calcination in air would heal oxygen vacancies rather than zinc vacancies, the green emission centred at 2.25 eV should be due to the oxygen vacancies. This conclusion has been supported by first principle investigations of the nature of defects in ZnO (Janotti and van de Walle, 2007). The broad green emission in ZnO originates from two sources: the low energy green emission centred at 2.25 eV (van Dijken, et al., 2000b) occurs from surface defect states while the high energy green emission at 2.5 eV occurs from defects in the bulk (Vanheusden, et al., 1996a).

Generally, oxygen vacancies create donor-like levels in the bandgap, corresponding to a defect level 0.5 eV by the singly ionised oxygen vacancies ($V_O^{\cdot}$) and 2 eV by the doubly ionised oxygen vacancies ($V_O^{\cdot\cdot}$) below the conduction band (van Dijken, et al., 2000a). The low energy green emission is due to the capture of holes by $V_O^{\cdot}$ to generate $V_O^{\cdot\cdot}$, leading to an emission with a peak at 2.25 eV (van Dijken, et al., 2000b). The high energy green emission occurs when the singly ionised oxygen vacancy ($V_O^{\cdot}$) becomes neutral V_O^{x} by capturing an electron from the conduction band giving out the emission at 2.5 eV (Vanheusden, et al., 1996b). The green emission centred at 2.25 eV is prominent for as-obtained ZnO (h-ZnO and s-ZnO), and when it is calcined the relative contribution of low energy green emission is decreased (Abhinandan, et al., 2010). This suggests that the doubly ionised surface oxygen defect states ($V_O^{\cdot\cdot}$) are mainly responsible for green emission in h-ZnO and s-ZnO and these surface oxygen vacancies can get compensated upon calcination in air. In h-ZnO and s-ZnO, a weak blue emission at 2.69 eV is observed, which is enhanced after calcination (as shown in the inset of Fig. 4.2). It is known that in oxygen rich conditions V_{Zn} and O_i are the dominant defects in ZnO (Erhart, et al., 2006; Janotti and van de Walle, 2007). First principle calculations show that Zn vacancy creates two energy levels: the first one by the transition between 0 and -1 charge states of Zn vacancies, introducing defect level around 0.8 eV above the valence band, and the second by -1/-2 level at the middle of the bandgap (Erhart, et al., 2006), around 2.3 eV above the valence band (Chen, S. L., et al., 2012). Therefore the observed emission peak at 2.69 eV can be attributed to the transition between the conduction band and the V_{Zn} acceptor level.

Considering the visible emission of h-ZnO and s-ZnO, both samples show a broad visible emission indicating the presence of deep trap levels. Comparing the intensity and position of blue emission and green emission, the defect states should be due to the presence of the dominant V_O states rather than V_{Zn}. The ratio of the intensity of green emission and UV emission (I_{GE}/I_{UV}) is an important factor for determining the concentration of defects related to the synthesis conditions (Foreman, et al., 2006). I_{GE}/I_{UV} value of h-ZnO and s-ZnO

are 0.55 and 0.45 respectively, indicating that hydrothermally grown ZnO has more oxygen vacancies. When h-ZnO and s-ZnO are calcined, the green emission corresponding to V_O is completely quenched, while the blue emission corresponding to V_{Zn} at 2.69 eV appears slightly enhanced.

4.3.2. Lifetime measurement and decay transient

Using the time correlated single photon counting technique, the dynamics and relaxation kinetics of photogenerated charge carriers in ZnO leading to defect emission is studied. The samples are excited using 340 nm laser source and the emission lifetime is measured. The temporal decay of emission at 2.25 eV (550 nm) and 2.69 eV (460 nm) is monitored, and the obtained decay kinetics is shown in Fig. 4.3.

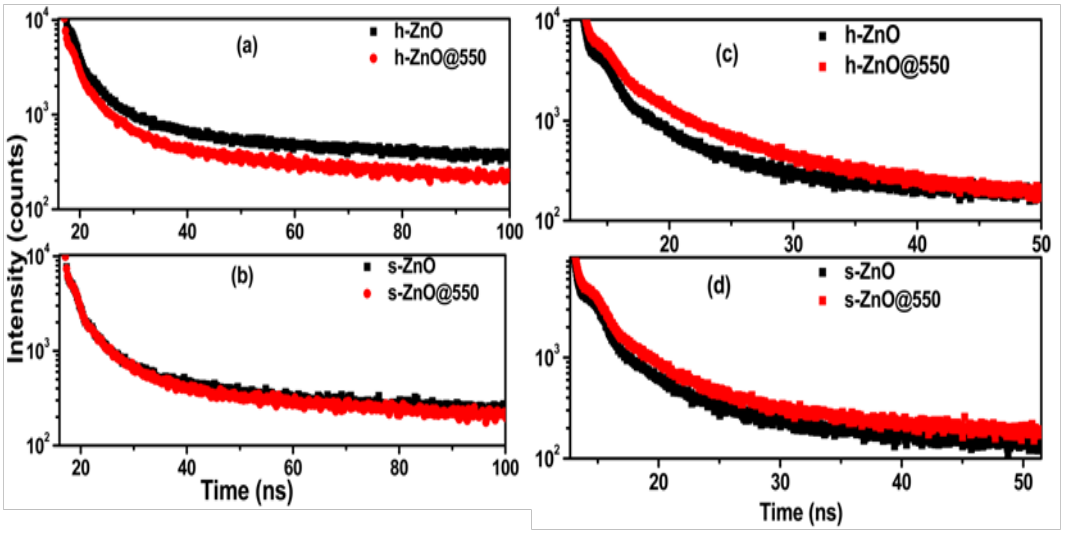

Figure 4.3. Fluorescence decay curves measured by TCSPC for h-ZnO, h-ZnO@550, s-ZnO and s-ZnO@550. The excitation wavelength is 340 nm. Emission is monitored at 550 nm (a,b) and 460 nm (c,d) respectively

The experimental values are fitted with a biexpontential model given by

$$f(t) = A_1 e^{\frac{t}{\tau_1}} + A_2 e^{\frac{t}{\tau_2}} \tag{4.1}$$

where τ_1 and τ_2 are the lifetimes, and A_1 and A_2 are pre-exponential factors. The average lifetime $\langle \tau \rangle$ can be determined using the Eq. 4.2. The fitting parameters are given in Tables 4.1 and 4.2.

$$\langle \tau \rangle = \sum_{i=1}^{n} \frac{A_i \tau_i^2}{A_i \tau_i} \tag{4.2}$$

The decay of visible emission comprises of two components, namely, a fast component (τ_1) and a slow component (τ_2), knowing which the average lifetimes of the samples can be calculated. While comparing the average decay lifetime of h-ZnO and s-ZnO at 550 nm (Table 4.1), it is seen that hydrothermally grown samples have longer lifetimes indicating the presence of a larger density of states in the inter-bands, which can trap the charge carriers. However, upon calcination of h-ZnO and s-ZnO, there is a two-fold decrease in the average lifetime, indicating the reduction of defect levels. The origin of two decay components for the PL transient is from the combination of radiative and nonradiative (NR) recombination processes (Lee, et al., 2010) as $(1/\tau_r + 1/\tau_{nr})^{-1}$, where τ_r and τ_{nr} denote the intrinsic radiative and defect-mediated NR lifetimes. For h-ZnO and s-ZnO the contribution from τ_2 is dominant, while the fast component is prominent for the corresponding calcined samples. When the ZnO nanocones are calcined in air, oxygen vacancies are healed out, and the fast nonradiative components become prominent for the emission characteristics. Thus, it is evident that in as-synthesized samples, the deep level states generated by the surface oxygen vacancies are mainly responsible for the radiative carrier relaxation giving out the green emission (van Dijken, et al., 2000b). This is evident from the PL spectra of the samples calcined in air, where the green emission is completely quenched. Consequently, the carrier lifetime is improved after calcination in the oxygen rich condition. On the contrary, the carrier lifetime probed at the 460 nm emission appears to increase after calcination. Since this is a

signature emission peak of the zinc vacancies (V_{Zn}) the enhanced lifetime at 460 nm is an indication of increasing zinc vacancy, most probably at the surface of the nanoparticles (Table 4.2).

Table 4.1. Lifetime analysis of ZnO emission at 550 nm

Sample	χ^2	A_1	τ_1(ns)	A_2	τ_2 (ns)	$<\tau>$
h-ZnO	1.16	0.47	6.39	0.53	98.9	93.88
s –ZnO	1.31	0.49	5.71	0.51	81.7	76.98
h-ZnO@550	1.42	0.52	5.19	0.48	51.91	47.30
s-ZnO@550	1.13	0.55	4.5	0.45	40.46	36.20

Table 4.2. Lifetime analysis of ZnO emission at 460 nm

Sample	χ^2	A_1	τ_1(ns)	A_2	τ_2 (ns)	$<\tau>$
h-ZnO	1.14	0.53	3.12	0.47	15.68	13.34
s-ZnO	0.94	0.61	3.31	0.39	18.88	15.53
h-ZnO@550	1.23	0.55	3.16	0.45	24.18	21.32
s-ZnO@550	1.11	0.63	3.2077	0.37	22.11	18.37

The morphology of ZnO plays a critical role in the generation of surface defect states, since different crystal orientations have different surface energies. For ZnO nanocones, the high energy polar $(10\bar{1}1)$ facets are exposed (Zhou, et al., 2005) instead of the energetically more favourable $(10\bar{1}0)$ plane. The basal plane will be polar $(000\bar{1})$ and six sides of the crystallite form the high energy polar $(10\bar{1}1)$ planes, both are oxygen terminated (Chang, et al., 2013; Ghoshal,

et al., 2008). Therefore, surface defects like V_O are predicted to be the prominent defects during the growth of ZnO nanocones (Kováčik, et al., 2007). The surface energy of polar planes can be reduced by passivating the surface by the capping agent (PVP). When ZnO is calcined at 550 ^oC, the surface is smoothened due to the removal of capping agent and a drastic surface reconstruction occurs to form spherical crystallites, by curving of side planes to minimize the surface energy. These cone-shaped nanostructures do not have crystallographically well-defined side planes due to the creation of step egde on the $(000\bar{1})$ surface at high temperature (Joo, et al., 2005), and the Zn ions may escape from the step edges during the calcination process. This accounts for the slight enhancement in the blue emission (2.69 eV) and increase in its decay transient. Thus in as-synthesized samples oxygen vacancies are prominent while in calcined samples Zn vacancies are prominent. These defect states play an important role in the below bandgap photoresponse of ZnO, and it can be utilised for tailoring the optoelectronic and photonic properties of ZnO.

4.3.3. Visible light photoconductivity in ZnO nanocones

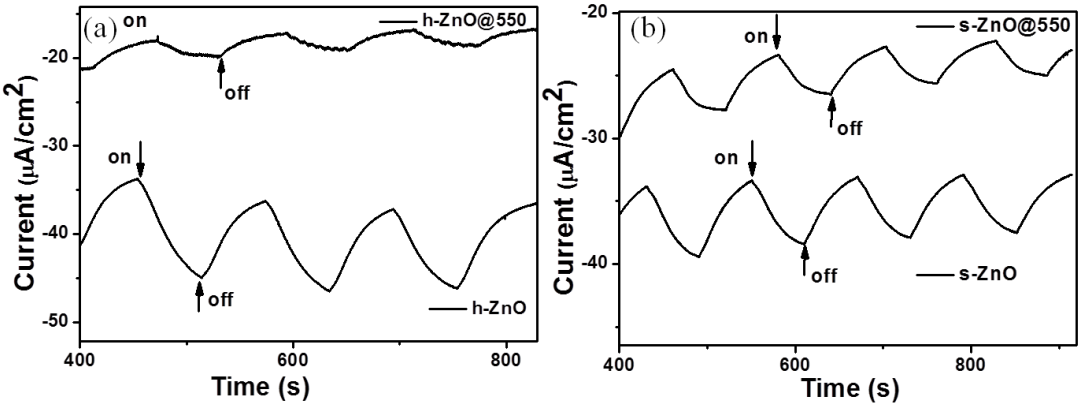

Figure 4.4. Photocurrent of various ZnO samples. (a) h-ZnO and h-ZnO@550, (b) s-ZnO and s-ZnO@550 at -0.5 V bias voltage

The role of defects in the visible light photoconductivity and nonlinear absorption of ZnO is analysed systematically. Many researchers have studied how the defects influence the optoelectronic properties of ZnO in the ultraviolet regime

(Kushwaha and Aslam, 2012; Mishra, et al., 2010; Pan, et al., 2013; Reyes, et al., 2012; Sharma, et al., 2003), but the contribution in visible light photoconductivity (Moazzami, et al., 2006) of undoped ZnO has not been well explored. Fig. 4.4 shows the photocurrent measured for various ZnO samples as a function of time at –0.5 V bias voltage with light on-and-off cycles in an interval of 60 s. The value of dark current, photocurrent and on-off difference are summarised in Table 4.3.

Table 4 3. Dark current, photocurrent and on-off difference of ZnO samples

Sample	Dark current $\mu A/cm^2$	Photocurrent $\mu A/cm^2$	On-off difference $\mu A/cm^2$
h-ZnO	-35.72	-45.72	10
s-ZnO	-33.44	-38.52	5.08
s-ZnO@550	-23.56	-26.56	3
h-ZnO@550	-16.88	-19.4	2.52

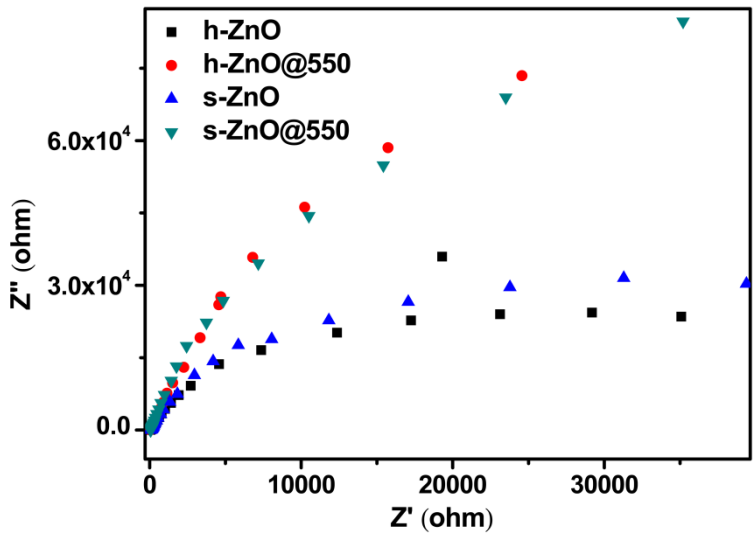

Figure 4.5. Nyquist plot of the impedance data of h-ZnO, h-ZnO@550, s-ZnO and s-ZnO@550

Hydrothermally grown ZnO exhibits the highest dark current and its conductivity is increased upon light illumination. When the samples are calcined at 550 ^{o}C, the dark conductivity as well as the photoconductivity decreased, indicating the reduction in donor level density (caused by the surface oxygen vacancies). Comparing the photoresponse of the samples with their respective PL and decay transient, the nature of the dominating defect levels can be identified. As shown in Fig 4.2, after calcination the green emission corresponding to oxygen vacancies is completely suppressed but the blue emission due to Zn vacancies persists or even enhances. Thus, the reduction in the photocurrent of the calcined sample may be due to the reduction in the oxygen vacancies. The hydrothermally synthesized samples have the higher photoconductivity as compared to s-ZnO. Comparing the photoresponse of as-synthesized and calcined samples, h-ZnO has 70 % higher photocurrent than h-ZnO@550, while s-ZnO has only 50 % more photocurrent compared to the calcined counterpart. This indicates that hydrothermally grown sample has more oxygen vacancies than all other samples. This conclusion has been verified by analyzing the impedance data of the samples. The carrier transfer resistance in ZnO samples is analysed using electrochemical impedance spectroscopy measurement. Fig 4.5 shows the Nyquist plot of the impedance data. While comparing the Nyquist plot of different ZnO samples, h-ZnO has the lower charge transfer resistance indicating the presence of larger number of carriers responsible for its enhanced photoconductivity.

In ZnO nanocones, vacancy creation on the oxygen terminated exposed facets will create structural changes on relaxation, which will significantly affect the electronic structures. Theoretical calculations (Sheetz, et al., 2009) predict that the valence band of ZnO is mainly constituted by O 2p states and deep states by partially Zn 3d states. The oxygen vacancies in the material induce localised occupied states in the bandgap (Lv, et al., 2013), creating donor levels. It is well known that the green emission in ZnO is generally due to the defect level to defect level transition generated by oxygen vacancies (van Dijken, et al., 2000a; van Dijken, et al., 2000b). Excitation with visible light can generate charge carriers, thereby increasing the charge carrier density, resulting in increasing photocurrent.

After calcination the concentration of oxygen vacancies decreases, which in turn reduces visible light absorption and photocurrent generation (Wang, J., et al., 2012). Therefore in ZnO samples, even though the Zn vacancies persist, oxygen vacancies have a critical role in visible light photoconductivity.

4.3.4. Nonlinear absorption

ZnO exhibits strong nonlinear absorption properties, which makes it a good candidate for nonlinear optical (NLO) devices such as optical limiters. Optical limiters are materials which transmit light normally at low input laser fluences, but transmit less at high inputs. The defect states in ZnO have a significant role in its nonlinear absorption (Anand, et al., 2014; Chen, S. L., et al., 2012; Stehr, et al., 2014). However, the type of defect levels that will contribute to the NLO activity of ZnO is still a matter of debate. In order to understand the effect of defect levels on the nonlinear property of ZnO, open aperture Z-scan technique is used to measure nonlinear absorption and optical limiting properties of colloidal ZnO samples. The measured open aperture Z-scan curve exhibits a decrease in transmittance at high intensities as shown in Fig 4.6a**.** Fig 4.6b shows the optical limiting curve calculated from the Z-scan curve.

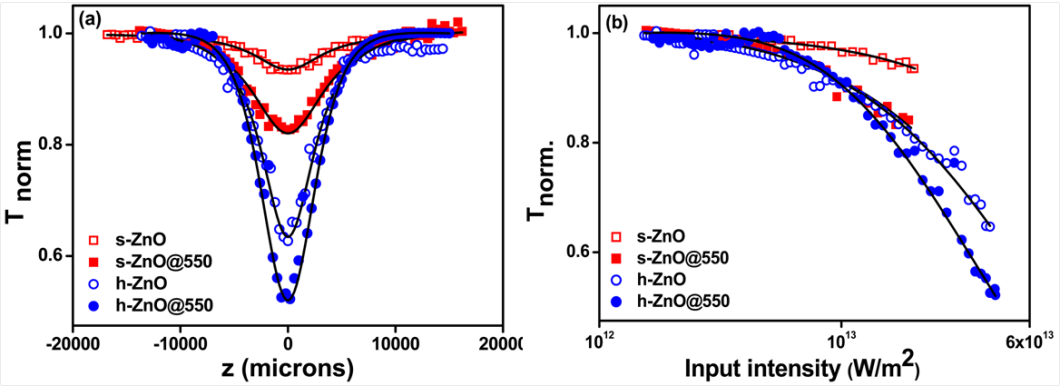

Figure 4.6 (a) Normalized open aperture Z-scan transmittance and (b) optical limiting response curve of s-ZnO, s-ZnO@550, h-ZnO and h-ZnO@550. Symbols denote experimental results while solid curves are theoretical fits to the data.

The *effective* nonlinear absorption coefficient (β_{eff}) is obtained by fitting the experimental Z-scan data with the theoretical plot. The effective nonlinear absorption has contribution from genuine two-photon absorption, reverse saturable absorption and nonlinear scattering. The data is found to fit best to a two-photon type absorption process. For an input energy of 150 μJ, the experimentally obtained values of β_{eff} and the saturation intensity (I_{sat}) are tabulated in table 4.4. Here the nonlinear absorption can occur through defect-assisted band-band excitation process by photons with lower energy than the bandgap. Intriguingly, the calcined samples exhibit stronger NLO behavior, and the β_{eff} increases with increase in calcination temperature, while the saturation intensity is reduced.

Table 4.4. Nonlinear absorption coefficient (β_{eff}) and saturation intensity of all ZnO samples

Sample	β_{eff} (cm/GW)	I_{sat} (GW/cm^2)
s-ZnO	0.8	9
s-ZnO@550	2.1	5
h-ZnO	2.5	3.9
h-ZnO@550	4.1	0.8

In principle, both oxygen vacancies ($V_{\ddot{O}}$ at 2.25 eV above the valence band maximum) and zinc vacancies ($V_{Zn}^{-2/-1}$ at 2.3 eV above the valence band maximum) can induce nonlinear absorption at high intensities of incident light. Nevertheless, as evident from the PL studies, the oxygen vacancies are passivated and zinc vacancies are slightly enhanced upon the calcination of the samples in air. Therefore, it is clear that, the enhancement in the NLO properties of ZnO after calcination originates from the Zn vacancies (V_{Zn}) rather than oxygen vacancies. It is evident that, as given in Fig 4.7, the electrons can be excited to V_{Zn} by the incident 532 nm (2.33 eV) laser pulses, populating the available intermediate states and inducing further absorption. Increase in Zn vacancies after calcination

enhances the density of states of V_{Zn}, thus populating more electrons and enhancing the nonlinear absorption.

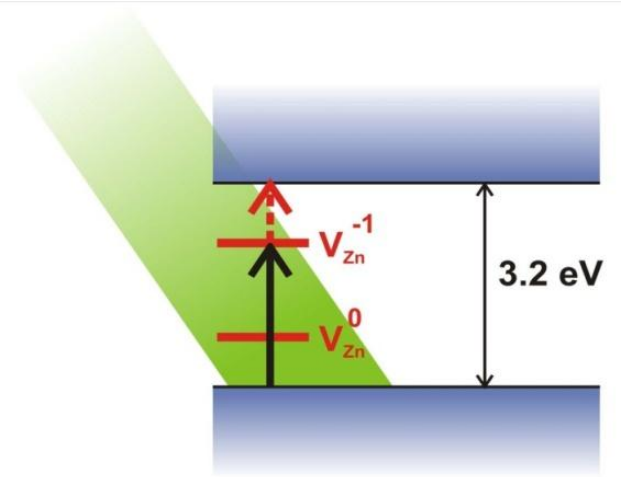

Figure 4.7. Zn-vacancy defect levels mediated in calcined ZnO, and the *effective* two-photon absorption mechanism of ZnO.

4.4. Conclusions

ZnO nanocones synthesized by a facile solution method have large oxygen vacancies creating two sub-band states, of which one is close to the valence band maximum and the other is close to the conduction band minimum in energy. The green photoluminescence emission of ZnO due to the defect-to-defect transitions is observed to be depleted after calcination of the samples in air, followed by a slight enhancement in the defect emission of the zinc vacancies. The reduction in visible light photocurrent after calcination indicates that defect levels due to oxygen vacancies are primarily responsible for the photoconductivity. Nonlinear absorption coefficients of the samples are enhanced significantly upon calcination, which clearly demonstrates that the nonlinearity originates from the sub-band states created by the zinc vacancies.

CHAPTER 5

SYNTHESIS OF REDUCED GRAPHENE OXIDE/ZnO HYBRID FOR VISIBLE LIGHT PHOTOCONDUCTIVITY AND OPTICAL LIMITING

In this chapter, the synthesis of reduced graphene oxide/ZnO by wet chemical method is discussed and identified the extent of deoxygenation of graphene oxide by structural characterization. Photoluminescence demonstrates how the defects in ZnO are modified in the presence of reduced graphene oxide and explained how this modification varies its photoconductivity and optical limiting properties.

5.1. Introduction

The wonder kid in carbon family, graphene has attracted tremendous interest in the field of material science due to its extraordinary physicochemical properties like high carrier mobility at room temperature, large specific surface area, good optical transparency and thermal conductivity (Geim and Novoselov, 2007). The most important challenge in graphene chemistry is its preparation by overcoming the strong exfoliation energy of π-stacked graphitic layers. Graphitic sheets can be exfoliated by micromechanical cleavage, chemical vapour deposition, high temperature thermal shock and chemical oxidation. The chemical oxidation of graphite dispersions into exfoliated sheets of graphene oxide is the most convenient methods to prepare exfoliated graphene in solution (Hummers and Offeman, 1958), as this method introduces functional groups on the two dimensional (2D) π-conjugated network or edges. By chemical functionalization, graphene may turn into a semiconductor with a tunable bandgap. Functionalization also gives a means for the anchoring of semiconductor, metal nanoparticles and small molecules on graphene sheets. Graphene-semiconductor hybrid materials have been identified as good candidate for photonic and

optoelectronic applications like solar cells, photodetectors, optical limiters and ultra fast lasers (Bao and Loh, 2012). This is due to the excellent electronic properties of graphene and its prominent capability to store and shuttle photogenerated electrons from the bandgap excitation of semiconductors upon light irradiation (Williams and Kamat, 2009).

Taking into account the excellent properties of ZnO and graphene, their hybrid can enable versatile properties with competence far beyond those of the individual members. The use of such hybrids to fabricate optoelectronic devices may offer advantages like lightweight, good stability and optical transparency. Recent literature shows that considerable effort has been made to attach ZnO nanostructures on graphene sheets for optoelectronic applications. Zhan et al. (2012) reported a self-powered, visible light photodetector based on reduced graphene oxide-ZnO hybrid nanostructure. Lee et al. (2009) demonstrated ZnO nanorod-graphene with good electrical conductance and good optical transparency compared to that of graphene layer, with ultraviolet and visible light emissions inherited from ZnO nanorods. Tian et al. (2012) developed a facile, one-step strategy towards the rapid synthesis of ZnO nanoparticle decorated reduced graphene oxide composite having application in photocurrent generation in the visible spectral region. Our aim is to modify the intrinsic defects in ZnO for tuning its below bandgap photoresponse and combine it with graphene for excellent photocurrent generation. This interest in ZnO/graphene hybrids is due to wavelength selectivity of ZnO and charge carrier mobility of graphene.

Materials with excellent optical limiting property are gaining interest since it can be utilised to protect delicate optical instruments, sensors, human eye, etc. from intense laser beams. Various materials like semiconductors (Jia, et al., 2004; Stryland, et al., 1988), organic dyes (Venugopal Rao, et al., 2002), polymers (Li, et al., 2004), metal nanoparticles (Suchand Sandeep, et al., 2010), carbon nanotubes (Sun, et al., 1998), fullerenes (Venturini, et al., 2002), graphene (Liu, Z. et al., 2009), etc, are studied as optical limiters. An optical limiting material with broadband limiting response, low limiting threshold intensity and

high damage threshold is ideal for practical applications. But no single material can meet all these application requirements. The fabrication of nanocomposite is a good approach to improve the nonlinear optical properties. Several research groups have studied the scope of graphene-porphyrin hybrid (Liu, Z. B., et al., 2009; Wang, A., et al., 2012; Xu, et al., 2009) for nonlinear optical applications. Even though porphyrin, phthalocyanine, etc. have excellent nonlinear optical response (Aneeshkumar, et al., 2003), lack of proper stability against thermal (Guermeur, et al., 1997) and optical bleaching (Bonnett and Martinez, 2000) limit their potential applications. The fabrication of graphene based materials with ZnO nanoparticles may overcome this disadvantage, because ZnO nanoparticles have good stability under prolonged laser irradiation.

In this chapter, a simple wet chemical approach for the *in-situ* growth of ZnO on the surface of reduced graphene oxide (rGO) by facile solution methods, namely; solution precipitation method and hydrothermal method is demonstrated. The structural analysis indicate that graphene possesses greater extend of π-conjugation in hydrothermally prepared samples. The interfacial interaction between intrinsic defects in ZnO nanostructures and graphene is discussed and correlated how the charge transfer pathways modify its visible photoconductivity and nonlinear optical properties.

5.2. Experimental

5.2.1. Synthesis of graphene oxide

Graphene oxide (GO) is prepared by chemical oxidation of graphite powder at low temperature. (1 g) Graphite powder is stirred with 98 % sulphuric acid for 12 h at room temperature. This mixture is cooled below 10 ℃ and potassium permanganate (4 g) is gradually added. The reaction mixture is stirred for 2.5 h while keeping the temperature below 10 ℃. Then 50 ml distilled water is added and stirred at room temperature for 30 min. The reaction is terminated by the addition of 150 ml of water and 30 % 10 ml H_2O_2. The dispersion is washed

by centrifugation and decantation, first with 5 % HCl solution and then with distilled water. The final product is dried at 60 ^{o}C under vacuum for 12 h.

5.2.2. Synthesis of reduced graphene oxide/ZnO

Reduced graphene oxide/ZnO (rGO/ZnO) hybrids are synthesized by the in-situ growth of ZnO on the surface of graphene oxide by two different routes namely hydrothermal synthesis and solution precipitation technique.

5.2.2.1. Hydrothermal synthesis of reduced graphene oxide/ZnO

Zinc acetate dihydrate is stirred with 0.05 % PVP solution (in 1 % acetic acid, 30 ml) for 30 min to form zinc acetate-PVP complex. GO is added to the above mixture and sonicated for 24 h to get a uniform dispersion. Different amounts of GO namely 10 mg, 20 mg, and 30 mg is added to the zinc acetate-PVP solution. For the precipitation of ZnO, NaOH solution is added, keeping the molar ratio of zinc acetate and NaOH solution as 1:6. The colloid formed is stirred for 30 min, and then it is transferred to a 50 ml teflon-lined stainless steel autoclave and heated in an oven at 100 ^{o}C for 7 h. After cooling to room temperature, the product is collected by centrifugation and washed with distilled water and dried at 100 ^{o}C. The powder obtained is designated as HGx, where x is the amount of GO in mg. Three set of rGO/ZnO products are prepared namely HG10, HG20 and HG30. ZnO is also synthesized by the same hydrothermal condition without adding GO as described in chapter 3.

5.2.2.2. Solution synthesis of reduced graphene oxide/ZnO

Zinc acetate dihydrate is stirred with 0.05 % PVP solution (in 1% acetic acid) for 30 min to form zinc acetate-PVP complex. GO is added to the above mixture and sonicated for 24 h to get a uniform dispersion. NaOH solution is added to precipitate ZnO and the colloid formed is stirred for 12 h at room temperature. The precipitate is filtered and dried at 100 ^{o}C. This sample is designated as SGx, where x is the amount of GO in mg. Different amount of GO is dispersed with Zn^{2+}, such that three set of products are obtained namely SG10,

SG20 and SG30.

5.3. Results and Discussions

5.3.1. Characterization of graphene oxide

Graphene oxide used in this study is prepared by the oxidation of pristine graphite, using reagents as in modified Hummers method (Sun, et al., 2008), but changing the temperature of oxidation to 10 ^{o}C. The XRD patterns of pristine graphite and graphene oxide (GO) are shown in Fig. 5.1. The pattern of pure graphite shows a peak at 2θ = 26.6^{o} corresponding to the basal spacing d_{002} = 0.34 nm and after oxidation the graphitic peak shifts to 10.2^{o} with increase of basal spacing to 0.86 nm. This increase in d spacing is due to the weakening of van der Waals interaction between the layers due to the intercalation of oxygen functional groups.

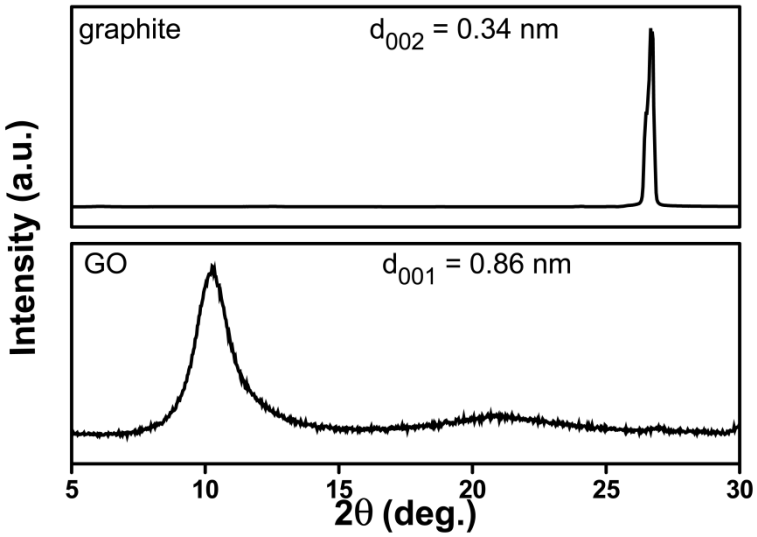

Figure 5.1. XRD patterns of graphite and GO

Fig. 5.2 shows the Raman spectra of the samples. The Raman spectrum of graphite shows an intense G band at 1577 cm^{-1} and a weak D band at 1336 cm^{-1}.The G band is assigned to the E_{2g} phonon of sp^2 carbon atoms and D band is a breathing mode of κ-point phonons of A_{1g} symmetry, originating from

the defects. After oxidation the intensity of D band is increased due to the introduction of more defects. The intensity ratio of D band to G band (I_D/I_G) of GO is 1.06 which is the measure of disorder, expressed by the sp^3/sp^2 carbon ratio. SEM image (Fig. 5.3) shows the folded nature of GO sheets which is due to the presence of strained epoxy groups and the rearrangement of hexagonal rings to 5 or 7 membered rings (Yoonessi and Gaier, 2010).

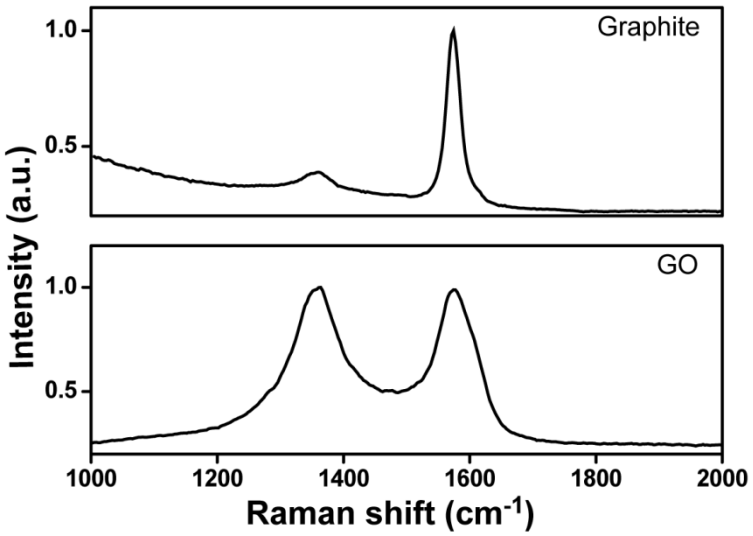

Figure 5.2. Raman spectra of graphite and GO

The presence of oxygen functionalities in GO is confirmed with TGA, IR and XPS. The decomposition of the samples is studied by TGA analysis and shown in Fig. 5.4. Graphite is stable in the temperature range up to 800 ^oC, whereas GO shows a major weight loss from 150-200 ^oC due to the loss of labile oxygen functional groups. Weight loss after 680 ^oC is due to the degradation of the carbon skeleton. The 8 % weight loss up to 150 ^oC is due to the loss of adsorbed water molecules. From the TGA analysis, oxygen percentage is calculated as 46 % (weight loss in the temperature range150-680 ^oC). Fig. 5.5 shows the IR spectrum of GO. The characteristic IR peaks at 1730 cm^{-1} assigned to C=O stretching vibrations of the –COOH groups, 3420 cm^{-1} for hydroxyl group stretching vibrations, 1402 cm^{-1} for C-O (carboxy), 1235 cm^{-1} for C-O (epoxy),

1075 cm^{-1} for C-O (alkoxy) and 1620 cm^{-1} for the skeletal vibrations of unoxidised graphitic domains prove the effective oxidation of graphite to GO.

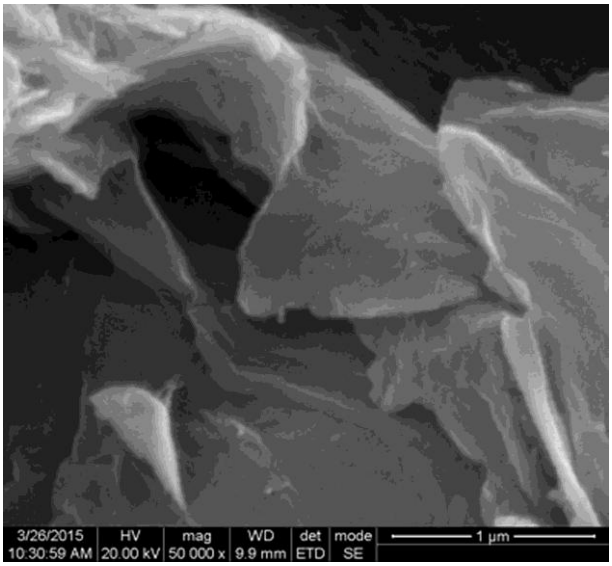

Figure 5.3. SEM image of GO

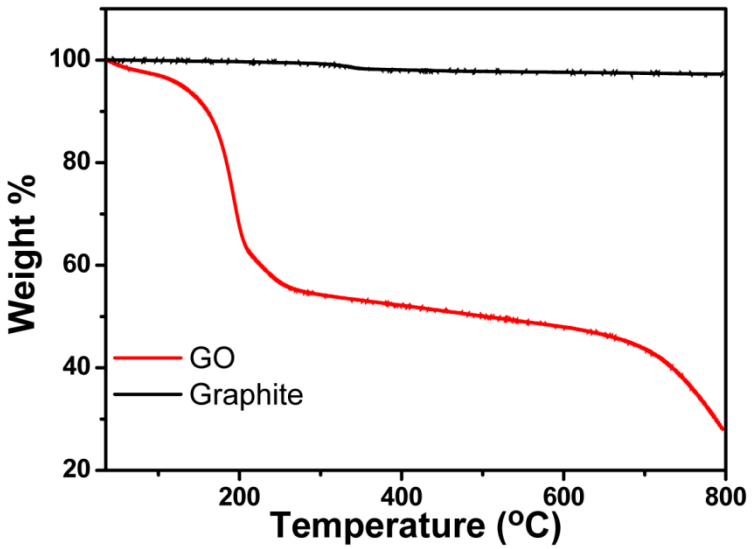

Figure 5.4. TGA of Graphite and GO

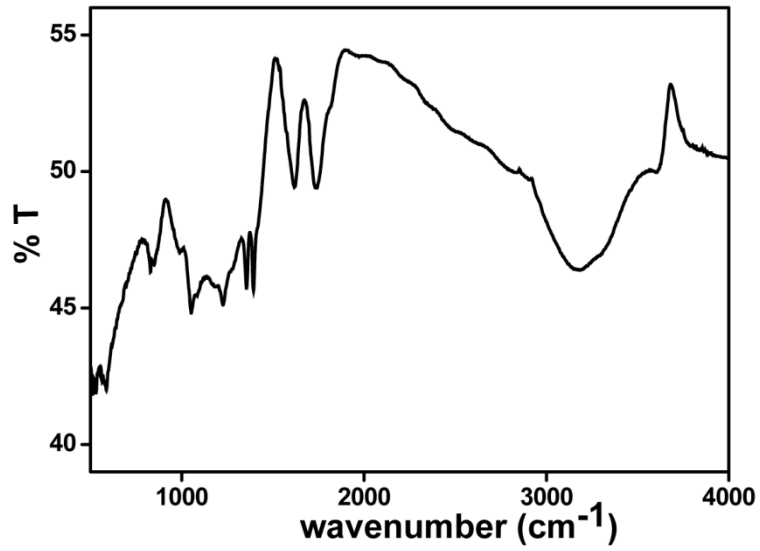

Figure 5.5. IR spectrum of GO

From the XPS survey spectrum (Fig. 5.6 a), oxygen content of GO is also calculated as 46 %. The high resolution C 1s spectra of GO is deconvoluted into five different states as given in Fig. 5.6 b. The peaks centred at 284.7, 286.1, 287.1, 288.7 and 289.5 eV can be assigned to the C=C, C-OH, epoxide, C=O and –COOH functional groups, respectively (Stankovich, et al., 2007; Wang, et al., 2013). GO prepared by this method have high oxygen content and different oxygenated functional groups, enable the GO nanosheets to react with ZnO precursors resulting in the nucleation of nanoparticles.

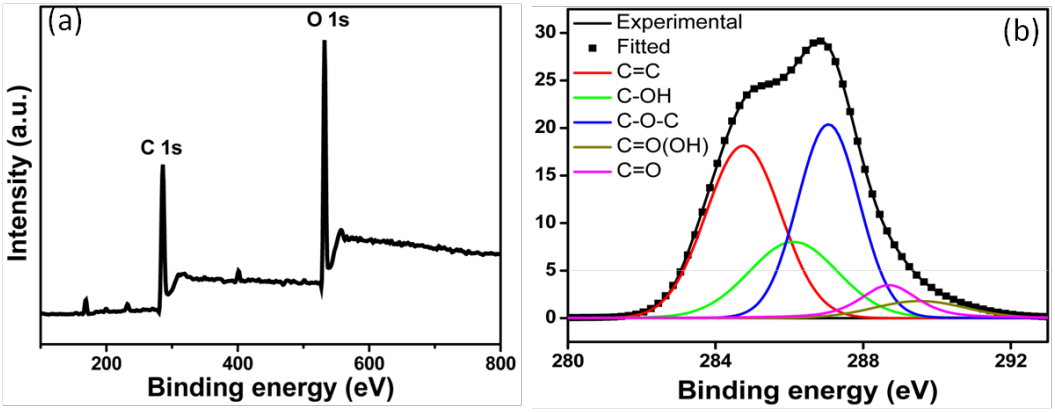

Figure 5.6. (a) XPS survey spectrum of GO (b) C1s spectra of GO

5.3.2. Characterization of reduced graphene oxide/ZnO

The reduced graphene oxide/ZnO hybrid is synthesized by two different routes namely solution precipitation technique and hydrothermal synthesis. In the solution method, Zn^{2+} precursor is dissolved in 1 % acetic acid and subsequently 0.05 % aqueous solution of PVP is added. This Zn^{2+}/PVP complex is sonicated with GO, Zn^{2+} ions get adsorbed on the surface of the GO sheets leading to exfoliation. The pH of Zn^{2+}/PVP/GO solution is found to be 4. When NaOH solution is added dropwise, pH of the solution slowly increases and turbidity starts to appear at a pH value of 6.4. The addition of NaOH is continued till the pH of the final solution is raised to 11. By the addition of NaOH, ZnO will get nucleated on the surface of the exfoliated graphene oxide sheets. The ZnO decorated exfoliated graphene oxide will be deoxygenated in the strong alkaline medium (Fan, et al., 2008) to give ZnO decorated reduced graphene oxide which is designated as SGx, where x is the amount of GO in mg.

For hydrothermal method, ZnO decorated exfoliated graphene oxide is heated at 100 ^{o}C. Exfoliated GO will undergo reduction under hydrothermal condition (designated as HGx) and this method is more effective than any other reduction methods in lowering the oxygen content and defect level on graphene sheets (Wang, H., et al., 2009). The extent of reduction of graphene oxide in SGx and HGx samples are compared with the help of characterization techniques.

The XRD pattern of the samples (Fig. 5.7) show that all the diffraction peaks are sharp, which indicate that ZnO formed are well crystallised. In the XRD pattern of hybrids the characteristic diffraction peak of GO or graphite is not observed, which indicates the exfoliation of layered graphene sheets due to the growth of ZnO nanoparticles (Xu, et al., 2008). After the formation of hybrid, the restacking of carbon sheets is prevented by the as-grown nanoparticles.

The TEM micrographs of HG30 and SG30 are shown in Fig. 5.8. This gives further evidence for the exfoliation of graphene sheets in presence of ZnO. When ZnO is synthesized in the absence of GO, TEM image indicate that ZnO

has cone shaped morphology (Fig. 3.12 b). During the *in-situ* growth of ZnO in presence of GO, TEM image shows that the cone shaped morphology is not maintained. In a typical ZnO wurtzite structure, number of alternating planes composed of tetrahedrally coordinated O^{2-} and Zn^{2+} are stacked along the c-axis. Such a crystal structure composed of basal polar oxygen plane $(000\bar{1})$ and top tetrahedral corner with exposed polar zinc plane (0001). When the ZnO nuclei is formed in presence of GO, the positively charged Zn plane can react with the functional groups of GO. Otherwise Zn^{2+} bonded to GO can combine with negatively charged oxygen plane of ZnO nuclei. During these reactions, chemical exfoliation occurs and the ZnO nanoparticles get partially covered by graphene sheets. Since the ZnO nanoparticles are partially surrounded by graphene sheets, the growth of ZnO to a well defined morhology is restricted. TEM image of HG30 indicate that ZnO nanoparticles are completely wrapped by graphene sheets, but in SG30 the interaction is relatively low.

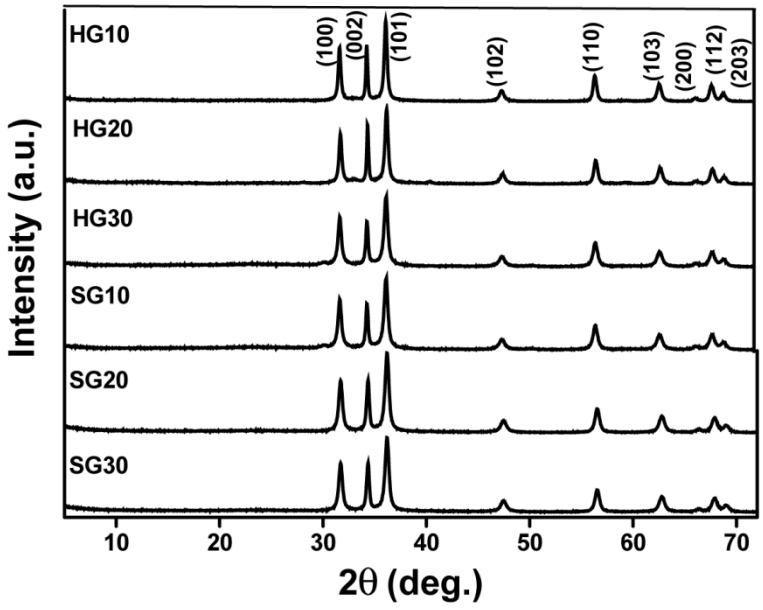

Figure 5.7. XRD patterns of HG10, HG20, HG30, SG10, SG20 and SG30

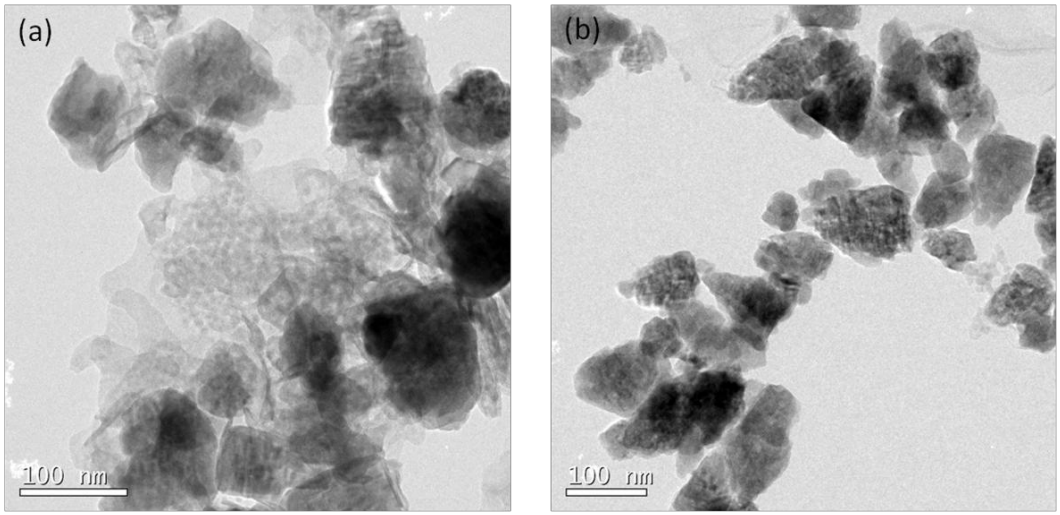

Figure 5.8. TEM images of (a) HG30 and (b) SG30

TGA, IR, Raman and XPS spectra of the samples are compared to find out the deoxygenation of graphene oxide in the hybrid by hydrothermal method and solution precipitation. TGA measurement provides a quantitative data about the deoxygenation of GO during the formation of the hybrid. Fig 5.9 shows thermogram of hybrids compared with pure ZnO (h-ZnO and s-ZnO) and GO. For h-ZnO and s-ZnO, weight loss of about 1.6 % and 2.5 %, respectively is observed in the temperature range 130 ^{o}C to 540 ^{o}C, which is due to the decompositon of chemisorbed PVP on the surface of ZnO. From the TGA analysis, oxygen percentage in GO is calculated as 46 % (weight loss in the temperature range 150-680 ^{o}C), but the weight loss for the hybrids at this range is significantly less indicating the reduction of GO by liberating oxygen functional groups during the formation of rGO/ZnO hybrid. GO has two significant weight loss starting at 150 ^{o}C and 650 ^{o}C. The former is the decomposition of labile oxygen functional groups and latter is due to the pyrolysis of carbon skeleton. Total weight loss in these temperatures is comparatively less for the rGO/ZnO prepared by solution (25 % loss for SG30) and hydrothermal treatment (18 % loss for HG30), indicating the deoxygenation of GO during the reaction. For the hydrothermally prepared rGO/ZnO, the weight loss around 150 ^{o}C is negligible because of the removal of labile oxygen functional groups during hydrothermal treatment. But the loss attributed to the pyrolysis of carbon skeleton is shifted to lower

temperature, may be due to the fragmentation of sp^2 domain. In solution precipitated rGO/ZnO, loss around 150 ^oC is significant due to the partial removal of labile oxygen functional groups.

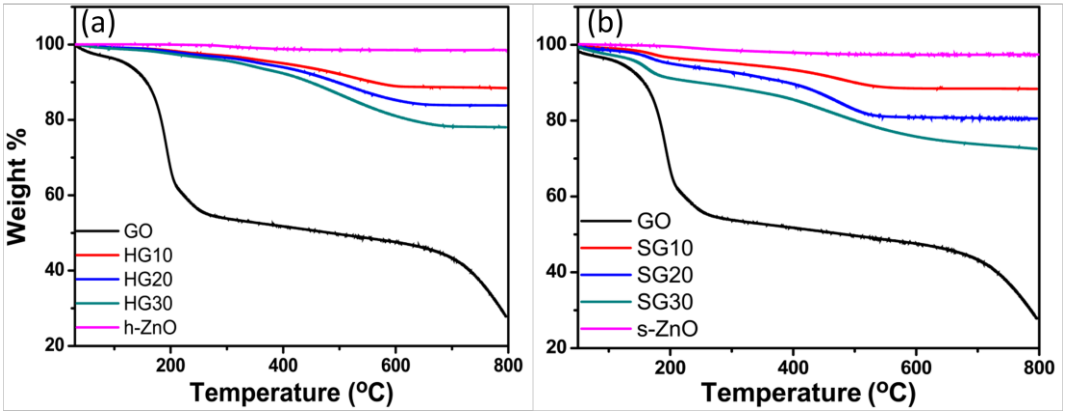

Figure 5.9. TGA of ZnO and GO compared with (a) hydrothermally prepared hybrids and (b) solution precipitated hybrids

The IR spectrum (Fig. 5.10) shows the decrease in oxygen functional groups in the hybrid compared to that in GO (Figure 5.5). But when comparing the IR spectra of HG30 and SG30, in SG30 peak at 1680 cm^{-1} indicates the presence of C=O in conjugation with C=C. But in both the samples the peak at 1730 cm^{-1} (C=O stretching vibrations of the –COOH groups) is absent, which may be due to the anchoring of ZnO on the graphene sheets. The absorption band at 410 cm^{-1} corresponding to the stretching vibration of Zn-O in the bulk ZnO is shifted to broad wavelength of 430-550 cm^{-1}. This shift may be due to the coordination of ZnO with functional groups on the graphene sheets.

The Raman spectra (Fig. 5.11) of SG30 and HG30 also show two characteristic bands namely G band at 1596 cm^{-1} and D band at 1345 cm^{-1}. In rGO/ZnO hybrids, the G band is blue shifted by 19 cm^{-1} and while the D band is red shifted by 11 cm^{-1} compared to GO. This shift in the Raman peak is due to the interaction between ZnO and reduced graphene oxide in the hybrid (Xu, et al., 2011). I_D/I_G ratios of SG30 and HG30 are 1.00 and 0.94 respectively (calculated

by averaging the spectra from five spots of the sample). For the hybrid, there is a decrease in I_D/I_G ratio compared to GO. But when the I_D/I_G ratio of SG30 and HG30 are compared, the latter exhibits slightly lower value. The decrease of I_D/I_G ratio in HG30 suggests that the hydrothermal method results in more graphene content without much fragmentation of sp^2 domain, which in turn indicates a better defect repairing mechanism (Luo, et al., 2011; Perera, et al., 2012). Therefore the hybrid synthesized by hydrothermal method have larger sp^2 domain and thus more extended π-conjugation.

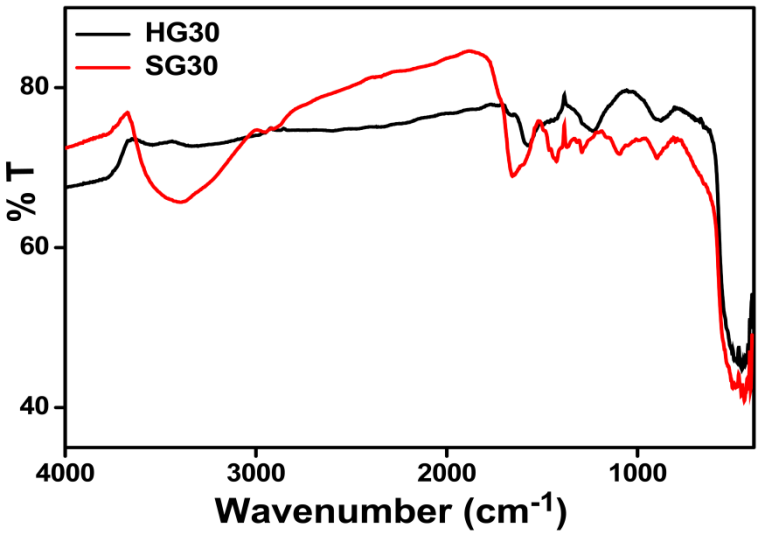

Figure 5.10. IR spectra of HG30 and SG30

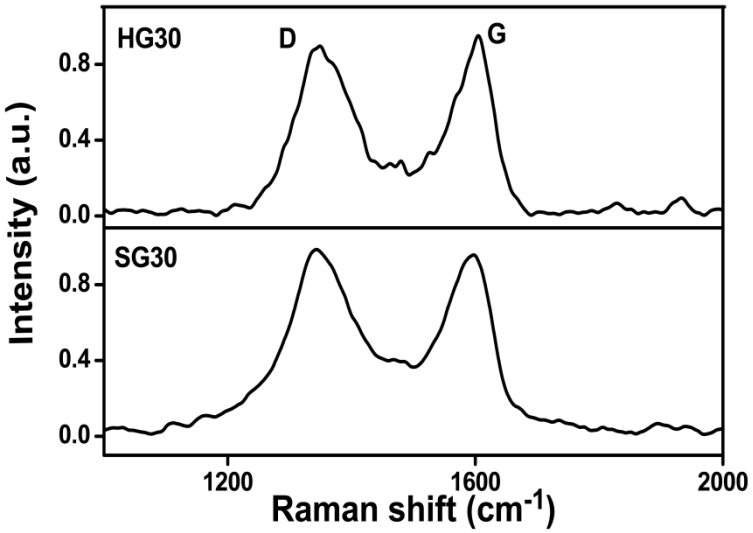

Figure 5.11. Raman spectra of HG30 and SG30

To further investigate the nature of oxygen functionalities in the hybrid, XPS spectra are taken. Fig. 5.12 illustrates the core level of C 1s XPS spectra of HG30 and SG30. Compared to GO, the relative intensities of oxygen functionalities are reduced in the C 1s spectra of the hybrids, indicating the deoxygenation of graphene oxide. In SG30, the C 1s signal is deconvoluted into sp^2 carbon (284.7 eV), C-OH (286.1 eV), C=O (288.7 eV) and –COOH (289.5 eV). But in C 1s spectra of HG30, the peak at 289.5 eV is absent, instead a peak at 290.2 eV corresponding to π-π* satellite appears indicating that the delocalised π conjugated domains are restored to some extend (Ganguly, et al., 2011). This suggests that, in hydrothermal reaction, besides the reduction of GO to reduced graphene oxide, the aromatic structures are recovered by repairing the defects (Nethravathi and Rajamathi, 2008a; Zhou, et al., 2009).

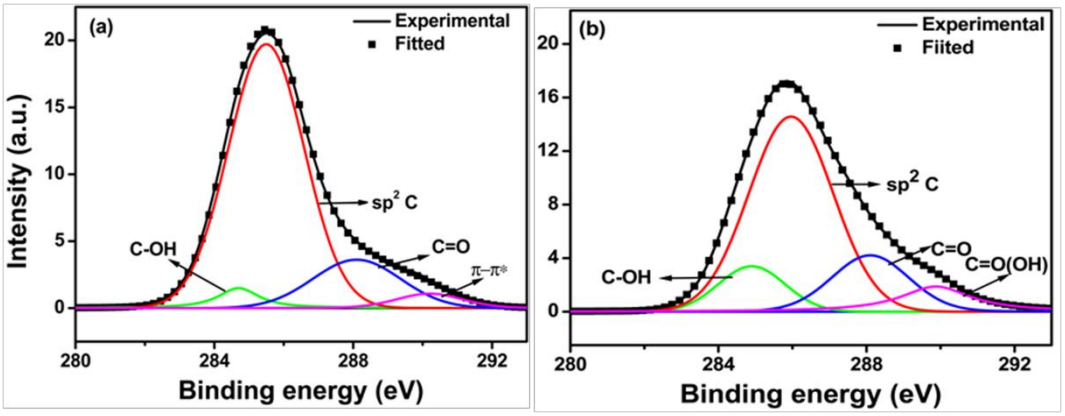

Figure 5.12. C 1s core level XPS spectra of (a) HG30 and (b) SG30

The UV-vis absorption spectra of reduced graphene oxide/ZnO hybrid prepared by hydrothermal method are shown in Fig. 5.13 a. The pure ZnO (h-ZnO) shows sharp band edge absorption at 362 nm. Compared with h-ZnO, rGO/ZnO hybrids, shows a broad background absorption in the whole visible region due to the presence of graphene. There is no noticeable correlation between carbon content and the broad visible absorption; this may be due to the scattering of light by aggregates of graphene particles (Catheline, et al., 2012). But the absorption edge of the hybrids is slightly shifted to higher wavelength indicating

the narrowing of bandgap. Fig. 5.13 b shows the estimation of its optical bandgap using the Tauc equation, the bandgap calculated for h-ZnO is 3.27 eV. While the bandgap of HG10, HG20 and HG30 are found to be 3.14 eV, 3.13 eV and 3.08 eV, respectively. This reduction in bandgap after the formation of rGO/ZnO may be due to the interaction of ZnO and π-electron cloud of graphene sheets (Lee, et al., 2012).

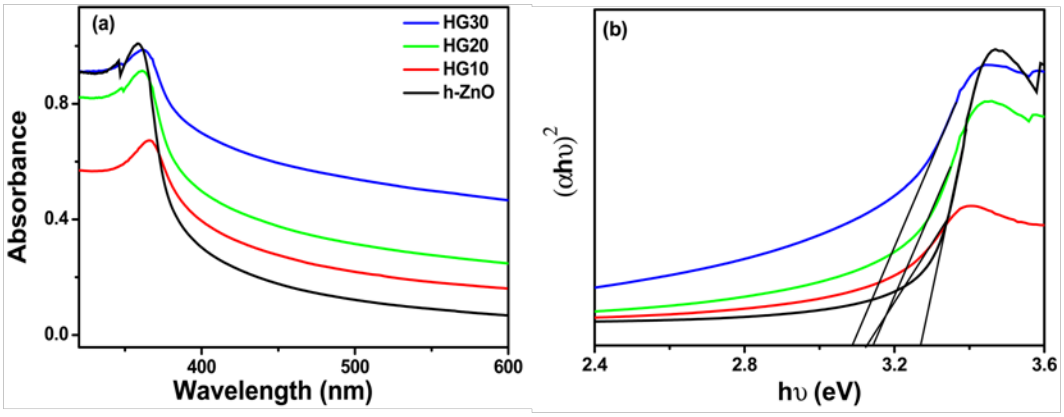

Figure 5.13. (a) UV-vis absorption spectra of ZnO and rGO/ZnO prepared by hydrothermal method (b) Corresponding Tauc plot for bandgap calculation

5.3.3. Formation mechanism of reduced graphene oxide/ZnO hybrid

The graphene oxide carries sufficient functional groups like epoxide, hydroxyls and carboxylic acid, which may render anchoring sites for ZnO nanoparticles. When Zn^{2+}/PVP complex is mixed with GO, Zn^{2+} gets adsorbed on the surface of GO. During the addition of NaOH, the crystal growth units $[Zn(OH)_4]^{2-}$ will form through the reaction between Zn^{2+} and OH^- in the presence of PVP. Both in hydrothermal and solution method, the hydrolysis of $[Zn(OH)_4]^{2-}$ as well as the reduction of GO occurs to give rGO/ZnO hybrid. The hydrolysis of $[Zn(OH)_4]^{2-}$ is accelerated by PVP, consuming the resultant water via binding water due to its excellent absorption ability (Kavitha, et al., 2014b; Zhang, J. et al., 2007). Thus PVP promotes the nucleation of ZnO at relatively low temperature. Since the reaction medium for the growth of ZnO is highly alkaline, the exfoliated GO will undergo deoxygenation (Fan, et al., 2008). Though the

mechanism of deoxygenation of GO in alkaline medium is not clear, it appears to be the reverse of the oxidation of graphite in strong acids (Hummers and Offeman, 1958). Therefore in solution precipitation (SG30) itself, GO will undergo chemical reduction. When this colloid is heated hydrothermally, the temperature and internal pressure will promote the recovery of π-conjugation. This defect repairing mechanism in hydrothermal method enhances the interaction between ZnO and graphene layers.

5.3.4. Photoluminescence spectra and Lifetime measurements

Fig. 5.14 shows the room temperature photoluminescence spectra of h-ZnO, HG10, HG20 and HG30. In all the samples there is a sharp emission in the ultraviolet region due to the band-to-band radiative recombination of excitons, and a broad green emission centred at 2.25 eV, together with a minor blue emission peak at 2.69 eV. No appreciable shift is observed in the excitonic emission of rGO/ZnO compared to pure ZnO, but there is considerable fluorescence quenching, suggests additional pathways for the disappearance of charge carriers by the interaction between excited ZnO and graphene sheets. As GO concentration is increased, the extent of PL quenching is also increased. The decrease in fluorescence yield of the band edge emission may be due to the interfacial charge transfer between ZnO and graphene sheets (Son, et al., 2012; Williams and Kamat, 2009). Guo et al. (2013) explored that upon excitation with photon energy larger than the bandgap, electron-hole pairs are generated in ZnO. The holes trapped at the surface facilitate the discharge of adsorbed oxygen ions. Then the unpaired electrons transferred to the graphene layer, because the conduction band of ZnO is higher than that of graphene.

The broad visible emission is attributed to the defects in ZnO. When the concentration of GO is increased, the intensity of defect emission is also decreased compared to h-ZnO. In h-ZnO, green emission centred at 2.25 eV is due to the capture of holes by $V_O^{\cdot}$ to generate $V_O^{\cdot\cdot}$, followed by a transition between $V_O^{\cdot\cdot}$ to the valence band. The emission peak at 2.69 eV can be attributed to the transition between the conduction band and the V_{Zn} acceptor level. The quenching

in visible emission in the hybrid may be due to the passivation of defects in ZnO during the formation of rGO/ZnO.

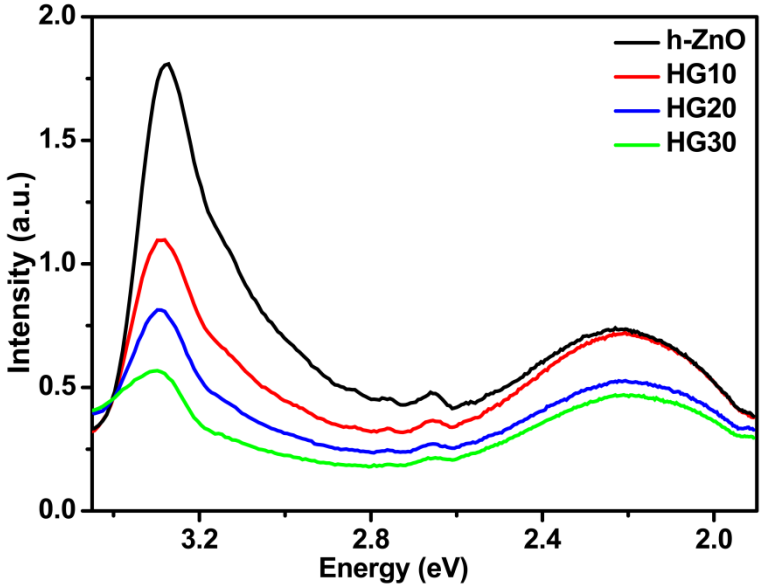

Figure 5.14. Photoluminescence spectra of ZnO and rGO/ZnO prepared by hydrothermal method.

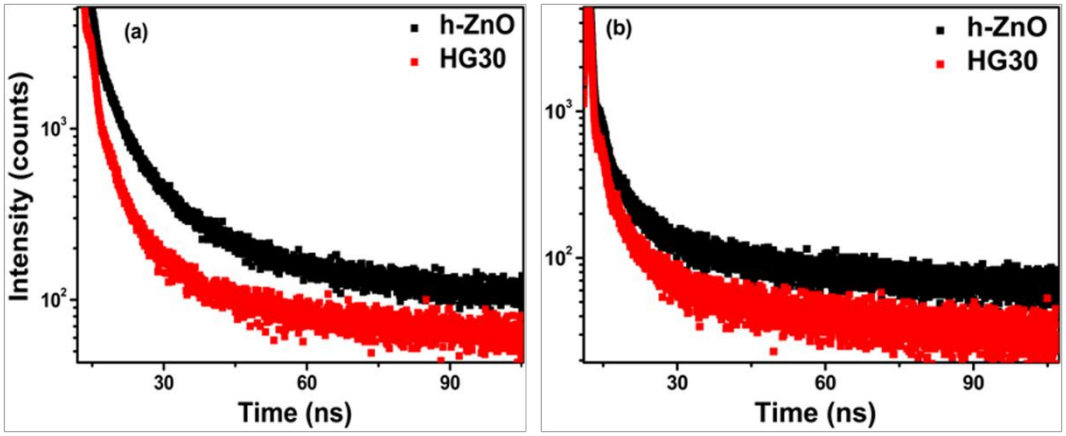

Figure 5.15. Fluorescence decay curves measured by TCSPC for h-ZnO and HG30. The excitation wavelength is 340 nm. Emission is monitored at (a) 550 nm and (b) 460 nm

TCSPC technique is used to study the relaxation kinetics of photogenerated charge carriers in ZnO leading to defect emission and to monitor how the defect states are modified after hybridising with graphene. The samples are excited using 340 nm laser source and the emission lifetime is measured. The

temporal decay of emission at 2.25 eV (550 nm) and 2.69 eV (460 nm) is monitored, and the obtained decay kinetics is shown in Fig. 5.15. The experimental values are fitted to a biexpontential model. The decay of visible emission comprises of two components, namely, a fast component (τ_1) and a slow component (τ_2), knowing which the average lifetimes of the samples can be calculated and are tabulated in Table 5.1 and 5.2.

While comparing h-ZnO and rGO/ZnO, there is significant decrease in the average lifetime at 550 nm for rGO/ZnO. This suggests the possibility of healing of surface oxygen vacancies during the growth of ZnO on graphene sheets. This repairing of oxygen vacancies may be due to the diffusion of oxygen from graphene oxide (Yoo, et al., 2014). During the hydrothermal treatment in basic medium, the oxygen released from graphene oxide under reduction (Fan, et al., 2008), can heal out the oxygen vacancies on ZnO surface. But the carrier lifetime probed at 460 nm, there is no appreciable change in the average lifetime of h-ZnO and rGO/ZnO. This blue emission is attributed to the Zn vacancies, suggesting retention of its defect states in rGO/ZnO.

Table 5.1. Lifetime analysis of emission at 550 nm

Sample	χ^2	A_1	τ_1(ns)	A_2	τ_2 (ns)	$<\tau>$
h-ZnO	1.16	0.47	6.39	0.53	98.9	93.88
HG10	1.21	0.52	5.96	0.53	98.95	73.16
HG30	1.31	0.50	4.64	0.47	78.73	36.14

Table 5.2. Lifetime analysis of emission at 460 nm

Sample	χ^2	A_1	τ_1(ns)	A_2	τ_2 (ns)	$<\tau>$
h-ZnO	1.14	0.53	3.12	0.47	15.68	13.34
HG10	1.32	0.63	3.45	0.36	16.77	13.24
HG30	1.29	0.63	3.525	0.36	15.19	11.86

5.3.5. Visible light photoconductivity in rGO/ZnO

The photocurrent experiments are performed using Autolab electrochemical workstation using a three electrode cell. Fig. 5.16 shows the photocurrent measured for h-ZnO and HG30 samples as a function of time at –0.5 V bias voltage with light on-and-off cycles in an interval of 60 s. The value of dark current, photocurrent and on-off difference of h-ZnO are -35.72, -45.72 and 10 μA/cm^2, respectively while that of HG30 are -49.04, -54.36 and 5.32 μA/cm^2, respectively. While comparing the dark conductivity of h-ZnO and HG30 at –0.5 V, there is an improvement in conductivity of HG30 due to the presence of reduced graphene oxide. Under applied voltage the electrons will move from graphene due to its lower resistance towards ZnO (Singh, G, et al. 2012). This type of rGO/ZnO heterostructure with excellent conductivity is in demand for electronic devices. When irradiated with light, the photoresponse of HG30 is lower than that of the h-ZnO. Oxygen vacancies have a critical role in the visible photoconductivity in ZnO. In HG30 the green emission corresponding to oxygen vacancies are passivated during the reduction of graphene oxide. The defect mediated below bandgap absorption will be less and it will reduces its visible photoconductivity due to less photoinduced charge transfer.

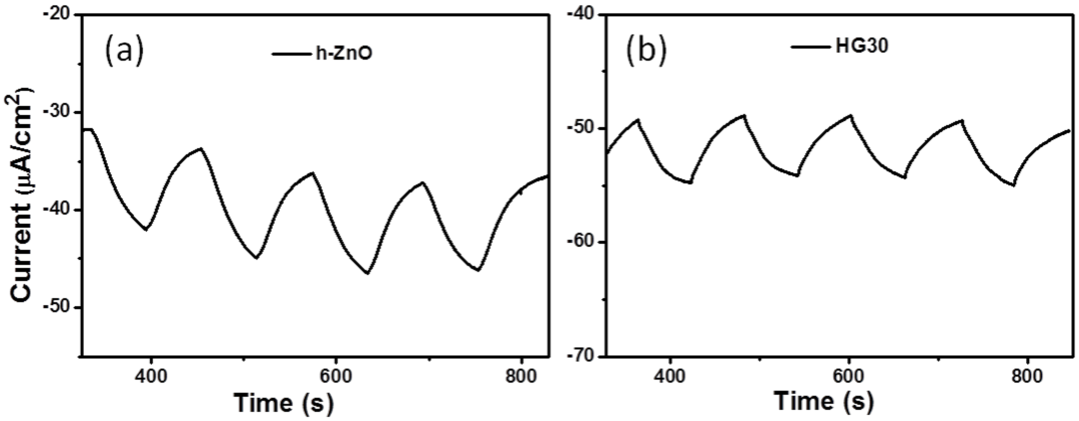

Figure 5.16. Photocurrent measurement of (a) h-ZnO, (b) HG30 at –0.5 V bias voltage

5.3.6. Nonlinear absorption and optical limiting

Open aperture Z-scan technique is employed to measure the nonlinear absorption and optical limiting property of the colloids of pure ZnO and rGO/ZnO hybrid (1 mg/ml of water). The open aperture curve exhibits a normalized transmittance valley, indicating the presence of reverse saturable absorption (RSA) in the colloids. This suggests the scope of this material as a good optical limiter. Different mechanisms exist for RSA such as two photon absorption (TPA), excited state absorption (ESA) and nonlinear scattering. The theoretical plot for two-photon absorption process fit well with the experimental data.

For an input energy of 30 μJ and 65 % linear transmittance, the normalised transmittance as a function of distance for the nanopowder dispersed in water is shown in Fig. 5.17. Compared to bare ZnO and GO dispersions, HG30 shows enhanced nonlinear optical (NLO) properties, because of the combination of NLO mechanism of ZnO and reduced graphene oxide. In case of ZnO defect states play a critical role in nonlinear absorption. When ZnO is irradiated with 532 nm (2.33 eV) laser pulses, the defect mediated below bandgap absorption can be assisted by both oxygen vacancies and zinc vacancies. From the PL studies it is found that during the growth of ZnO on rGO surface, oxygen vacancies get passivated while there is no appreciable change in Zn vacancy states. Therefore in ZnO an *effective* nonlinear absorption process originates from Zn vacancies. For graphene oxide, excited state absorption is the dominating nonlinear absorption mechanism in the nanosecond regime (Liu, Z. et al., 2009). As shown in Fig.5.17, HG30 has the largest dip among the normalised transmittance curves. Therefore, HG30 exhibits better optical limiting behaviour compared to GO and ZnO (Kavitha, et al., 2013b). When irradiated with laser, electrons in ZnO get excited to V_{Zn} states, populating the intermediate states and induce further absorption. These photo-excited electron can be transferred to the unoccupied states of graphene sheets (Guo, et al., 2013). This photoinduced electron transfer plays a significant role for the enhanced optical limiting behaviour for this hybrid material. The value of β_{eff} can be evaluated from the theoretical fitting of the Z-scan experimental data. The normalised transmittance curve fitted with two-

photon absorption and the corresponding value of β_{eff} and I_{sat} are summarised in Table 5.3. Compared to GO, all the hybrids show an increase in nonlinear absorption coefficient and optical limiting efficiency. When the loading of GO is increased the optical limiting efficiency is also increased. The mechanism for the optical limiting behaviour of the hybrid may be due to the combination of two-photon absorption, excited state absorption and electron transfer between ZnO and graphene sheets. During the synthesis of rGO/ZnO, the epoxy and hydroxyl groups on the surface of GO are partially removed by the addition of NaOH, which increases the conjugation network of the nanostructure of graphene. The more the extended conjugation, the higher is the chance for electron transfer resulting in enhanced optical limiting.

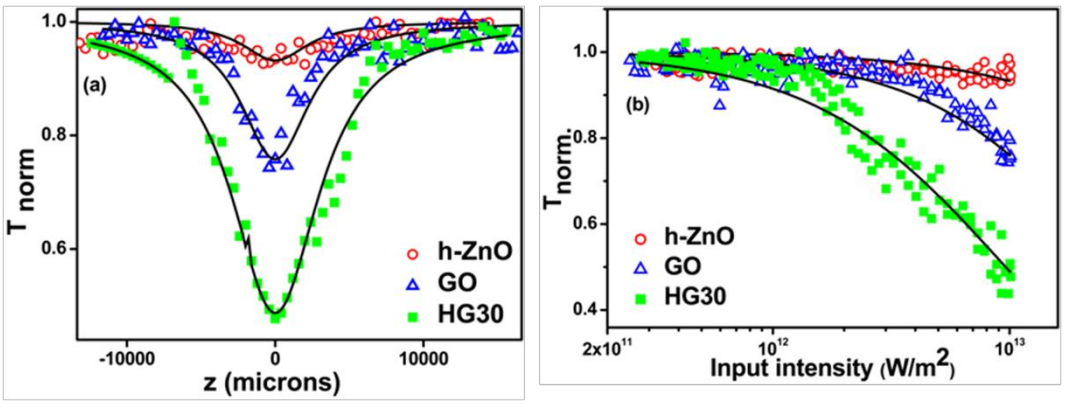

Figure 5.17 (a) Normalized open aperture Z-scan transmittance and (b) optical limiting response curve of h-ZnO, GO and HG30. Symbols denote experimental results while solid curves are theoretical fits to the data.

Table 5.3. Nonlinear absorption coefficient (β_{eff}) and saturation intensity (I_{sat}) of rGO/ZnO samples compared with pure ZnO

Sample name	β_{eff} cm/GW	I_{sat} GW/cm^2
h-ZnO	0.95	5
GO	5.4	1.7
HG10	7.5	0.95
HG30	15	1.8

5.4. Conclusions

Reduced graphene oxide/ZnO hybrid is synthesized via solution precipitation technique and hydrothermal method. All the characterization techniques like FTIR, XPS, TGA, TEM and XRD adopted for this study reveals the exfoliation of GO due to the adherence of ZnO on the surface of the graphene sheets. When ZnO is precipitated in alkaline medium GO undergoes reduction, which is further reduced under hydrothermal treatment, due to the temperature and internal pressure. It helps in the recovery of π-conjugation in rGO. This defect repairing mechanism in hydrothermal method enhances the interaction between ZnO and graphene layers. Compared to ZnO, fluorescent quenching is observed for the hybrids indicating photoinduced electron transfer between ZnO and graphene layers. The dark conductivity of rGO/ZnO is improved due to the presence of graphene. TCSPC measurements indicate that in rGO/ZnO oxygen vacancy defect states are healed out by diffusion of oxygen from GO to ZnO while Zn vacancy states are retained. Because of the passivation of oxygen vacancies, visible light photoconductivity of the hybrid is depleted, compared to

pure ZnO. Though the photocurrent is low, its excellent dark conductivity suggests the scope of this material in electronic applications. ZnO decorated graphene sheets exhibit good nonlinear absorption than its individual counterparts, suggesting the Zn vacancy state assisted *effective* nonlinear absorption with photoinduced electron transfer between ZnO and graphene sheets. These results suggest that rGO/ZnO is a good candidate for optical limiting material.

CHAPTER 6
REDUCED GRAPHENE OXIDE/ZnO HYBRID FILMS BY LAYER-BY-LAYER SELF ASSEMBLY FOR PHOTOCURRENT GENERATION AND NONLINEAR ABSORPTION

In this chapter, the fabrication of multilayer films reduced graphene oxide/ZnO hybrid by layer-by-layer self assembly is described. Combining the advantages of ZnO having below bandgap photoresponse and graphene with extremely high carrier mobility, these reduced graphene oxide/ZnO films are used for photocurrent generation and nonlinear absorption.

6.1. Introduction

The control of defect states and associated charge carriers play an important role in the optoelectronic properties of ZnO. During the *in-situ* growth of ZnO on graphene surface there is a reduction of oxygen vacancy states in ZnO due to the diffusion of oxygen from graphene oxide to ZnO. The variation in these defect states are discussed in detail in chapter 5. Since the oxygen vacancy states play an important role in the below bandgap photoresponse of ZnO, an *ex-situ* method to combine ZnO and graphene, which will not affect the defect states in ZnO, is proposed. Reduced graphene oxide/ZnO films are fabricated by layer-by-layer (LBL) self assembly technique, in which ZnO is bound to graphene by electrostatic interaction.

LBL self assembly technique makes use of adsorption of oppositely charged polyelectrolytes to build up multilayer structures (Decher, et al., 1992; Iler, 1966; Park, et al., 2011). Langmuir Blodgett technique (Li, X., et al., 2008) and chemical self assembly (Song, S., et al., 2014) are other two versatile techniques used to build hierarchical nanostructures. Though these techniques

help to construct films of long range molecular order, it has poor stability, limited to few substrates and the deposition process is very slow. For LBL films, even though they have low molecular order, they have the advantage of high strength, ease of preparation and possibility to deposit on any substrate. In LBL technique, multilayer films are fabricated by the alternate adsorption of polyelectrolytes, the interaction between the layers may be hydrogen bonding (Kharlampieva, et al., 2009), charge transfer interaction (Shimazaki, et al., 2000), electrostatic interaction, etc. In electrostatic LBL assembly, cationic and anionic polymers are deposited alternately on the substrate (Li, Z., et al., 2011; McClure, et al., 2009). In addition to polyelectrolytes deposition, metal (Chirea, et al., 2005) and semiconductor nanoparticles (Eita, et al., 2014), biomolecules (Lu, et al., 2009), etc can be arranged hierarchically by this method.

Here multilayer films of ZnO and reduced graphene oxide is fabricated by electrostatic layer-by-layer technique. The electrostatic layer-by-layer self assembly technique provides an effective approach for the fabrication of ordered multilayer films with controllable properties of both ZnO and graphene. Short recombination lifetime of graphene limits its optoelectronic applications. Combining graphene with semiconductor nanoparticles help to overcome this limitation by means of electron transfer that will help to extend the recombination time of the charge carriers. But poor dispersion of graphene in aqueous medium hinders the uniform growth of the multilayer film. It can be overcome by preparing a negatively charged homogenous reduced graphene oxide dispersion by the reduction of graphene oxide in presence of poly(sodium 4-styrene sulfonate) (PSS) (Stankovich, et al., 2006). A positively charged ZnO dispersion is prepared by dispersing hydrothermally prepared ZnO (h-ZnO) in acidified solution of polyacrylamide (PAM). Then the multilayer films are constructed using negatively charged PSS coated reduced graphene oxide (PSS-rGO) and positively charged dispersion of ZnO in PAM (PAM-ZnO). The growth and surface morphology of these films are studied using UV-vis absorption spectra and SEM. By measuring the photoconductivity of these multilayer films, the role of defects in ZnO for the photocurrent generation is confirmed. Using open

aperture Z-scan technique, the nonlinear absorption of the multilayer films is measured.

6.2. Experimental

6.2.1. Synthesis of PSS coated reduced graphene oxide

1 mg/ml of aqueous solution of GO is prepared by ultrasonication to form a colloidal suspension. 4 g of PSS is dissolved in this colloidal solution, followed by the addition of 100 μL hydrazine hydrate and it is refluxed at 70 ^{o}C for 4 h. Finally a stable suspension of reduced graphene oxide is obtained; which is repeatedly washed with distilled water until the pH of the colloid become neutral. The reduction and exfoliation of graphene oxide in presence of PSS is analysed by XRD, XPS and TEM analysis. For the fabrication of multilayer films, the pH of PSS-rGO dispersion is adjusted to nine by the addition of 1 M NaOH solution. Due to the presence of the anionic PSS, this graphene dispersion will carry a negative charge.

6.2.2. Preparation of ZnO dispersion in PAM

About 4 % polyacrylamide solution is prepared in water and pH of the solution is adjusted to 2 by adding 1 M HCl solution, such that a positively charged polyelectrolyte is obtained (Shen, et al., 2009; Shen, et al., 2008). To this cationic polyelectrolyte, ZnO nanocones (h-ZnO) synthesized by hydrothermal method are dispersed by ultrasonication.

6.2.3. Fabrication of reduced graphene oxide/ZnO films by layer-by-layer self assembly

Reduced graphene/ZnO (rGO/ZnO) multilayer films are fabricated by electrostatic layer-by-layer self assembly technique using negatively charged PSS-rGO and positively charged PAM-ZnO as building blocks. The multilayer films are deposited on quartz and fluorine doped tin oxide (FTO) coated glass

substrates by alternate spin coating of positively charged PAM solution (pH = 4) containing 0.5 mg/ml of h-ZnO and negatively charged solution of PSS-rGO (0.5 mg/ml, pH = 9). After coating each layer the substrate is washed with distilled water to remove weakly adsorbed materials. This sequence is repeated to get desired number of layers, designated as $(PAM\text{-}ZnO/PSS\text{-}rGO)_n$, where n is the number of bilayers. UV-vis absorption spectra of multilayer films on quartz are recorded after coating each bilayer in order to monitor its uniform deposition. The morphology of the films in FTO substrate is characterized by scanning electron microscopy.

6.3. Results and Discussions

6.3.1. Characterization of PSS coated reduced graphene oxide

PSS coated reduced graphene oxide (PSS-rGO) is obtained by the reduction of graphene oxide in presence of aqueous solution of PSS. Normally during the reduction of aqueous solution of graphene oxide, the oxygen functionalities in the graphitic layers will reduce, results in the decrease of its hydrophilic character. This causes the rapid irreversible agglomeration and precipitation of graphene. But when the reduction of graphene oxide is done in presence of the anionic polymer PSS, a stable dispersion of reduced graphene oxide can be prepared. XRD, XPS and TEM analysis are employed to analyse the reduction and formation of PSS-rGO.

The XRD patterns of graphite, GO and PSS-rGO are shown in Fig. 6.1. Graphite shows a characteristic peak at $2\theta = 26.7^o$ corresponding to (002) plane with d-spacing of 0.334 nm, is shifted to a broad peak at $2\theta = 10.3^o$ with increase of basal spacing to 0.862 nm in GO. For PSS-rGO, the peak at $2\theta = 10.3^o$ disappears and the broad graphitic peak reappears at $2\theta = 23.5^o$ with d-spacing 0.430 nm. The shift of graphitic peak at 26.7^o to 23.5^o in PSS-rGO may be due to intercalation of the polymer and presence of residual oxygen functionalities on graphene layers (Remyamol, et al., 2014a). The decrease in basal spacing of PSS-rGO compared to GO indicate the reduction of graphene layers. The broadening

of XRD peak is due to the small size and short range order of graphene layers. (Dubin, et al., 2010).

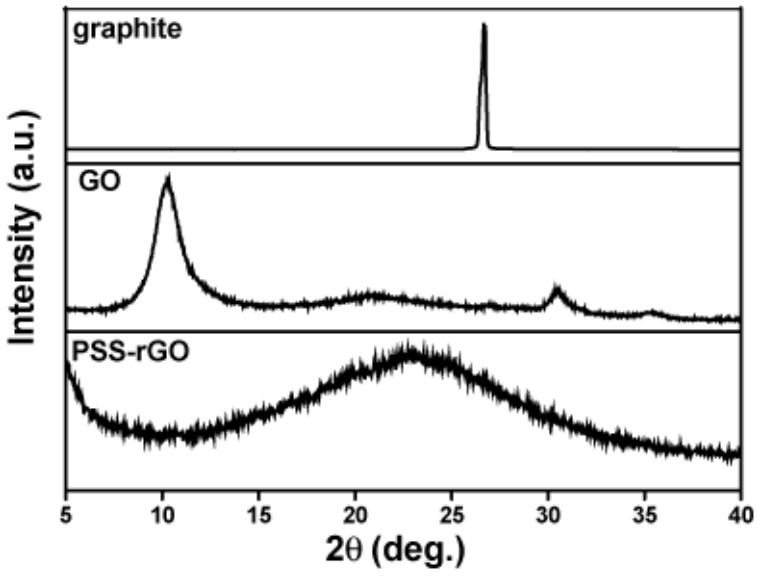

Figure 6.1. XRD patterns of graphite, GO and PSS-rGO

Fig. 6.2 shows the TEM image and selected area electron diffraction (SAED) pattern of PSS-rGO. TEM image shows that PSS-rGO consists of partially folded few layered reduced graphene oxide sheets. SAED pattern does not contain any well defined hexagonal pattern indicate that rGO is not highly crystalline, due to the presence of PSS. X-ray photoelectron spectroscopy (XPS) is employed to analyze the extend of reduction of graphene oxide after coating PSS. The C 1s spectra of GO clearly indicate considerable degree of oxidation with carbon in different functional groups (Fig. 6.3a). But in C 1s spectra of PSS-rGO, the intensities of peaks corresponding to oxygen functionalities are considerably reduced, indicating the deoxygenation of graphene oxide (Fig. 6.3b). In addition, there is a peak at 285.2 eV corresponding to sulphur bonded carbon in PSS-rGO. By the reduction of graphene oxide in presence of PSS, a stable aqueous dispersion of graphene nanoplatelets is obtained. Excellent dispersion is essential for the making multilayer films. It is observed that large concentration of PSS is required to prevent the agglomeration of reduced graphene oxide. During reduction, PSS are intercalated between the graphene layers which will reduce the

hydrophobic interaction between the layers. This PSS-rGO will remain as stable dispersion for several months.

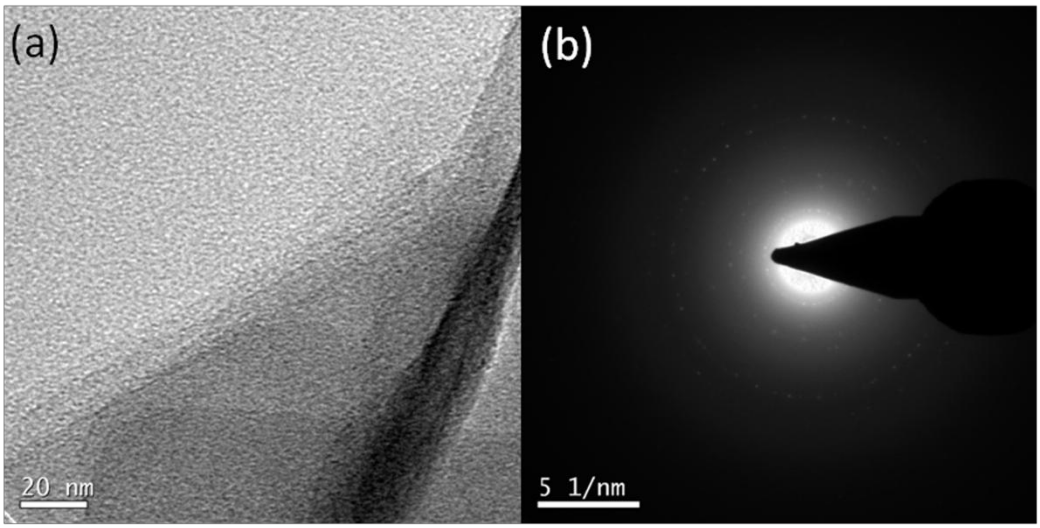

Figure 6.2. (a) TEM image (b) SAED pattern of PSS-rGO

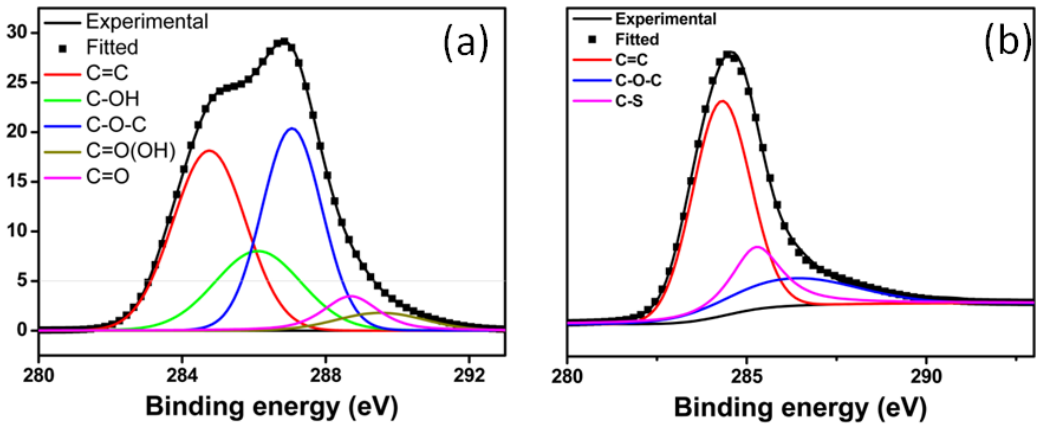

Figure 6.3. C 1s XPS spectra of (a) GO (b) PSS-rGO

6.3.2. Growth and characterization of multilayer films

Electrostatic LBL technique is employed for the fabrication of rGO/ZnO multilayer films. The cationic (PAM-ZnO) and anionic (PSS-rGO) polyelectrolytes are alternately spin coated on FTO glass. The consecutive growth of multilayer films is examined by UV-vis absorption spectra, after the deposition of each bilayer. For the measurement of UV-vis absorption spectra, the films are coated on quartz substrate. Fig. 6.4 a shows the UV-vis absorption spectra of

$(PAM\text{-}ZnO/PSS\text{-}rGO)_n$.where n is the number of bilayers which is varied from 3 to 9. The ZnO and PSS-rGO exhibit two characteristic peaks at 360 nm and 270 nm, respectively. The linear increase in peak absorbance at 360 nm and 270 nm with the number of bilayers (Fig. 6.4 b) indicates that the deposition is uniform in terms of layer-by-layer.

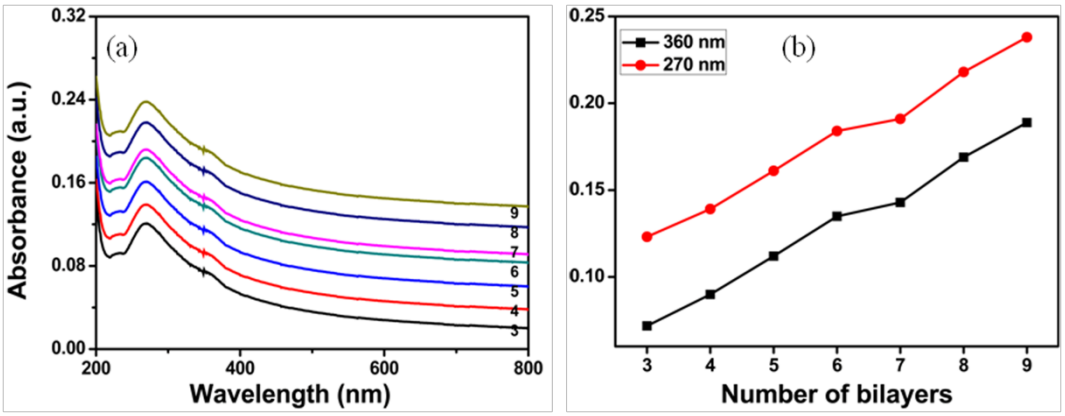

Figure 6.4 (a) UV-vis absorption spectra of $(PAM\text{-}ZnO/PSS\text{-}rGO)_n$ on quartz substrate (b) The plot of absorbance at 270 nm and 360 nm vs the number of bilayers.

The surface of $(PAM\text{-}ZnO/PSS\text{-}rGO)_3$, $(PAM\text{-}ZnO/PSS\text{-}rGO)_5$, and $(PAM\text{-}ZnO/PSS\text{-}rGO)_9$ multilayer films coated on FTO substrate are uniform as shown in Fig. 6.5. SEM image shows that the increase in number of bilayers makes the surface of the film more dense and continuous. The close examination of Fig. 6.5a reveals that the surface of the three bilayer film is rough and porous with the ZnO nanocones projected out. By the adsorption of more and more bilayers, the surface becomes smooth due to the covering of lamellar graphene sheets (Fig. 6.5, b and c). Fig. 6.6 shows the cross-sectional SEM image of $(PAM\text{-}ZnO/PSS\text{-}rGO)_9$, there is no observable separation between the bilayers indicating the good interaction between the bilayers. The growth of uniform films by the addition of more bilayers may be due to two reasons. (1) the electrostatic force of attraction between the oppositely charge polyelectrolytes namely PAM and PSS. (2) hydrogen bonding between acetylamine groups of polyacrylamide chains and the aromatic structures of graphene sheets incorporated with PSS (Yang, Y., et al., 2013).

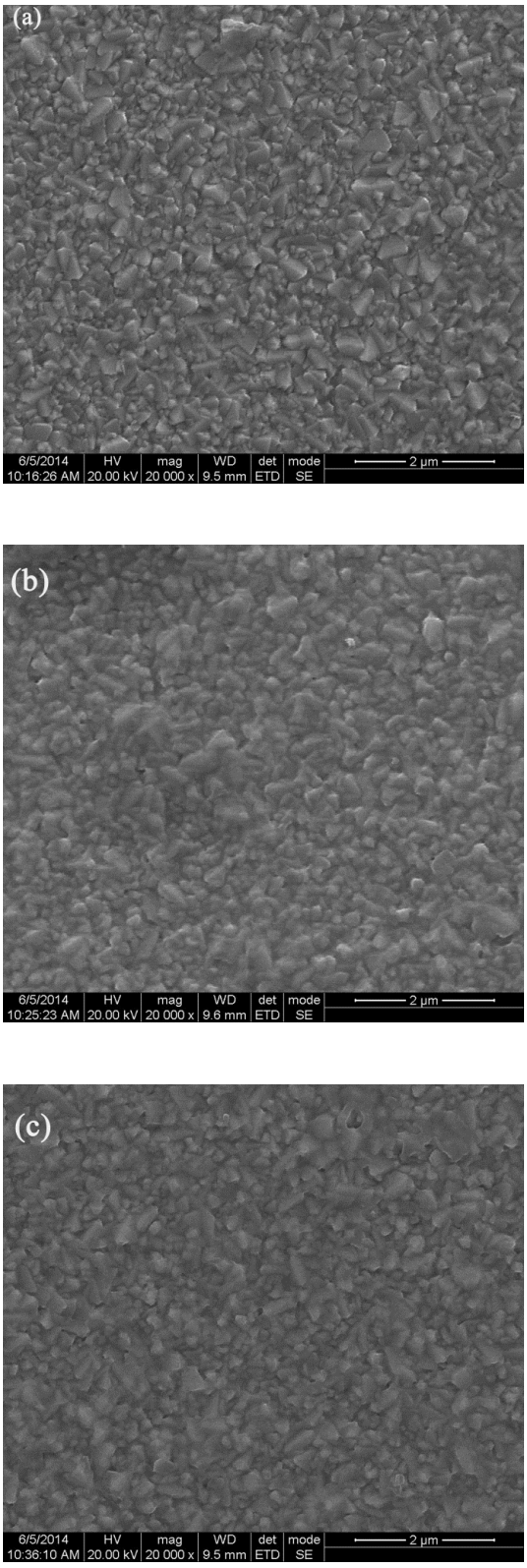

Figure 6.5. SEM images of (a) $(PAM\text{-}ZnO/PSS\text{-}rGO)_3$, (b) $(PAM\text{-}ZnO/PSS\text{-}rGO)_5$, (c) $(PAM\text{-}ZnO/PSS\text{-}rGO)_9$ on FTO substrate

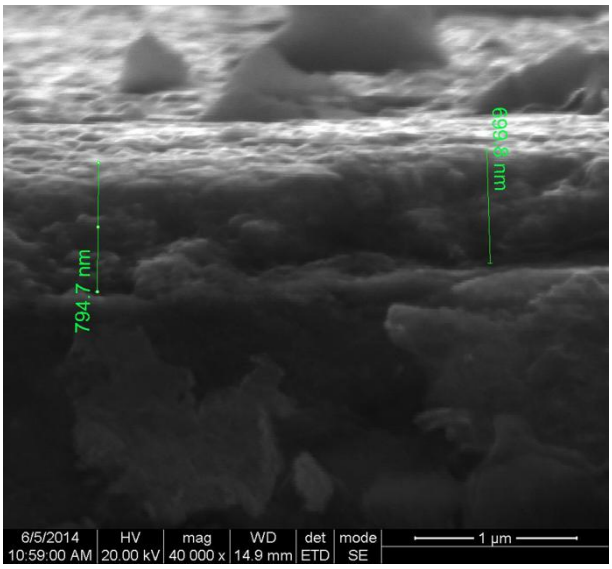

Figure 6.6. Cross-sectional SEM image of $(PAM\text{-}ZnO/PSS\text{-}rGO)_9$ on FTO substrate

6.3.3. Visible light photoconductivity of multilayer films

Multilayer films coated on FTO substrate is used as the working electrode for the measurement of photoconductivity and electrochemical impedance spectra. Fig. 6.7 shows the photocurrent measured for $(PAM\text{-}ZnO/PSS\text{-}G)_5$ and $(PAM\text{-}ZnO/PSS\text{-}G)_9$ as function of time at –0.5 V bias voltage with light on and off cycles in an interval of 60 s. The value of dark current, photocurrent and on-off difference are summarised in Table 6.1. For a comparison, photoresponse of rGO/ZnO prepared by hydrothermal method is also given in Table 6.1. On comparing multilayer film $(PAM\text{-}ZnO/PSS\text{-}rGO)_9$ with h-ZnO and PSS-rGO, the multilayer film has considerable improvement in dark conductivity and photoconductivity. But for $(PAM\text{-}ZnO/PSS\text{-}rGO)_3$, the dark as well as photo current response is low, may be due to the low loading of ZnO and rGO. With the increase in the number of bilayers, the on-off difference is increasing for the multilayer films.

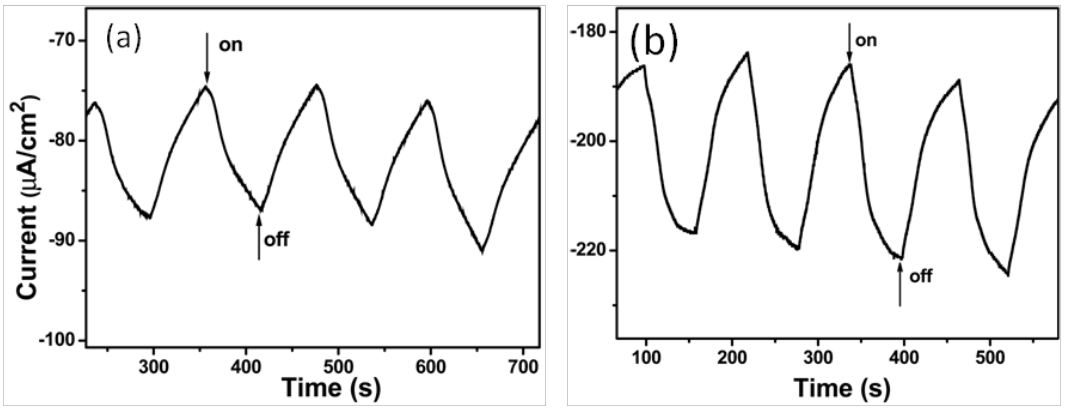

Figure 6.7. Photocurrent measurement of (a) $(PAM\text{-}ZnO/PSS\text{-}rGO)_5$ (b) $(PAM\text{-}ZnO/PSS\text{-}rGO)_9$ at bias voltage of –0.5 V

In order to find out the mechanism of improvement in conductivity for the self assembled multilayers, electrochemical impedance spectra is analysed. Fig. 6.8 shows Nyquist plot corresponding to the impedance measurement. Usually Nyquist plot consist of several semicircles, in which first semicircle is assigned to the charge transfer resistance and others arise from the capacitance at the bulk electrolyte interface (Patel, et al., 2014). For all the samples, Nyquist plot consist of only first semicircle. The smaller the radius of this semicircle, the better the charge transfer resistance (Hou, et al., 2013). For rGO/ZnO prepared by *in-situ* method (hydrothermal method), the carrier transfer resistance is very high. This electrode is prepared by continuously coating nine layers of rGO/ZnO dispersed in PAM. Here the electron transfer efficiency may be reduced due to insulating character of the polymer. For the rGO/ZnO multilayers, as the number of bilayers is increased, the radius of semicircle decreases indicating that the charge transfer resistance is gradually reducing. In other words, this indicates faster interfacial charge transfer between the ZnO and rGO within the bilayers and between the bilayers. The multilayer films fabricated by LBL technique will be highly interpenetrating; it will enhance the interaction between the ZnO and rGO perpendicular to the electrode surface. For PSS-rGO, the radius of the arc is comparable with five bilayers and it is also reflected in the dark conductivity of this sample. Excellent conductivity of PSS-rGO is due to the sufficiently good reduction of graphene oxide in PSS

Table 6.1. Dark current, photocurrent and on-off difference of samples

Sample	Dark current ($\mu A/cm^2$)	Photocurrent ($\mu A/cm^2$)	On-off Difference ($\mu A/cm^2$)
$(PAM\text{-}ZnO/PSS\text{-}rGO)_3$	-25.52	-27.19	1.67
$(PAM\text{-}ZnO/PSS\text{-}rGO)_5$	-75.16	-87.2	12.36
$(PAM\text{-}ZnO/PSS\text{-}rGO)_7$	-73.96	-92.04	18.08
$(PAM\text{-}ZnO/PSS\text{-}rGO)_9$	-185.36	-219.16	33.80
rGO/ZnO (hydrothermal)	-49.04	-54.36	5.32
PSS-rGO	-77.08	-83.096	6.92
h-ZnO	-35.72	-45.72	10

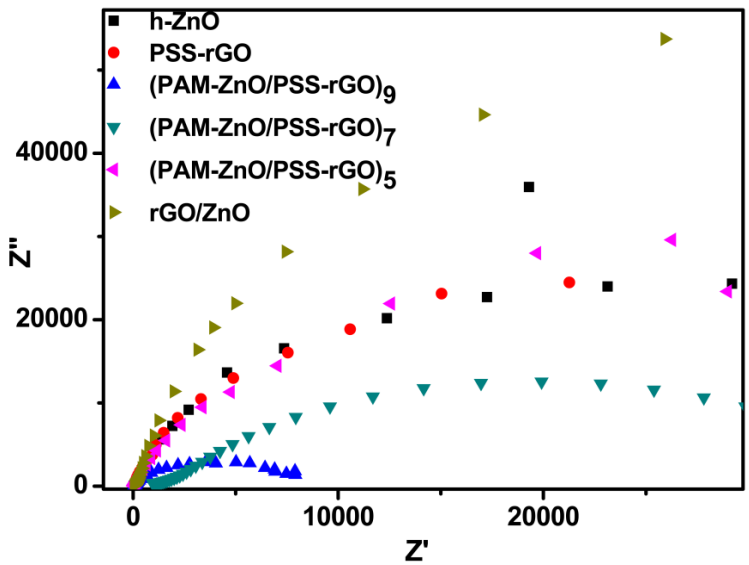

Figure 6.8. Nyquist plot of impedance data of ZnO, rGO/ZnO, PSS-rGO and the multilayers films

The photoconductivity (on-off difference) of the multilayer films is increasing with the increase in the number of bilayers. When the multilayer films are irradiated with light, both ZnO and graphene can assist the absorption of light.

It is clear from the table 6.1 that the photoresponse of PSS-rGO is low, though it has excellent dark conductivity. This is due to the poor optical absorption of graphene (Zhang, et al., 2013). The oxygen vacancy states are responsible for the below bandgap absorption and conductivity in h-ZnO and hence higher photocurrent in h-ZnO (Kavitha, et al., 2014a).

Taking into account the photoresponse and charge transfer resistance of multilayer films, mechanism for the photoconductivity is proposed. During the photocurrent measurement, when the film is irradiated with light, a defect assisted excitation occurs in ZnO. The excited electrons in ZnO can easily transfer to graphene sheets, since the work function of graphene is lower than that of the conduction band of ZnO. This will result in an efficient charge separation and prolonged recombination time for the electron-hole pairs (Guo, et al., 2013). The electron transferred to graphene sheets can recombine in two ways; either it can recombine with the holes in the valence band of ZnO in its bilayer or the ZnO in the next bilayer. This type of tunnelling of electrons from graphene to the successive bilayers will result in efficient charge transfer. This transfer and propagation of electron will enhance as the number of bilayers increases which in turn improve the photocurrent of the multilayer films. Fig. 6.9 shows the energy band diagram of representative multilayer film and possible mode of electron transfer in two bilayers are presented. The excellent conductivity of this self assembled films indicate its scope as a transparent electrode as well as photoanode in solar cells.

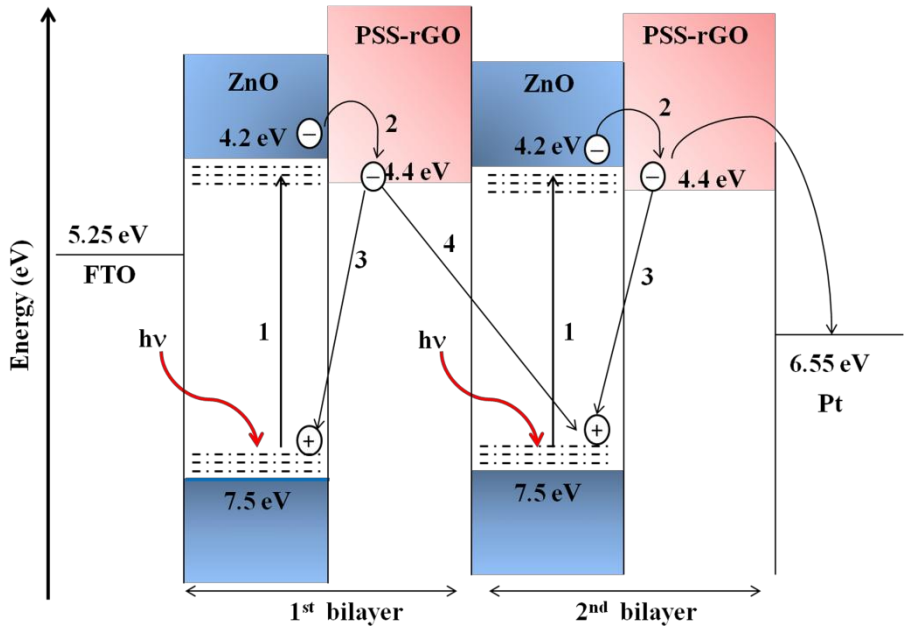

Figure 6.9. Schematic diagram of the energy band of multilayer films with two bilayers, when a bias of –0.5 V is applied across the film and illuminated with light. The possible modes of electron transfer are numbered as (1) defect assisted excitation in ZnO (2). Electron transfer to the graphene (3) recombination with the hole of ZnO in the same bilayer (4) recombination with the hole of ZnO in the next bilayer

6.3.4. Nonlinear absorption of multilayer films

Nonlinear absorption of multilayer films coated on FTO substrate is investigated using open aperture Z-scan technique. Fig. 6.10 shows the open aperture Z-scan curve of lowest bilayer $(PAM\text{-}ZnO/PSS\text{-}rGO)_3$ and highest bilayer $PAM\text{-}ZnO/PSS\text{-}rGO)_9$ under study at input laser pulse energy of 25 μJ. Nonlinear absorption curve of $(PAM\text{-}ZnO/PSS\text{-}rGO)_3$ has the configuration of two peak on either side of the focus and a valley at the focus (Fig. 6.10a). This indicates that three bilayer films show saturable absorption (SA) at lower input intensity (away from focus) and reverse saturable absorption (RSA) at higher input intensity (in the focus). RSA occurs when excited state absorption cross section of the material is larger than the ground state absorption cross section at the input wavelength. RSA indicate positive absorption which can occur either by excited state absorption (ESA) or two-photon absorption process. In contrast, for SA, the absorption of the material decreases with input intensity due to the large

ground state absorption cross section. This switching of nonlinear absorption in $(PAM\text{-}ZnO/PSS\text{-}rGO)_3$ can be demonstrated as follows. When the film is far away from the focus, the input intensity is too low to induce nonlinearity and the transmittance is unity. When the film is moved further near to the focus, intensity of light falling on the sample is increased and the ground state gets depleted causing saturable absorption, so that the transmittance increases. On the other hand as the film reaches the focus, still higher intensities are seen by the film and RSA dominates, causing strong optical limiting. Hence transmittance decreases effectively and falls to a value less than unity. But for $(PAM\text{-}ZnO/PSS\text{-}rGO)_9$, the film exhibits a clear increase in transmittance with increase in input laser intensity showing SA (Fig. 6.10b).

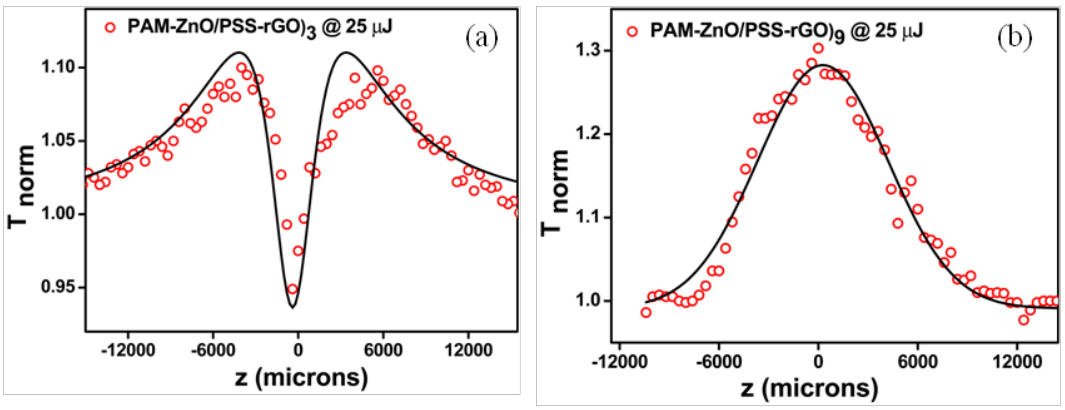

Figure 6.10 Open aperture Z-scan curve of (a) $(PAM\text{-}ZnO/PSS\text{-}rGO)_3$ (b) $(PAM\text{-}ZnO/PSS\text{-}rGO)_9$ at input energy of 25 μJ. Symbols denote experimental results while solid curves are fits to the data.

In order to understand the nature of nonlinear absorption of multilayer films, Z-scan measurement is done at a lower input energy of 5 μJ and it is shown in Fig. 6.11. At lower input energy, the three bilayer film exhibit a peak at the focus indicating SA plays a dominant role in the nonlinear absorption. In contrast, nine bilayer shows saturable absorption behaviour even at lower input energy. In short, $(PAM\text{-}ZnO/PSS\text{-}rGO)_3$ shows a switching from SA to RSA as the input energy increases while $(PAM\text{-}ZnO/PSS\text{-}rGO)_9$ shows SA in all the input energies.

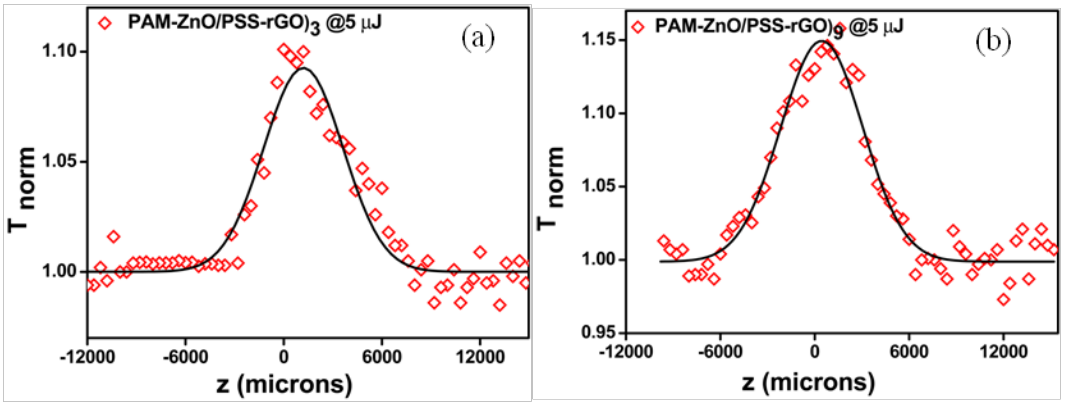

Figure 6.11. Open aperture Z-scan curve of (a) $(PAM\text{-}ZnO/PSS\text{-}rGO)_3$ (b) $(PAM\text{-}ZnO/PSS\text{-}rGO)_9$ at input energy of 5 μJ. Symbols denote experimental results while solid curves are fits to the data.

6.4. Conclusions

The multilayer films containing ZnO and PSS-rGO is constructed by layer-by-layer self assembly technique. The electrostatic force of attraction between the polyelectrolytes facilitates the efficient interaction between ZnO and rGO. The UV-vis absorption spectra show that the absorbance at 360 nm and 270 nm of the films are increasing linearly with the number of bilayers indicating the uniform growth of multilayers by this technique. This layer-by-layer self assembled rGO/ZnO films are used for visible light photocurrent generation and nonlinear absorption. The photoconductivity of the multilayer films is increasing with increase in number of bilayers. The improvement in photocurrent may be due to the efficient charge separation and prolonged recombination time for the electron-hole pairs in ZnO/rGO. Open aperture Z-scan measurements show that, three bilayer films have increased transmittance at lower input intensity. With the increase in input intensity, it shows optical limiting behaviour. However, for nine bilayer films the absorption saturates quickly due to ground state depletion.

CHAPTER 7
SUMMARY AND CONCLUSIONS

ZnO and ZnO/graphene hybrids have promising future in variety of optoelectronic applications including photoconductivity and nonlinear absorption. However, there are still many challenges to overcome before these systems are used to fabricate high performance devices. Better understanding of the nature of defects in ZnO and ZnO/graphene is essential to modify its conductivity and absorption. The major outcome of the thesis are (1) Synthesis of ZnO nanocones and its influence on below bandgap photoconductivity and nonlinear absorption, (2) Synthesis of rGO/ZnO and study the modification of defects in ZnO during its growth on reduced graphene oxide sheets and (3) Fabrication of ZnO/graphene films by layer-by-layer self assembly technique is proposed to reduce the interfacial carrier transfer resistance and thereby modifying its photoconductivity and nonlinear absorption.

Chapter 1 gives an overview about ZnO and ZnO/graphene hybrids. The nature of defects and how it modifies the optical properties of ZnO is discussed in detail. The theory of photoconductivity and nonlinear absorption is also described. The general features of graphene and the importance of ZnO/graphene hybrids are also detailed. The theoretical background of characterization techniques and experimental set up for photoconductivity and nonlinear absorption are explained in chapter 2.

Chapter 3 is dedicated to the synthesis of ZnO with cone shape morphology by solution precipitation and hydrothermal method. In ZnO nanocones base will be hexagonal polar $(000\bar{1})$ facet and the six sides will be the high energy polar $(10\bar{1}1)$ planes. By the detailed evaluation of reaction conditions the growth mechanism of ZnO nanocones is revealed. The capping agent, PVP has a significant role in the crystallization of ZnO in solution method. The length to width ratio of the nanocones depends on the pH of the reaction medium. At

lower pH distorted hexagonal plates are formed. The cones are formed by the stacking of these hexagonal plates along the direction of c-axis. Depending on the concentration of OH^- ions, elongated, shortened and quasi-spherical ZnO nanoparticles can grow. We have adjusted the pH in such a way that shortened nanocones will form during the precipitation. In this morphology, the most exposed facets are oxygen terminated. Therefore, the dominant defect states may be oxygen vacancies. These defect states play an important role in the below band gap photoresponse of ZnO, and it can be utilised for tailoring the optoelectronic properties.

By the careful examination of photoluminescence spectra and time correlated single photon counting experiment the defect states in ZnO nancones are identified. Chapter 4 describes how the photoconductivity and nonlinear absorption is modified with respect to the alteration of these defect states. The as-grown ZnO nanocones have a green emission centred at 2.25 eV and a blue emission at 2.69 eV, in addition to the band edge emission at 3.27 eV. After calcination of the sample, the green emission is suppressed while the blue emission is enhanced. By probing the carrier life time of these two emissions before and after calcination, we have identified that green emission is due to oxygen vacancy states while blue emission by zinc vacancies. The oxygen vacancies create donor-like levels within the bandgap, corresponding to singly ($V_O^{\cdot}$) and doubly ionised ($V_O^{\cdot\cdot}$) oxygen vacancies below the bandgap. The low energy green emission is due to the capture of holes by $V_O^{\cdot}$ to generate $V_O^{\cdot\cdot}$, leading to an emission with a peak at 2.25 eV. These surface oxygen vacancies can get compensated upon calcination in air, resulting in the quenching of green emission. The blue emission at 2.69 eV is attributed to the transition between the conduction band and the zinc vacancy acceptor level. After calcination the blue emission is enhanced and hence zinc vacancies are one of the dominant defects in oxygen rich conditions.

ZnO nanocones exhibits dark conductivity and its conductivity is increased upon illumination with white light. When this ZnO is calcined in air,

the dark conductivity as well as the photoconductivity gets decreased, indicating the reduction in donor level density, especially the surface oxygen vacancies. The oxygen vacancies in the material can induce occupied states near to the valence band, which can mediate the visible light excitation in ZnO. This will generate charge carriers, resulting in increased photocurrent. After calcination density of oxygen vacancy states decreases, which in turn reduces visible light absorption and photocurrent generation. ZnO nanocones exhibit significant improvement in effective two photon absorption upon calcination, suggesting the nonlinearity originates from the sub-band states created by the zinc vacancies. In summary, oxygen vacancies have a critical role in visible light photoconductivity, while zinc vacancy states are crucial in nonlinear absorption.

The combination of ZnO and graphene is identified as good candidate for optoelectronic applications. The 2D graphene can support the nanoparticles and it can also store and shuttle the photogenrated electrons from ZnO upon excitation. Chapter 5 describes solution method and hydrothermal method to grow ZnO nanoaparticles on reduced graphene oxide (rGO). Graphene oxide (GO) is used as the precursor for rGO. During the crystallization of ZnO, GO will undergo reduction in alkaline medium and it is further reduced by hydrothermal treatment. Structural analysis reveals that hydrothermal method provides highly reduced graphene oxide decorated with ZnO. Photoluminescence and carrier life time experiments demonstrate the interaction and electron transfer between ZnO and graphene layers. During the reduction of GO in presence of ZnO, there is diffusion of oxygen from GO to ZnO, this will compensate the oxygen vacancies on the surface of ZnO. The dark conductivity of rGO/ZnO is improved while its visible light photoconductivity is depleted compared to pure ZnO. rGO/ZnO exhibits good nonlinear absorption compared to ZnO and GO. This suggests the effective two photon absorption process with photoinduced electron transfer between ZnO and graphene.

Chapter 6 detailed the electrostatic layer-by-layer self assembly technique to fabricate rGO/ZnO multilayer films. The multilayer films are

fabricated by ZnO nancones dispersed in polyacrylamide (PAM) and rGO grafted and dispersed with poly (sodium 4-styrene sulfonate) (PSS-rGO). The visible light photoconductivity of these films is improved compared to ZnO and rGO. Based on the photoresponse and carrier resistance measurement, it can be concluded that there is an efficient charge separation and prolonged recombination time for the electron-hole pairs in ZnO/rGO multilayer films. Nonlinear absorption of these films shows an interesting behaviour. Three bilayer films have increased transmittance at lower input energy. With the increase in input intensity it shows optical limiting behaviour. But for nine bilayer films the absorption saturates quickly due to the fast ground state depletion by the electron transfer to graphene layers.

Conclusions

ZnO with cone shaped structures are synthesized by wet chemical method. These ZnO nanostructures posses oxygen and zinc vacancies, these defect states provides good dark conductivity for ZnO. Oxygen vacancies play a key role in visible light photoconductivity and zinc vacancies are crucial in nonlinear absorption. When rGO/ZnO is prepared by chemical method, there is repairing of oxygen vacancies in ZnO which deplete its photocurrent. But the nonlinear absorption and optical limiting property of rGO/ZnO is enhanced. The rGO/ZnO multilayer films are prepared by layer-by layer self assembly technique. These films exhibit low carrier transfer resistance in turn results in good dark and light conductivity. The nonlinear absorption of these films varies from saturable absorption to optical limiting with respect to pump intensity and number of bilayers.

Possible future applications

ZnO is a well known UV absorber, here the defect states in ZnO nancones assist below bandgap photoconductivity. ZnO nanocones have large oxygen vacancies creating two sub-band states, this will assist the below band gap absorption, which indicate the scope of this nanostructure as a visible light photodetector. ZnO possesses excellent dark conductivity due to the defects pave

way to fabricate transparent conducting coatings. In this study rGO/ZnO dispersions is identified as good optical limiter. rGO/ZnO also exhibit dark conductivity, which can be used for the thin film transistors, photovoltaics, etc. Layer-by-layer assembly is a good and economical approach to fabricate rGO/ZnO films from solution. It can be coated on any substrate with superior interaction between ZnO and graphene, which suggest its scope for this method for the fabrication of an optoelectronic device especially for the fabrication of photoelectrode due its excellent conductivity.

REFERENCES

1. Abhinandan, M., Soumik, S., Tanujjal, B., Sunandan, B., Joydeep, D., Raychaudhuri, A. K. and Samir Kumar, P. (2010). Dynamics of light harvesting in ZnO nanoparticles. *Nanotechnology*, 21(26): 265703.

2. Acik, M., Lee, G., Mattevi, C., Pirkle, A., Wallace, R. M., Chhowalla, M., Cho, K. and Chabal, Y. (2011). The Role of Oxygen during Thermal Reduction of Graphene Oxide Studied by Infrared Absorption Spectroscopy. *Journal of Physical Chemistry C*, 115(40): 19761-19781.

3. Ahn, K. S., Shet, S., Deutsch, T., Jiang, C. S., Yan, Y., Al-Jassim, M. and Turner, J. (2008). Enhancement of photoelectrochemical response by aligned nanorods in ZnO thin films. *Journal of Power Sources*, 176(1): 387-392.

4. Akhavan, O., Mehrabian, M., Mirabbaszadeh, K. and Azimirad, R. (2009). Hydrothermal synthesis of ZnO nanorod arrays for photocatalytic inactivation of bacteria. *Journal of Physics D: Applied Physics*, 42(22): 225305.

5. Alenezi, M. R., Alshammari, A. S., Jayawardena, K. D. G. I., Beliatis, M. J., Henley, S. J. and Silva, S. R. P. (2013). Role of the exposed polar facets in the performance of thermally and UV activated ZnO nanostructured gas sensors. *Journal of Physical Chemistry C*, 117(34): 17850-17858.

6. Anand, B., Krishnan, S. R., Podila, R., Siva Sankara Sai, S., Rao, A. M. and Philip, R. (2014). The role of defects in the nonlinear optical absorption behavior of carbon and ZnO nanostructures. *Physical Chemistry Chemical Physics*, 16(18): 8168-8177.

7. Aneeshkumar, B., Gopinath, P., Vallabhan, C. P. G., Nampoori, V. P. N., Radhakrishnan, P. and Thomas, J. (2003). Optical-limiting response of rare-earth metallo-phthalocyanine-doped copolymer matrix. *Journal of the Optical Society of America B*, 20(7): 1486-1490.

8. Appavoo, K., Liu, M. and Sfeir, M. Y. (2014). Role of size and defects in ultrafast broadband emission dynamics of ZnO nanostructures. *Applied Physics Letters*, 104(13): 133101.

9. Ashfold, M. N. R., Doherty, R. P., Ndifor-Angwafor, N. G., Riley, D. J. and Sun, Y. (2007). The kinetics of the hydrothermal growth of ZnO nanostructures. *Thin Solid Films*, 515(24): 8679-8683.

10. Bae, S., Kim, H., Lee, Y., Xu, X., Park, J. S., Zheng, Y., Balakrishnan, J., Lei, T., Ri Kim, H., Song, Y. I., Kim, Y. J., Kim, K. S., Ozyilmaz, B., Ahn, J. H., Hong, B. H. and Iijima, S. (2010). Roll-to-roll production of 30-inch graphene films for transparent electrodes. *Nature Nanotechnology*, 5(8): 574-578.

11. Bai, X., Wang, L., Zong, R., Lv, Y., Sun, Y. and Zhu, Y. (2013). Performance Enhancement of ZnO Photocatalyst via Synergic Effect of Surface Oxygen Defect and Graphene Hybridization. *Langmuir*, 29(9): 3097-3105.

12. Balandin, A. A., Ghosh, S., Bao, W., Calizo, I., Teweldebrhan, D., Miao, F. and Lau, C. N. (2008). Superior Thermal Conductivity of Single-Layer Graphene. *Nano Letters*, 8(3): 902-907.

13. Bang, S., Lee, S., Ko, Y., Park, J., Shin, S., Seo, H. and Jeon, H. (2012). Photocurrent detection of chemically tuned hierarchical ZnO nanostructures grown on seed layers formed by atomic layer deposition. *Nanoscale Research Letters*, 7(1): 1-11.

14. Bao, Q. and Loh, K. P. (2012). Graphene Photonics, Plasmonics, and Broadband Optoelectronic Devices. *ACS Nano*, 6(5): 3677-3694.

15. Bao, Q., Zhang, H., Wang, Y., Ni, Z., Yan, Y., Shen, Z. X., Loh, K. P. and Tang, D. Y. (2009). Atomic-Layer Graphene as a Saturable Absorber for Ultrafast Pulsed Lasers. *Advanced Functional Materials*, 19(19): 3077-3083.

16. Bilecka, I., Elser, P. and Niederberger, M. (2009). Kinetic and Thermodynamic Aspects in the Microwave-Assisted Synthesis of ZnO Nanoparticles in Benzyl Alcohol. *ACS Nano*, 3(2): 467-477.

17. Bitenc, M., Podbršček, P., Crnjak Orel, Z., Cleveland, M. A., Paramo, J. A., Peters, R. M. and Strzhemechny, Y. M. (2009). Correlation between Morphology and Defect Luminescence in Precipitated ZnO Nanorod Powders. *Crystal Growth & Design*, 9(2): 997-1001.

18. Bonnett, R. and Martinez, G. (2000). Photobleaching studies on azabenzoporphyrins and related systems: a comparison of the photobleaching of the zinc(II) complexes of the tetrabenzoporphyrin, 5-azadibenzo[b,g]porphyrin and phthalocyanine systems. *Journal of Porphyrins and Phthalocyanines*, 04(05): 544-550.

19. Boppella, R., Anjaneyulu, K., Basak, P. and Manorama, S. V. (2013). Facile Synthesis of Face Oriented ZnO Crystals: Tunable Polar Facets and Shape Induced Enhanced Photocatalytic Performance. *Journal of Physical Chemistry C*, 117(9): 4597-4605.

20. Bottom, R. (2008) Thermogravimetric analysis. In P. Gabbott (Eds.),. *Principles and Applications of Thermal Analysis* (pp 87-118). Wiley-Blackwell: US.

21. Brodie, B. C. (1859). On the Atomic Weight of Graphite. *Royal Society of London Philosophical Transactions Series I*, 149: 249-259.

22. Carrey, J., Carrère, H., Kahn, M. L., Chaudret, B., Marie, X. and Respaud, M. (2008). Photoconductivity of self-assembled ZnO nanoparticles synthesized by organometallic chemistry. *Semiconductor Science and Technology*, 23(2): 025003.

23. Catheline, A., Ortolani, L., Morandi, V., Melle-Franco, M., Drummond, C., Zakri, C. and Penicaud, A. (2012). Solutions of fully exfoliated individual graphene flakes in low boiling point solvents. *Soft Matter*, 8(30): 7882-7887.

24. Chang, J., Ahmed, R., Wang, H., Liu, H., Li, R., Wang, P. and Waclawik, E. R. (2013). ZnO Nanocones with High-Index $(10\bar{1}1)$, Facets for Enhanced Energy Conversion Efficiency of Dye-Sensitized Solar Cells. *Journal of Physical Chemistry C*, 117(27): 13836-13844.

25. Chang, J. and Waclawik, E. R. (2012). Facet-controlled self-assembly of ZnO nanocrystals by non-hydrolytic aminolysis and their photodegradation activities. *CrystEngComm*, 14(11): 4041-4048.

26. Chen, L., Xu, Z., Li, J., Li, Y., Shan, M., Wang, C., Wang, Z., Guo, Q., Liu, L., Chen, G. and Qian, X. (2012). A facile strategy to prepare functionalized graphene via intercalation, grafting and self-exfoliation of graphite oxide. *Journal of Materials Chemistry*, 22(27): 13460-13463.

27. Chen, M. W., Chen, C. Y., Lien, D. H., Ding, Y. and He, J. H. (2010). Photoconductive enhancement of single ZnO nanowire through localized Schottky effects. *Optics Express*, 18(14): 14836-14841.

28. Chen, S. L., Stehr, J., Reddy, N. K., Tu, C. W., Chen, W. M. and Buyanova, I. A. (2012). Efficient upconversion of photoluminescence via two-photon absorption in bulk and nanorod ZnO. *Applied Physics B*, 108(4): 919-924.

29. Cheng, A. J., Tzeng, Y., Zhou, Y., Park, M., Wu, T. H., Shannon, C., Wang, D. and Lee, W. (2008). Thermal chemical vapor deposition growth of zinc oxide nanostructures for dye-sensitized solar cell fabrication. *Applied Physics Letters*, 92(9): 092113.

30. Chirea, M., García-Morales, V., Manzanares, J. A., Pereira, C., Gulaboski, R. and Silva, F. (2005). Electrochemical Characterization of Polyelectrolyte/Gold Nanoparticle Multilayers Self-Assembled on Gold

Electrodes. *The Journal of Physical Chemistry B*, 109(46): 21808-21817.

31. Compton, O. C., Cranford, S. W., Putz, K. W., An, Z., Brinson, L. C., Buehler, M. J. and Nguyen, S. T. (2011). Tuning the Mechanical Properties of Graphene Oxide Paper and Its Associated Polymer Nanocomposites by Controlling Cooperative Intersheet Hydrogen Bonding. *ACS Nano*, 6(3): 2008-2019.

32. Dakhlaoui, A., Jendoubi, M., Smiri, L. S., Kanaev, A. and Jouini, N. (2009). Synthesis, characterization and optical properties of ZnO nanoparticles with controlled size and morphology. *Journal of Crystal Growth*, 311(16): 3989-3996.

33. Decher, G., Hong, J. D. and Schmitt, J. (1992). Buildup of ultrathin multilayer films by a self-assembly process: III. Consecutively alternating adsorption of anionic and cationic polyelectrolytes on charged surfaces. *Thin Solid Films*, 210–211, Part 2(0): 831-835.

34. Dubin, S., Gilje, S., Wang, K., Tung, V. C., Cha, K., Hall, A. S., Farrar, J., Varshneya, R., Yang, Y. and Kaner, R. B. (2010). A One-Step, Solvothermal Reduction Method for Producing Reduced Graphene Oxide Dispersions in Organic Solvents. *ACS Nano*, 4(7): 3845-3852.

35. Eita, M., Usman, A., El-Ballouli, A. a. O., Alarousu, E., Bakr, O. M. and Mohammed, O. F. (2014). A Layer-by-Layer ZnO Nanoparticle–PbS Quantum Dot Self-Assembly Platform for Ultrafast Interfacial Electron Injection. *Small*, doi: 10.1002/smll.201400939.

36. Ellmer, K., Klein, A. and Rech, B. (2007).*Transparent Conductive Zinc Oxide: Basics and Applications in Thin Film Solar Cells*. Springer: London.

37. Erhart, P., Albe, K. and Klein, A. (2006). First-principles study of intrinsic point defects in ZnO: Role of band structure, volume relaxation, and finite-size effects. *Physical Review B*, 73(20): 205203.

38. Eswaraiah, V., Jyothirmayee Aravind, S. S. and Ramaprabhu, S. (2011). Top down method for synthesis of highly conducting graphene by exfoliation of graphite oxide using focused solar radiation. *Journal of Materials Chemistry*, 21(19): 6800-6803.

39. Fan, X., Peng, W., Li, Y., Li, X., Wang, S., Zhang, G. and Zhang, F. (2008). Deoxygenation of Exfoliated Graphite Oxide under Alkaline Conditions: A Green Route to Graphene Preparation. *Advanced Materials*, 20(23): 4490-4493.

40. Feng, X. and Ji, W. (2009). Shape-dependent two-photon absorption in semiconductor nanocrystals. *Optics Express*, 17(15): 13140-13150.

41. Feng, Y., Zhang, M., Guo, M. and Wang, X. (2010). Studies on the PEG-Assisted Hydrothermal Synthesis and Growth Mechanism of ZnO Microrod and Mesoporous Microsphere Arrays on the Substrate. *Crystal Growth & Design*, 10(4): 1500-1507.

42. Ferrari, A. C. (2007). Raman spectroscopy of graphene and graphite: Disorder, electron–phonon coupling, doping and nonadiabatic effects. *Solid State Communications*, 143(1–2): 47-57.

43. Foreman, J. V., Li, J., Peng, H., Choi, S., Everitt, H. O. and Liu, J. (2006). Time-Resolved Investigation of Bright Visible Wavelength Luminescence from Sulfur-Doped ZnO Nanowires and Micropowders. *Nano Letters*, 6(6): 1126-1130.

44. Gan, X., Shiue, R. J., Gao, Y., Mak, K. F., Yao, X., Li, L., Szep, A., Walker, D., Hone, J., Heinz, T. F. and Englund, D. (2013). High-Contrast Electrooptic Modulation of a Photonic Crystal Nanocavity by Electrical Gating of Graphene. *Nano Letters*, 13(2): 691-696.

45. Ganguly, A., Sharma, S., Papakonstantinou, P. and Hamilton, J. (2011). Probing the Thermal Deoxygenation of Graphene Oxide Using High-Resolution In Situ X-ray-Based Spectroscopies. *Journal of Physical Chemistry C*, 115(34): 17009-17019.

46. García-Gutiérrez, R., Barboza-Flores, M., Berman-Mendoza, D., Rangel-Segura, R. and Contreras-López, O. E. (2012). Luminescence and Structure of ZnO Grown by Physical Vapor Deposition. *Advances in Materials Science and Engineering*, 2012: 872597.

47. Geim, A. K. and Novoselov, K. S. (2007). The rise of graphene. *Nature Materials*, 6(3): 183-191.

48. Georgekutty, R., Seery, M. K. and Pillai, S. C. (2008). A Highly Efficient Ag-ZnO Photocatalyst: Synthesis, Properties, and Mechanism. *Journal of Physical Chemistry C*, 112(35): 13563-13570.

49. Ghosh, S., Sarker, B. K., Chunder, A., Zhai, L. and Khondaker, S. I. (2010). Position dependent photodetector from large area reduced graphene oxide thin films. *Applied Physics Letters*, 96(16): 163109.

50. Ghoshal, T., Kar, S., Ghatak, J. and Chaudhuri, S. ZnO nanocones: Solvothermal synthesis and photoluminescence properties. (2008). *Materials Research Bulletin*, 43(8–9): 2228-2238.

51. Gimenez, A. J., Yáñez-Limón, J. M. and Seminario, J. M. (2010). ZnO−Paper Based Photoconductive UV Sensor. *Journal of Physical Chemistry C*, 115(1): 282-287.

52. Goldstein, J., Newbury, D.E., Joy, D.C., Lyman, C.E., Echlin, P., Lifshin, E., Sawyer, L., Michael, J.R. (2003) *Scanning Electron Microscopy and X-ray Microanalysis.* (3rd ed.) Springer: US.

53. Gong, Y., Andelman, T., Neumark, G., O'Brien, S. and Kuskovsky, I. (2007). Origin of defect-related green emission from ZnO nanoparticles: effect of surface modification. *Nanoscale Research Letters*, 2(6): 297-302.

54. Gu, H., Yang, Y., Tian, J. and Shi, G. (2013). Photochemical Synthesis of Noble Metal (Ag, Pd, Au, Pt) on Graphene/ZnO Multihybrid Nanoarchitectures as Electrocatalysis for H2O2 Reduction. *ACS Applied Materials & Interfaces*, 5(14): 6762-6768.

55. Gu, P., Wang, X., Li, T., Meng, H., Yu, H. and Fan, Z. (2012). Synthesis, characterization and photoluminescence of ZnO spindles by polyvinylpyrrolidone-assisted low-temperature wet-chemistry process. *Journal of Crystal Growth*, 338(1): 162-165.

56. Guermeur, C., Sanchez, C., Schaudel, B., Nakatani, K., Delaire, J. A., del Monte, F. and Levy, D. (1997). Dye-matrix interactions in sol-gel-derived hybrid organic-inorganic nanocomposites, In *Proc. SPIE 3136, Sol-Gel Optics IV*, 1997 pp 10-19.

57. Guo, L., Zhang, H., Zhao, D., Li, B., Zhang, Z., Jiang, M. and Shen, D. (2012). High responsivity ZnO nanowires based UV detector fabricated by the dielectrophoresis method. *Sensors and Actuators B: Chemical*, 166–167(0): 12-16.

58. Guo, W., Xu, S., Wu, Z., Wang, N., Loy, M. M. T. and Du, S. (2013). Oxygen-Assisted Charge Transfer Between ZnO Quantum Dots and Graphene. *Small*, 9(18): 3031-3036.

59. Hani, K., Guangyu, C., Oleg, L., Helge, H., Sanghoon, P., Alfons, S. and Lee, C. (2009). Investigation of chemical bath deposition of ZnO thin films using six different complexing agents. *Journal of Physics D: Applied Physics*, 42(13): 135304.

60. Hayashi, H., Lightcap, I. V., Tsujimoto, M., Takano, M., Umeyama, T., Kamat, P. V. and Imahori, H. (2011). Electron Transfer Cascade by Organic/Inorganic Ternary Composites of Porphyrin, Zinc Oxide Nanoparticles, and Reduced Graphene Oxide on a Tin Oxide Electrode that Exhibits Efficient Photocurrent Generation. *Journal of the American Chemical Society*, 133(20): 7684-7687.

61. Henini, M. (2012).*Molecular Beam Epitaxy: From Research to Mass Production*. Elsevier Science.

62. Hou, Y., Wu, T., Wang, L. and Feng, P. (2013). Integration of supertetrahedral cluster with reduced graphene oxide sheets for enhanced photostability and photoelectrochemical properties. *Science China Chemistry*, 56(4): 423-427.

63. Hummers, W. S. and Offeman, R. E. (1958). Preparation of Graphitic Oxide. *Journal of the American Chemical Society*, 80(6): 1339-1339.

64. Iler, R. K. (1966). Multilayers of colloidal particles. *Journal of Colloid and Interface Science*, 21(6): 569-594.

65. Ischenko, V., Polarz, S., Grote, D., Stavarache, V., Fink, K. and Driess, M. (2005). Zinc Oxide Nanoparticles with Defects. *Advanced Functional Materials*, 15(12): 1945-1954.

66. Janotti, A. and Van de Walle, C. G. (2007). Native point defects in ZnO. *Physical Review B*, 76(16): 165202.

67. Jia, W., Douglas, E. P., Guo, F. and Sun, W. (2004). Optical limiting of semiconductor nanoparticles for nanosecond laser pulses. *Applied Physics Letters*, 85(26): 6326-6328.

68. Jia, Y., Yu, X. Y., Luo, T., Zhang, M. Y., Liu, J. H. and Huang, X. J. (2013). PEG aggregation templated porous ZnO nanostructure: room temperature solution synthesis, pore formation mechanism, and their photoluminescence properties. *CrystEngComm*, 15(18): 3647-3653.

69. Jiang, B., Tian, C., Pan, Q., Jiang, Z., Wang, J.-Q., Yan, W. and Fu, H. (2011). Enhanced Photocatalytic Activity and Electron Transfer Mechanisms of Graphene/TiO2 with Exposed {001} Facets. *Journal of Physical Chemistry C*, 115(48): 23718-23725.

70. Jiang, L. and Gao, L. (2005). Fabrication and characterization of ZnO-coated multi-walled carbon nanotubes with enhanced photocatalytic activity. *Materials Chemistry and Physics*, 91(2): 313-316.

71. Jimenez-Cadena, G., Comini, E., Ferroni, M., Vomiero, A. and Sberveglieri, G. (2010). Synthesis of different ZnO nanostructures by modified PVD process and potential use for dye-sensitized solar cells. *Materials Chemistry and Physics*, 124(1): 694-698.

72. Joo, J., Kwon, S. G., Yu, J. H. and Hyeon, T. (2005). Synthesis of ZnO Nanocrystals with Cone, Hexagonal Cone, and Rod Shapes via Non-Hydrolytic Ester Elimination Sol–Gel Reactions. *Advanced Materials*, 17(15): 1873-1877.

73. Joshi, T., Ganguly, P., Haranath, D., Singh, S. and Biradar, A. M. (2014). Tuning the photoluminescence of ferroelectric liquid crystal by controlling

the size of dopant ZnO quantum dots. *Materials Letters*, 114(0): 156-158.

74. Kavitha, M. K., Haripadmam, P. C., Gopinath, P., Krishnan, B. and John, H. (2013a). Effect of morphology and solvent on two-photon absorption of nano zinc oxide. *Materials Research Bulletin*, 48(5): 1967-1971.

75. Kavitha, M. K., Jinesh, K. B., Philip, R., Gopinath, P. and John, H. (2014a). Defect engineering in ZnO nanocones for visible photoconductivity and nonlinear absorption. *Physical Chemistry Chemical Physics*, 16(45): 25093-25100

76. Kavitha, M. K., John, H. and Gopinath, P. (2014b). Polyvinyl pyrrolidone assisted low temperature synthesis of ZnO nanocones and its linear and nonlinear optical studies. *Materials Research Bulletin*, 49(0): 132-137.

77. Kavitha, M. K., John, H., Gopinath, P. and Philip, R. (2013b). Synthesis of reduced graphene oxide-ZnO hybrid with enhanced optical limiting properties. *Journal of Materials Chemistry C*, 1(23): 3669-3676.

78. Khanderi, J., Hoffmann, R. C., Gurlo, A. and Schneider, J. J. (2009). Synthesis and sensoric response of ZnO decorated carbon nanotubes. *Journal of Materials Chemistry*, 19(28): 5039-5046.

79. Kharlampieva, E., Kozlovskaya, V. and Sukhishvili, S. A. (2009). Layer-by-Layer Hydrogen-Bonded Polymer Films: From Fundamentals to Applications. *Advanced Materials*, 21(30): 3053-3065.

80. Kim, Y. J., Lee, J. H. and Yi, G. C. (2009). Vertically aligned ZnO nanostructures grown on graphene layers. *Applied Physics Letters*, 95(21): 213101.

81. Kind, H., Yan, H., Messer, B., Law, M. and Yang, P. (2002). Nanowire Ultraviolet Photodetectors and Optical Switches. *Advanced Materials*, 14(2): 158-160.

82. Knutsen, K. E., Galeckas, A., Zubiaga, A., Tuomisto, F., Farlow, G. C., Svensson, B. G. and Kuznetsov, A. Y. (2012). Zinc vacancy and oxygen interstitial in ZnO revealed by sequential annealing and electron irradiation. *Physical Review B*, 86(12): 121203.

83. Kováčik, R., Meyer, B. and Marx, D. (2007). F Centers versus Dimer Vacancies on ZnO Surfaces: Characterization by STM and STS Calculations. *Angewandte Chemie International Edition*, 46(26): 4894-4897.

84. Krishnamurthy, S. and Kamat, P. V. (2014). CdSe–Graphene Oxide Light-Harvesting Assembly: Size-Dependent Electron Transfer and Light Energy Conversion Aspects. *ChemPhysChem*, 15(10): 2129-2135.

85. Kuo, C. Y., Ko, R. M., Tu, Y. C., Lin, Y. R., Lin, T. H. and Wang, S. J. (2012). Tip Shaping for ZnO Nanorods via Hydrothermal Growth of ZnO Nanostructures in a Stirred Aqueous Solution. *Crystal Growth & Design*, 12(8): 3849-3855.

86. Kuo, S. Y., Hsieh, M. Y. and Lin, H. I. (2014). Investigation on the Tunable-Length Zinc Oxide Nanowire Arrays for Dye-Sensitized Solar Cells. *International Journal of Photoenergy*, 2014: 404753.

87. Kurbanov, S. S., Panin, G. N., Kim, T. W. and Kang, T. W. (2009). Strong violet luminescence from ZnO nanocrystals grown by the low-temperature chemical solution deposition. *Journal of Luminescence*, 129(9): 1099-1104.

88. Kushwaha, A. and Aslam, M. (2012). Defect induced high photocurrent in solution grown vertically aligned ZnO nanowire array films. *Journal of Applied Physics*, 112(5): 054316.

89. Laudise, R. A. and Ballman, A. A. (1960). Hydrothermal synthesis of Zinc oxide and Zinc sulphide. *Journal of Physical Chemistry*, 64(5): 688-691.

90. Lee, J. M., Pyun, Y. B., Yi, J., Choung, J. W. and Park, W. I. (2009). ZnO Nanorod−Graphene Hybrid Architectures for Multifunctional Conductors. *Journal of Physical Chemistry C*, 113(44): 19134-19138.

91. Lee, J. S., You, K. H. and Park, C. B. (2012). Highly Photoactive, Low Bandgap TiO2 Nanoparticles Wrapped by Graphene. *Advanced Materials*, 24(8): 1084-1088.

92. Lee, S. K., Chen, S. L., Hongxing, D., Sun, L., Chen, Z., Chen, W. M. and Buyanova, I. A. (2010). Long lifetime of free excitons in ZnO tetrapod structures. *Applied Physics Letters*, 96(8): 083104.

93. Leiter, F. H., Alves, H. R., Hofstaetter, A., Hofmann, D. M. and Meyer, B. K. (2001). The Oxygen Vacancy as the Origin of a Green Emission in Undoped ZnO. *Physica status solidi (b)*, 226(1): R4-R5.

94. Leung, Y. H., Chen, X. Y., Ng, A. M. C., Guo, M. Y., Liu, F. Z., Djurišić, A. B., Chan, W. K., Shi, X. Q. and Van Hove, M. A. (2013). Green emission in ZnO nanostructures - Examination of the roles of oxygen and zinc vacancies. *Applied Surface Science*, 271(0): 202-209.

95. Li, B. and Cao, H. (2011a). ZnO@graphene composite with enhanced performance for the removal of dye from water. *Journal of Materials Chemistry*, 21(10): 3346-3349.

96. Li, B., Liu, T., Wang, Y. and Wang, Z. (2012). ZnO/graphene-oxide

nanocomposite with remarkably enhanced visible-light-driven photocatalytic performance. *Journal of Colloid and Interface Science*, 377(1): 114-121.

97. Li, C., Liu, C., Li, Q. and Gong, Q. (2004). Broadband optical limiting and nonlinear optical absorption properties of a novel hyperbranched conjugated polymer. *Chemical Physics Letters*, 400(4–6): 569-572.

98. Li, F. M., Hsieh, G. W., Dalal, S., Newton, M. C., Stott, J. E., Hiralal, P., Nathan, A., Warburton, P. A., Unalan, H. E., Beecher, P., Flewitt, A. J., Robinson, I., Amaratunga, G. and Milne, W. I. (2008). Zinc Oxide Nanostructures and High Electron Mobility Nanocomposite Thin Film Transistors. *IEEE Transactions on Electron Devices*, 55(11): 3001-3011.

99. Li, H., Wang, J., Liu, H., Zhang, H. and Li, X. (2005). Zinc oxide films prepared by sol–gel method. *Journal of Crystal Growth*, 275(1–2): 943-946.

100. Li, M., Xing, G., Xing, G., Wu, B., Wu, T., Zhang, X. and Sum, T. C. (2013). Origin of green emission and charge trapping dynamics in ZnO nanowires. *Physical Review B*, 87(11): 115309.

101. Li, W. J., Shi, E. W., Zhong, W. Z. and Yin, Z. W. (1999). Growth mechanism and growth habit of oxide crystals. *Journal of Crystal Growth*, 203(1–2): 186-196.

102. Li, X., Zhang, G., Bai, X., Sun, X., Wang, X., Wang, E. and Dai, H. (2008). Highly conducting graphene sheets and Langmuir-Blodgett films. *Nature Nanotechnology*, 3(9): 538-542.

103. Li, Z., Wang, J., Liu, X., Liu, S., Ou, J. and Yang, S. (2011). Electrostatic layer-by-layer self-assembly multilayer films based on graphene and manganese dioxide sheets as novel electrode materials for supercapacitors. *Journal of Materials Chemistry*, 21(10): 3397-3403.

104. Lightcap, I. V., Kosel, T. H. and Kamat, P. V. (2010). Anchoring Semiconductor and Metal Nanoparticles on a Two-Dimensional Catalyst Mat. Storing and Shuttling Electrons with Reduced Graphene Oxide. *Nano Letters*, 10(2): 577-583.

105. Liu, S., Sun, H., Suvorova, A. and Wang, S. (2013). One-pot hydrothermal synthesis of ZnO-reduced graphene oxide composites using Zn powders for enhanced photocatalysis. *Chemical Engineering Journal*, 229(0): 533-539.

106. Liu, X., Du, H. and Sun, X. W. (2014). High-performance photoresponse of carbon-doped ZnO/reduced graphene oxide hybrid nanocomposites under UV and visible illumination. *RSC Advances*, 4(10): 5136-5140.

107. Liu, X., Pan, L., Lv, T., Lu, T., Zhu, G., Sun, Z. and Sun, C. (2011). Microwave-assisted synthesis of ZnO-graphene composite for photocatalytic reduction of Cr(vi). *Catalysis Science & Technology*, 1(7): 1189-1193.

108. Liu, Y., Zhang, Z., Xu, H., Zhang, L., Wang, Z., Li, W., Ding, L., Hu, Y., Gao, M., Li, Q. and Peng, L.-M. (2009). Visible Light Response of Unintentionally Doped ZnO Nanowire Field Effect Transistors. *Journal of Physical Chemistry C*, 113(38): 16796-16801.

109. Liu, Z., Wang, Y., Zhang, X., Xu, Y., Chen, Y. and Tian, J. (2009). Nonlinear optical properties of graphene oxide in nanosecond and picosecond regimes. *Applied Physics Letters*, 94(2): 021902-3.

110. Liu, Z. B., Xu, Y. F., Zhang, X. Y., Zhang, X. L., Chen, Y. S. and Tian, J. G. (2009). Porphyrin and Fullerene Covalently Functionalized Graphene Hybrid Materials with Large Nonlinear Optical Properties. *Journal of Physical Chemistry B*, 113(29): 9681-9686.

111. Look, D. C., Hemsky, J. W. and Sizelove, J. R. (1999a). Residual Native Shallow Donor in ZnO. *Physical Review Letters*, 82(12): 2552-2555.

112. Look, D. C., Reynolds, D. C., Hemsky, J. W., Jones, R. L. and Sizelove, J. R. (1999b). Production and annealing of electron irradiation damage in ZnO. *Applied Physics Letters*, 75(6): 811-813.

113. Lu, M., Lee, D., Xue, W. and Cui, T. (2009). Flexible and disposable immunosensors based on layer-by-layer self-assembled carbon nanotubes and biomolecules. *Sensors and Actuators A: Physical*, 150(2): 280-285.

114. Luo, D., Zhang, G., Liu, J. and Sun, X. (2011). Evaluation Criteria for Reduced Graphene Oxide. *Journal of Physical Chemistry C*, 115(23): 11327-11335.

115. Lv, J., Zhu, J., Huang, K., Meng, F., Song, X. and Sun, Z. (2011). Tunable surface wettability of ZnO nanorods prepared by two-step method. *Applied Surface Science*, 257(17): 7534-7538.

116. Lv, Y., Yao, W., Ma, X., Pan, C., Zong, R. and Zhu, Y. (2013). The surface oxygen vacancy induced visible activity and enhanced UV activity of a ZnO_{1-x} photocatalyst. *Catalysis Science & Technology*, 3(12): 3136-3146.

117. McClure, S. A., Worfolk, B. J., Rider, D. A., Tucker, R. T., Fordyce, J. A. M., Fleischauer, M. D., Harris, K. D., Brett, M. J. and Buriak, J. M. (2009). Electrostatic Layer-by-Layer Assembly of CdSe Nanorod/Polymer Nanocomposite Thin Films. *ACS Applied Materials & Interfaces*, 2(1):

219-229.

118. Min, S. K., Oh C. H., Lee, G. J., and Lee, Y.P. (2009). Nonlinear Optical Properties of ZnO Nanorods Prepared by Using the Electro-deposition Method. *Journal of the Korean Physical Society*, 55(3): 1005-1008.

119. Mishra, S. K., Srivastava, R. K., Prakash, S. G., Yadav, R. S. and Panday, A. C. (2010). Photoluminescence and photoconductive characteristics of hydrothermally synthesized ZnO nanoparticles. *Opto-Electronics Review*, 18(4): 467-473.

120. Moazzami, K., Murphy, T. E., Phillips, J. D., Cheung, M. C. K. and Cartwright, A. N. (2006). Sub-bandgap photoconductivity in ZnO epilayers and extraction of trap density spectra. *Semiconductor Science and Technology*, 21(6): 717.

121. Morishige, K., Kittaka, S., Moriyasu, T. and Morimoto, T. (1980). Thermal desorption study of surface hydroxyls on ZnO. *J C S Faraday 1*, 76: 738-745.

122. Morozov, S. V., Novoselov, K. S., Katsnelson, M. I., Schedin, F., Elias, D. C., Jaszczak, J. A. and Geim, A. K. (2008). Giant Intrinsic Carrier Mobilities in Graphene and Its Bilayer. *Physical Review Letters*, 100(1): 016602.

123. Murphy, S., Huang, L. and Kamat, P. V. (2013). Reduced Graphene Oxide–Silver Nanoparticle Composite as an Active SERS Material. *Journal of Physical Chemistry C*, 117(9): 4740-4747.

124. Nair, R. R., Blake, P., Grigorenko, A. N., Novoselov, K. S., Booth, T. J., Stauber, T., Peres, N. M. R. and Geim, A. K. (2008). Fine Structure Constant Defines Visual Transparency of Graphene. *Science*, 320(5881): 1308.

125. Nethravathi, C. and Rajamathi, M. (2008a). Chemically modified graphene sheets produced by the solvothermal reduction of colloidal dispersions of graphite oxide. *Carbon*, 46(14): 1994-1998.

126. Nethravathi, C., Viswanath, B., Shivakumara, C., Mahadevaiah, N. and Rajamathi, M. (2008b). The production of smectite clay/graphene composites through delamination and co-stacking. *Carbon*, 46(13): 1773-1781.

127. Nguyen, T. L., Michael, M. and Mulvaney, P. (2014). Synthesis of Highly Crystalline CdSe@ZnO Nanocrystals via Monolayer-by-Monolayer Epitaxial Shell Deposition. *Chemistry of Materials*, 26(14): 4274-4279.

128. Novoselov, K. S., Geim, A. K., Morozov, S. V., Jiang, D., Zhang, Y.,

Dubonos, S. V., Grigorieva, I. V. and Firsov, A. A. (2004). Electric Field Effect in Atomically Thin Carbon Films. *Science*, 306(5696): 666-669.

129. Özgür, Ü., Gu, X., Chevtchenko, S., Spradlin, J., Cho, S. J., Morkoç, H., Pollak, F. H., Everitt, H. O., Nemeth, B. and Nause, J. E. (2006). Thermal conductivity of bulk ZnO after different thermal treatments. *Journal of Electronic Materials*, 35(4): 550-555.

130. Pan, X., Yang, M.-Q. and Xu, Y.-J. (2014). Morphology control, defect engineering and photoactivity tuning of ZnO crystals by graphene oxide - a unique 2D macromolecular surfactant. *Physical Chemistry Chemical Physics*, 16(12): 5589-5599.

131. Pan, Y. W., Ren, S. T., Qu, S. L. and Wang, Q. (2013). Physical model for the exotic ultraviolet photo-conductivity of ZnO nanowire films. *Chinese Physics B*, 22(11): 118102.

132. Parand, P., Samadpour, M., Esfandiar, A. and Iraji Zad, A. (2014). Graphene/PbS as a Novel Counter Electrode for Quantum Dot Sensitized Solar Cells. *ACS Photonics*, 1(4): 323-330.

133. Park, J. S., Cho, S. M., Kim, W.-J., Park, J. and Yoo, P. J. (2011). Fabrication of Graphene Thin Films Based on Layer-by-Layer Self-Assembly of Functionalized Graphene Nanosheets. *ACS Applied Materials & Interfaces*, 3(2): 360-368.

134. Park, Y. R., Liu, N. and Lee, C. J. (2013). Photoluminescence enhancement from hybrid structures of metallic single-walled carbon nanotube/ZnO films. *Current Applied Physics*, 13(9): 2026-2032.

135. Patel, D. B., Chauhan, K. R. and Mukhopadhyay, I. (2014). Revealing the charge transport mechanism of a photoelectrochemical cell: analysis using A.C. voltage perturbation. *Physical Chemistry Chemical Physics*, 16(38): 20900-20908.

136. Peining, Z., Nair, A. S., Shengjie, P., Shengyuan, Y. and Ramakrishna, S. (2012). Facile Fabrication of TiO2–Graphene Composite with Enhanced Photovoltaic and Photocatalytic Properties by Electrospinning. *ACS Applied Materials & Interfaces*, 4(2): 581-585.

137. Perera, S. D., Mariano, R. G., Vu, K., Nour, N., Seitz, O., Chabal, Y. and Balkus, K. J. (2012). Hydrothermal Synthesis of Graphene-TiO2 Nanotube Composites with Enhanced Photocatalytic Activity. *ACS Catalysis*, 2(6): 949-956.

138. Pham, V. H., Dang, T. T., Hur, S. H., Kim, E. J. and Chung, J. S. (2012). Highly Conductive Poly(methyl methacrylate) (PMMA)-Reduced Graphene Oxide Composite Prepared by Self-Assembly of PMMA Latex

and Graphene Oxide through Electrostatic Interaction. *ACS Applied Materials & Interfaces*, 4(5): 2630-2636.

139. Phan, T. L., Yu, S. C., Vincent, R., Dan, N. H. and Shi, W. S. (2010). Photoluminescence properties of various CVD-grown ZnO nanostructures. *Journal of Luminescence*, 130(7): 1142-1146.

140. Pirruccio, G., Martín Moreno, L., Lozano, G. and Gómez Rivas, J. (2013). Coherent and Broadband Enhanced Optical Absorption in Graphene. *ACS Nano*, 7(6): 4810-4817.

141. Polsongkram, D., Chamninok, P., Pukird, S., Chow, L., Lupan, O., Chai, G., Khallaf, H., Park, S. and Schulte, A. (2008). Effect of synthesis conditions on the growth of ZnO nanorods via hydrothermal method. *Physica B: Condensed Matter*, 403(19–20): 3713-3717.

142. Pradhan, D., Mohapatra, S. K., Tymen, S., Misra, M. and Leung, K. T. (2011). Morphology-Controlled ZnO Nanomaterials for Enhanced Photoelectrochemical Performance. *Materials Express*, 1(1): 59-67.

143. Qin, L., Shing, C., Sawyer, S. and Dutta, P. S. (2011). Enhanced ultraviolet sensitivity of zinc oxide nanoparticle photoconductors by surface passivation. *Optical Materials*, 33(3): 359-362.

144. Rai, P., Kwak, W. K. and Yu, Y. T. (2013). Solvothermal Synthesis of ZnO Nanostructures and Their Morphology-Dependent Gas-Sensing Properties. *ACS Applied Materials & Interfaces*, 5(8): 3026-3032.

145. Remyamol, T., Gopinath, P. and John, H. (2014a). Phenylenediamine functionalized reduced graphene oxide/polyaniline hybrid: synthesis, characterization, improved conductivity and photocurrent generation. *RSC Advances*, 4(56): 29901-29908.

146. Remyamol, T., John, H. and Gopinath, P. (2013). Grafting of self assembled polyaniline nanorods on reduced graphene oxide for nonlinear optical application. *Synthetic Metals*, 185–186(0): 38-44.

147. Remyamol, T., Pramod, G. and Honey, J. (2014b). Photoinduced electron transfer, improved nonlinear optical properties and photocurrent generation in polyaniline-graphite oxide hybrid. *Materials Research Express*, 1(3): 035051.

148. Reyes, P. I., Ku, C. J., Duan, Z., Xu, Y., Garfunkel, E. and Lu, Y. (2012). Reduction of persistent photoconductivity in ZnO thin film transistor-based UV photodetector. *Applied Physics Letters*, 101(3): 031118.

149. Rodríguez-Paéz, J. E., Caballero, A. C., Villegas, M., Moure, C., Durán, P. and Fernández, J. F. (2001). Controlled precipitation methods: formation

mechanism of ZnO nanoparticles. *Journal of the European Ceramic Society*, 21(7): 925-930.

150. Schmidt-Mende, L. and MacManus-Driscoll, J. L. (2007). ZnO – nanostructures, defects, and devices. *Materials Today*, 10(5): 40-48.

151. Shao, D., Sun, H., Yu, M., Lian, J. and Sawyer, S. (2012). Enhanced Ultraviolet Emission from Poly(vinyl alcohol) ZnO Nanoparticles Using a SiO_2–Au Core/Shell Structure. *Nano Letters*, 12(11): 5840-5844.

152. Shao, D., Yu, M., Sun, H., Hu, T., lian, J. and Sawyer, S. (2013). High responsivity, fast ultraviolet photodetector fabricated from ZnO nanoparticle-graphene core-shell structures. *Nanoscale*, 5(9): 3664-3667.

153. Sharma, P., Sreenivas, K. and Rao, K. V. (2003). Analysis of ultraviolet photoconductivity in ZnO films prepared by unbalanced magnetron sputtering. *Journal of Applied Physics*, 93(7): 3963-3970.

154. Sheetz, R. M., Ponomareva, I., Richter, E., Andriotis, A. N. and Menon, M. (2009). Defect-induced optical absorption in the visible range in ZnO nanowires. *Physical Review B*, 80(19): 195314.

155. Sheik-Bahae, M., Said, A. A., Wei, T. H., Hagan, D. J. and Van Stryland, E. W. (1990). Sensitive measurement of optical nonlinearities using a single beam.*, IEEE Journal of Quantum Electronics*, 26(4): 760-769.

156. Shen, J., Hu, Y., Li, C., Qin, C., Shi, M. and Ye, M. (2009). Layer-by-Layer Self-Assembly of Graphene Nanoplatelets. *Langmuir*, 25(11): 6122-6128.

157. Shen, J., Hu, Y., Qin, C. and Ye, M. (2008). Layer-by-Layer Self-Assembly of Multiwalled Carbon Nanotube Polyelectrolytes Prepared by in Situ Radical Polymerization. *Langmuir*, 24(8): 3993-3997.

158. Shim, E., Lee, C., Jung, E., Lee, J., Kim, D., Lee, Y., Kim, D. and Lee, S. (2012). Enhanced native acceptor-related blue emission of ZnO thin films annealed in an oxygen ambient. *Journal of the Korean Physical Society*, 60(11): 1939-1943.

159. Shimazaki, Y., Nakamura, R., Ito, S. and Yamamoto, M. (2000). Molecular Weight Dependence of Alternate Adsorption through Charge-Transfer Interaction. *Langmuir*, 17(3): 953-956.

160. Singh, G., Choudhary, A., Haranath, D., Joshi, A. G., Singh, N., Singh, S. and Pasricha, R. (2012). ZnO decorated luminescent graphene as a potential gas sensor at room temperature. *Carbon*, 50(2): 385-394.

161. Singh, J., Kumar, P, Hui, K. S., Hui, K. N., Ramam, K., Tiwari, R. S. and

Srivastava, O. N. (2012). Synthesis, band-gap tuning, structural and optical investigations of Mg doped ZnO nanowires. *CrystEngComm*, 14(18): 5898-5904.

162. Soci, C., Zhang, A., Xiang, B., Dayeh, S. A., Aplin, D. P. R., Park, J., Bao, X. Y., Lo, Y. H. and Wang, D. (2007). ZnO Nanowire UV Photodetectors with High Internal Gain. *Nano Letters*, 7(4): 1003-1009.

163. Son, D. I., Kwon, B. W., Park, D. H., Seo, W.-S., Yi, Y., Angadi, B., Lee, C. L. and Choi, W. K. (2012). Emissive ZnO–graphene quantum dots for white-light-emitting diodes. *Nature Nanotechnology*, 7: 465–471.

164. Song, S., Xue, Y., Feng, L., Elbatal, H., Wang, P., Moorefield, C. N., Newkome, G. R. and Dai, L. (2014). Reversible Self-Assembly of Terpyridine-Functionalized Graphene Oxide for Energy Conversion. *Angewandte Chemie International Edition*, 53(5): 1415-1419.

165. Song, T., Choung, J. W., Park, J.-G., Park, W. I., Rogers, J. A. and Paik, U. (2008). Surface Polarity and Shape-Controlled Synthesis of ZnO Nanostructures on GaN Thin Films Based on Catalyst-Free Metalorganic Vapor Phase Epitaxy. *Advanced Materials*, 20(23): 4464-4469.

166. Song, W., Kwon, S. Y., Myung, S., Jung, M. W., Kim, S. J., Min, B. K., Kang, M.-A., Kim, S. H., Lim, J. and An, K.-S. (2014). High-mobility ambipolar ZnO-graphene hybrid thin film transistors. *Sci. Rep.*, 4:

167. Soon Ki Min, C. H. O., Geon Joon Lee, Young Pak Lee, Sun Ki Min and Sung Hwan Han (2009). Nonlinear Optical Properties of ZnO Nanorods Prepared by Using the Electro-deposition Method. *Journal of the Korean Physical Society*, 55(3): 1005-1008.

168. Srikant, V. and Clarke, D. R. (1998). On the optical band gap of zinc oxide. *Journal of Applied Physics*, 83(10): 5447-5451.

169. Stankovich, S., Dikin, D. A., Piner, R. D., Kohlhaas, K. A., Kleinhammes, A., Jia, Y., Wu, Y., Nguyen, S. T. and Ruoff, R. S. (2007). Synthesis of graphene-based nanosheets via chemical reduction of exfoliated graphite oxide. *Carbon*, 45(7): 1558-1565.

170. Stankovich, S., Piner, R. D., Chen, X., Wu, N., Nguyen, S. T. and Ruoff, R. S. (2006). Stable aqueous dispersions of graphitic nanoplatelets via the reduction of exfoliated graphite oxide in the presence of poly(sodium 4-styrenesulfonate). *Journal of Materials Chemistry*, 16(2): 155-158.

171. Stehr, J. E., Chen, S. L., Reddy, N. K., Tu, C. W., Chen, W. M. and Buyanova, I. A. (2014). Turning ZnO into an Efficient Energy Upconversion Material by Defect Engineering. *Advanced Functional Materials*: 3760–3764.

172. Stryland, E. W. V., Wu, Y. Y., Hagan, D. J., Soileau, M. J. and Mansour, K. (1988). Optical limiting with semiconductors. *Journal of the Optical Society of America B: Optical Physics*, 5(9): 1980-1988.

173. Suchand Sandeep, C. S., Samal, A. K., Pradeep, T. and Philip, R. (2010). Optical limiting properties of Te and Ag_2Te nanowires. *Chemical Physics Letters*, 485(4–6): 326-330.

174. Sun, X., Liu, Z., Welsher, K., Robinson, J., Goodwin, A., Zaric, S. and Dai, H. (2008). Nano-graphene oxide for cellular imaging and drug delivery. *Nano Research*, 1(3): 203-212.

175. Sun, X., Yu, R. Q., Xu, G. Q., Hor, T. S. A. and Ji, W. (1998). Broadband optical limiting with multiwalled carbon nanotubes. *Applied Physics Letters*, 73(25): 3632-3634.

176. Sun, X. M., Chen, X., Deng, Z. X. and Li, Y. D. (2003). A CTAB-assisted hydrothermal orientation growth of ZnO nanorods. *Materials Chemistry and Physics*, 78(1): 99-104.

177. Sunandan, B. and Joydeep, D. (2009). Hydrothermal growth of ZnO nanostructures. *Science and Technology of Advanced Materials*, 10(1): 013001.

178. Sutherland, R. L. (2003). *Handbook of Nonlinear Optics* (2^{nd} ed.). Macel Dekker: Newyork.

179. Tak, Y., Hong, S. J., Lee, J. S. and Yong, K. (2009). Fabrication of ZnO/CdS core/shell nanowire arrays for efficient solar energy conversion. *Journal of Materials Chemistry*, 19(33): 5945-5951.

180. Tauc, J. (1966). *The Optical Properties of Solids*. Academic Press: Newyork.

181. Tian, J., Liu, S., Li, H., Wang, L., Zhang, Y., Luo, Y., Asiri, A. M., Al-Youbi, A. O. and Sun, X. (2012). One-step preparation of ZnO nanoparticle-decorated reduced graphene oxide composites and their application to photocurrent generation. *RSC Advances*, 2(4): 1318-1321.

182. van de Walle, C. G. and Neugebauer, J. (2004). First-principles calculations for defects and impurities: Applications to III-nitrides. *Journal of Applied Physics*, 95(8): 3851-3879.

183. van Dijken, A., Makkinje, J. and Meijerink, A. (2001). The influence of particle size on the luminescence quantum efficiency of nanocrystalline ZnO particles. *Journal of Luminescence*, 92(4): 323-328.

184. van Dijken, A., Meulenkamp, E. A., Vanmaekelbergh, D. and Meijerink, A. (2000a). The Kinetics of the Radiative and Nonradiative Processes in Nanocrystalline ZnO Particles upon Photoexcitation. *Journal of Physical Chemistry B*, 104(8): 1715-1723.

185. van Dijken, A., Meulenkamp, E. A., Vanmaekelbergh, D. and Meijerink, A. (2000b). The luminescence of nanocrystalline ZnO particles: the mechanism of the ultraviolet and visible emission. *Journal of Luminescence*, 87–89(0): 454-456.

186. Vanheusden, K., Seager, C. H., Warren, W. L., Tallant, D. R. and Voigt, J. A. (1996a). Correlation between photoluminescence and oxygen vacancies in ZnO phosphors. *Applied Physics Letters*, 68(3): 403-405.

187. Vanheusden, K., Warren, W. L., Seager, C. H., Tallant, D. R., Voigt, J. A. and Gnade, B. E. (1996b). Mechanisms behind green photoluminescence in ZnO phosphor powders. *Journal of Applied Physics*, 79(10): 7983-7990.

188. Venturini, J., Koudoumas, E., Couris, S., Janot, J. M., Seta, P., Mathis, C. and Leach, S. (2002). Optical limiting and nonlinear optical absorption properties of C60-polystyrene star polymer films: C60 concentration dependence. *Journal of Materials Chemistry*, 12(7): 2071-2076.

189. Venugopal Rao, S., Naga Srinivas, N. K. M. and Narayana Rao, D. (2002). Nonlinear absorption and excited state dynamics in Rhodamine B studied using Z-scan and degenerate four wave mixing techniques. *Chemical Physics Letters*, 361(5–6): 439-445.

190. Vivas, M. G., Shih, T., Voss, T., Mazur, E. and Mendonca, C. R. (2010). Nonlinear spectra of ZnO: reverse saturable, two- and three-photon absorption. *Optics Express*, 18(9): 9628-9633.

191. Wang, A., Long, L., Zhao, W., Song, Y., Humphrey, M. G., Cifuentes, M. P., Wu, X., Fu, Y., Zhang, D., Li, X. and Zhang, C. (2012). Increased optical nonlinearities of graphene nanohybrids covalently functionalized by axially-coordinated porphyrins. *Carbon*, 53(0): 327-338.

192. Wang, B. G., Shi, E. W. and Zhong, W. Z. (1997). Understanding and Controlling the Morphology of ZnO Crystallites under Hydrothermal Conditions. *Crystal Research and Technology*, 32(5): 659-667.

193. Wang, C. Y. and Adhikari, S. (2011). ZnO-CNT composite nanotubes as nanoresonators. *Physics Letters A*, 375(22): 2171-2175.

194. Wang, D. and Song, C. (2005). Controllable Synthesis of ZnO Nanorod and Prism Arrays in a Large Area. *Journal of Physical Chemistry B*, 109(26): 12697-12700.

195. Wang, H., Robinson, J. T., Li, X. and Dai, H. (2009). Solvothermal Reduction of Chemically Exfoliated Graphene Sheets. *Journal of the American Chemical Society*, 131(29): 9910-9911.

196. Wang, J., Chen, Y., Li, R., Dong, H., Zhang, L., Lotya, M., Jonathan, N. C. and Werner, J. B. (2011) Nonlinear Optical Properties of Graphene and Carbon Nanotube Composites. In Yellampalli, S., (Eds.) *Carbon Nanotubes - Synthesis, Characterization, Applications*. InTech.

197. Wang, J., Hernandez, Y., Lotya, M., Coleman, J. N. and Blau, W. J. (2009). Broadband Nonlinear Optical Response of Graphene Dispersions. *Advanced Materials*, 21(23): 2430-2435.

198. Wang, J., Wang, Z., Huang, B., Ma, Y., Liu, Y., Qin, X., Zhang, X. and Dai, Y. (2012). Oxygen Vacancy Induced Band-Gap Narrowing and Enhanced Visible Light Photocatalytic Activity of ZnO. *ACS Applied Materials & Interfaces*, 4(8): 4024-4030.

199. Wang, R., Wang, Y., Xu, C., Sun, J. and Gao, L. (2013). Facile one-step hydrazine-assisted solvothermal synthesis of nitrogen-doped reduced graphene oxide: reduction effect and mechanisms. *RSC Advances*, 3(4): 1194-1200.

200. Wang, X., Yin, L., Liu, G., Wang, L., Saito, R., Lu, G. Q. and Cheng, H.-M. (2011). Polar interface-induced improvement in high photocatalytic hydrogen evolution over ZnO-CdS heterostructures. *Energy & Environmental Science*, 4(10): 3976-3979.

201. Wang, Z. L. (2009). ZnO nanowire and nanobelt platform for nanotechnology. *Materials Science and Engineering Reports*, 64(3–4): 33-71.

202. Willander, M., Nur, O., Sadaf, J. R., Qadir, M. I., Zaman, S., Zainelabdin, A., Bano, N. and Hussain, I. (2010). Luminescence from Zinc Oxide Nanostructures and Polymers and their Hybrid Devices. *Materials*, 3(4): 2643-2667.

203. Williams, G. and Kamat, P. V. (2009). Graphene−Semiconductor Nanocomposites: Excited-State Interactions between ZnO Nanoparticles and Graphene Oxide. *Langmuir*, 25(24): 13869-13873.

204. Xu, C., Wu, X., Zhu, J. and Wang, X. (2008). Synthesis of amphiphilic graphite oxide. *Carbon*, 46(2): 386-389.

205. Xu, L., Guo, Y., Liao, Q., Zhang, J. and Xu, D. (2005). Morphological Control of ZnO Nanostructures by Electrodeposition. *Journal of Physical Chemistry B*, 109(28): 13519-13522.

206. Xu, S., Cheng, C., Guo, W., He, Y., Huang, R., Du, S. and Wang, N. (2013). Tuning the optical and electrical properties of hydrothermally grown ZnO nanowires by sealed post annealing treatment. *Solid State Communications*, 160(0): 41-46.

207. Xu, T., Zhang, L., Cheng, H. and Zhu, Y. (2011). Significantly enhanced photocatalytic performance of ZnO via graphene hybridization and the mechanism study. *Applied Catalysis B: Environmental*, 101(3–4): 382-387.

208. Xu, X., Wu, M., Asoro, M., Ferreira, P. J. and Fan, D. L. (2012). One-Step Hydrothermal Synthesis of Comb-Like ZnO Nanostructures. *Crystal Growth & Design*, 12(10): 4829-4833.

209. Xu, Y., Liu, Z., Zhang, X., Wang, Y., Tian, J., Huang, Y., Ma, Y., Zhang, X. and Chen, Y. (2009). A Graphene Hybrid Material Covalently Functionalized with Porphyrin: Synthesis and Optical Limiting Property. *Advanced Materials*, 21(12): 1275-1279.

210. Yang, R., Ding, Y. and Wang, Z. L. (2004). Deformation-Free Single-Crystal Nanohelixes of Polar Nanowires. *Nano Letters*, 4(7): 1309-1312.

211. Yang, W., Chen, G., Shi, Z., Liu, C. C., Zhang, L., Xie, G., Cheng, M., Wang, D., Yang, R., Shi, D., Watanabe, K., Taniguchi, T., Yao, Y., Zhang, Y. and Zhang, G. (2013). Epitaxial growth of single-domain graphene on hexagonal boron nitride. *Nature Materials*, 12(9): 792-797.

212. Yang, Y., Xie, Y., Pang, L., Li, M., Song, X., Wen, J. and Zhao, H. (2013). Preparation of Reduced Graphene Oxide/Poly(acrylamide) Nanocomposite and Its Adsorption of Pb(II) and Methylene Blue. *Langmuir*, 29(34): 10727-10736.

213. Yazyev, O. V. and Louie, S. G. (2010). Electronic transport in polycrystalline graphene. *Nature Materials*, 9(10): 806-809.

214. Yoo, D. H., Cuong, T. V., Lee, S., Hwang, W. S., Yoo, W. J., Hong, C.-H. and Hahn, S. H. (2014). Unraveling Oxygen Transfer at the Graphene Oxide–ZnO Nanorod Interface. *Journal of Physical Chemistry C*, 118(31): 17638-17642.

215. Yoonessi, M. and Gaier, J. R. (2010). Highly Conductive Multifunctional Graphene Polycarbonate Nanocomposites. *ACS Nano*, 4(12): 7211-7220.

216. Zan, L., Genlian, F., Zhanqiu, T., Qiang, G., Dingbang, X., Yishi, S., Zhiqiang, L. and Di, Z. (2014). Uniform dispersion of graphene oxide in aluminum powder by direct electrostatic adsorption for fabrication of

graphene/aluminum composites. *Nanotechnology*, 25(32): 325601.

217. Zeng, H., Duan, G., Li, Y., Yang, S., Xu, X. and Cai, W. (2010). Blue Luminescence of ZnO Nanoparticles Based on Non-Equilibrium Processes: Defect Origins and Emission Controls. *Advanced Functional Materials*, 20(4): 561-572.

218. Zeng, J. H., Jin, B. B. and Wang, Y. F. (2009). Facet enhanced photocatalytic effect with uniform single-crystalline zinc oxide nanodisks. *Chemical Physics Letters*, 472(1–3): 90-95.

219. Zhan, X., Wang, Q., Wang, F., Wang, Y., Wang, Z., Cao, J., Safdar, M. and He, J. (2014). Composition-Tuned ZnO/ZnxCd1–xTe Core/Shell Nanowires Array with Broad Spectral Absorption from UV to NIR for Hydrogen Generation. *ACS Applied Materials & Interfaces*, 6(4): 2878-2883.

220. Zhan, Z., Zheng, L., Pan, Y., Sun, G. and Li, L. (2012). Self-powered, visible-light photodetector based on thermally reduced graphene oxide-ZnO (rGO-ZnO) hybrid nanostructure. *Journal of Materials Chemistry*, 22(6): 2589-2595.

221. Zhang, B. Y., Liu, T., Meng, B., Li, X., Liang, G., Hu, X. and Wang, Q. J. (2013). Broadband high photoresponse from pure monolayer graphene photodetector. *Nat Commun*, 4: 1811.

222. Zhang, C., Zhang, J., Su, Y., Xu, M., Yang, Z. and Zhang, Y. (2014). ZnO nanowire/reduced graphene oxide nanocomposites for significantly enhanced photocatalytic degradation of Rhodamine 6G. *Physica E: Low-dimensional Systems and Nanostructures*, 56(0): 251-255.

223. Zhang, G., Shen, X. and Yang, Y. (2011). Facile Synthesis of Monodisperse Porous ZnO Spheres by a Soluble Starch-Assisted Method and Their Photocatalytic Activity. *Journal of Physical Chemistry C*, 115(15): 7145-7152.

224. Zhang, H., Lv, X., Li, Y., Wang, Y. and Li, J. (2009). P25-Graphene Composite as a High Performance Photocatalyst. *ACS Nano*, 4(1): 380-386.

225. Zhang, J., Liu, H., Wang, Z. and Ming, N. (2008). Low-temperature growth of ZnO with controllable shapes and band gaps. *Journal of Crystal Growth*, 310(11): 2848-2853.

226. Zhang, J., Liu, H., Wang, Z., Ming, N., Li, Z. and Biris, A. S. (2007). Polyvinylpyrrolidone-Directed Crystallization of ZnO with Tunable Morphology and Bandgap. *Advanced Functional Materials*, 17(18): 3897-3905.

227. Zhang, L. Z. and Xiang, L. (2011). Influence of sodium dodecyl sulfate on the fabrication of zinc oxide nanoparticles. *Research on Chemical Intermediates*, 37(2-5): 281-289.

228. Zhang, Q., Dandeneau, C. S., Zhou, X. and Cao, G. (2009). ZnO Nanostructures for Dye-Sensitized Solar Cells. *Advanced Materials*, 21(41): 4087-4108.

229. Zhang, X., Qin, J., Xue, Y., Yu, P., Zhang, B., Wang, L. and Liu, R. (2014). Effect of aspect ratio and surface defects on the photocatalytic activity of ZnO nanorods. *Sci. Rep.*, 4:

230. Zhang, Y., Tan, Y. W., Stormer, H. L. and Kim, P. (2005). Experimental observation of the quantum Hall effect and Berry's phase in graphene. *Nature*, 438(7065): 201-204.

231. Zhang, Z. and Mu, J. (2007). Hydrothermal synthesis of ZnO nanobundles controlled by PEO–PPO–PEO block copolymers. *Journal of Colloid and Interface Science*, 307(1): 79-82.

232. Zhou, X., Shi, T. and Zhou, H. (2012). Hydrothermal preparation of ZnO-reduced graphene oxide hybrid with high performance in photocatalytic degradation. *Applied Surface Science*, 258(17): 6204-6211.

233. Zhou, X., Xie, Z.-X., Jiang, Z.-Y., Kuang, Q., Zhang, S.-H., Xu, T., Huang, R.-B. and Zheng, L.-S. (2005). Formation of ZnO hexagonal micro-pyramids: a successful control of the exposed polar surfaces with the assistance of an ionic liquid. *Chemical Communications*, (44): 5572-5574.

234. Zhou, Y., Bao, Q., Tang, L. A. L., Zhong, Y. and Loh, K. P. (2009). Hydrothermal Dehydration for the "Green" Reduction of Exfoliated Graphene Oxide to Graphene and Demonstration of Tunable Optical Limiting Properties. *Chemistry of Materials*, 21(13): 2950-2956.

235. Zhu, Y., Elim, H. I., Foo, Y. L., Yu, T., Liu, Y., Ji, W., Lee, J. Y., Shen, Z., Wee, A. T. S., Thong, J. T. L. and Sow, C. H. (2006). Multiwalled Carbon Nanotubes Beaded with ZnO Nanoparticles for Ultrafast Nonlinear Optical Switching. *Advanced Materials*, 18(5): 587-592.

236. Zhu, Y., Stoller, M. D., Cai, W., Velamakanni, A., Piner, R. D., Chen, D. and Ruoff, R. S. (2010). Exfoliation of Graphite Oxide in Propylene Carbonate and Thermal Reduction of the Resulting Graphene Oxide Platelets. *ACS Nano*, 4(2): 1227-1233.

237. Zuniga Perez, J., Munoz-Sanjose, V., Palacios-Lidon, E. and Colchero, J. (2005). Polarity Effects on ZnO Films Grown along the Nonpolar [1120] direction. *Physical Review Letters*, 95(22): 226105.

LIST OF PUBLICATIONS BASED OF THESIS

PUBLISHED

1. Kavitha, M. K., Jinesh, K. B., Philip, R., Gopinath, P. and John, H. (2014). Defect engineering in ZnO nanocones for visible photoconductivity and nonlinear absorption. *Physical Chemistry Chemical Physics*, 16(45): 25093-25100

2. Kavitha, M. K., John, H. and Gopinath, P. (2014). Polyvinyl pyrrolidone assisted low temperature synthesis of ZnO nanocones and its linear and nonlinear optical studies. *Materials Research Bulletin*, 49(0): 132-137.

3. Kavitha, M. K., Haripadmam, P. C., Gopinath, P., Krishnan, B. and John, H. (2013). Effect of morphology and solvent on two-photon absorption of nano zinc oxide. *Materials Research Bulletin*, 48(5): 1967-1971.

4. Kavitha, M. K., John, H., Gopinath, P. and Philip, R. (2013). Synthesis of reduced graphene oxide-ZnO hybrid with enhanced optical limiting properties. *Journal of Materials Chemistry C*, 1(23): 3669-3676.

5. Haripadmam, P. C., Kavitha, M. K., John H., Krishnan, B., and Gopinath, P. (2012). Optical limiting studies of ZnO nanotops and its polymer nanocomposite films*, Applied Physics Letters*, 101(7): 071103.

COMMUNICATED

1. Kavitha, M. K., Pillai, S. C., Gopinath, P and John, H. UV and solar photocatalysis of ZnO decorated reduced graphene oxide, *Journal of Environmental Chemical Engineering*, under review

2. Kavitha, M. K., Gopinath, P and John, H. Tailoring the visible light photoconductivity of reduced graphene oxide/ZnO layer-by-layer films by the intrinsic defect states in ZnO, *Physical Chemistry and Chemical Physics,* under review

UNDER PREPARATION

1. Kavitha, M. K., Gopinath, P. and John, H. Nonlinear absorption in graphene/ZnO layer-by-layer self assembled films

PRESENTATIONS IN CONFERENCES/SEMINARS

Oral Presentations

1. Kavitha, M. K., Gopinath, P and John, H. Visible light photoconductivity in ZnO and ZnO-graphene hybrids. *National Conference on Material Science and Technology, NCMST 2014, IIST, Thiruvanthapuram*. 28-30 Jul. (2014)

2. Kavitha, M. K., Gopinath, P and John, H. Polyvinylpyrrolidone Assisted Low Temperature Synthesis of ZnO Nanocones and Its Optical Limiting Property. *25th Kerala Science Congress 2013, Technopark, Thiruvanthapuram.* 29 Jan.- 1 Feb. (2013)

3. Kavitha, M. K., Gopinath, P and John, H. Synthesis of nano ZnO with different morphologies. *National Seminar on Frontiers of Chemistry 2011, IIST, Thiruvanthapuram.*07-08 Dec. (2011)

4. Kavitha, M. K., Gopinath, P and John, H. Weak quantum confinement in Triangular ZnO nanostructures. *IIST Research scholars Day 2011, IIST, Thiruvanthapuram.* 16-17 Dec. (2011)

Poster Presentations

1. Kavitha, M. K., Gopinath, P and John, H. Improved photocatalytic activity of ZnO-graphene hybrid. *International Union of Materials Research Societies – International Conference in Asia, IUMRS-ICA-2013, IISc Bangalore*. 16-20 Dec. (2013)

2. Kavitha, M. K., Gopinath, P and John, H. Hydrothermal Synthesis of reduced Graphene oxide–ZnO hybrid with its enhanced optical limiting property. *NanoIndia 2013, CSIR-NIIST, Thiruvanthapuram*. 19-20 Feb. (2013)

3. Kavitha, M. K., Gopinath, P and John, H. Synthesis, characterization and photoluminescence of Triangular ZnO nanostructures. *NanoSciTech 2012 - International Conference on Frontiers of Nanoscience, Nanotechnology & Their Applications, Punjab University, Chandigarh.* 15-18 Feb. (2012) **Best poster award.**

4. Kavitha, M. K., John, H. and Krishnan, B. Fiber optic chemical sensor using polyaniline modified cladding. *Optical Society of India-International conference on Contemporary trends in Optics and Optoelectronics 2011, IIST, Thiruvanthapuram.* 17-19 Jan. (2011)